1-1-2011

Studies in Magnetism and Superconductivity under Extreme Pressure

Wenli Bi
Washington University in St. Louis

Recommended Citation

Bi, Wenli, "Studies in Magnetism and Superconductivity under Extreme Pressure" (2011). *All Theses and Dissertations (ETDs)*. 554.
https://openscholarship.wustl.edu/etd/554

WASHINGTON UNIVERSITY IN ST. LOUIS

Department of Physics

Dissertation Examination Committee:
James S. Schilling, Chairperson
Daniel Haskel
Sophia E. Hayes
Kenneth F. Kelton
Alexander Seidel
Philip Skemer

STUDIES IN MAGNETISM AND SUPERCONDUCTIVITY UNDER EXTREME PRESSURE

by

Wenli Bi

A dissertation presented to the
Graduate School of Arts and Sciences
of Washington University in
partial fulfillment of the
requirements for the degree
of Doctor of Philosophy

December 2011

St. Louis, Missouri

Preface

Studies of superconductivity, magnetism and structure under pressure have made important contributions to further our understanding of the physical properties of materials in material science, geoscience, and astrophysics. High pressure can create new superconductors, transform the magnetic state, and generate structural phase transitions in materials. In Eu metal the strong local moment magnetism in divalent Eu ($4f^7$) suppresses superconductivity, but under sufficiently high pressure, Eu is expected to become trivalent and nonmagnetic ($4f^6$). Recently, superconductivity in Eu was discovered by Debessai *et al.* for pressures above 80 GPa, where the transition temperature was found to be only ~2 K, nearly an order of magnitude lower than for comparable trivalent *s,p,d*-electron metals (Sc, Y, La, and Lu). This might be because its crystal structure is less favorable for superconductivity, or that Eu is not fully trivalent but rather mixed-valent. In this thesis I present the results of extensive high pressure studies on Eu's structure, valence, and magnetism to nearly 1 Mbar pressure through a series of synchrotron techniques including x-ray diffraction, x-ray absorption near edge structure (XANES), x-ray magnetic circular dichroism (XMCD), and synchrotron Mössbauer spectroscopy (SMS). Results of high pressure studies on the

magnetism and superconductivity through ac susceptibility and electrical resistivity on selected Eu compounds and novel Fe-based superconductors will also be described.

Acknowledgments

I would like to thank all the people who have helped and inspired me during my Ph.D. study. Especially I express my most sincere thanks to:

My advisor Prof. James Schilling, for his guidance and support during my research at Washington University. I have gained such invaluable experience from working with him.

Dr. Daniel Haskel, Dr. Narcizo Souza-Neto, Dr. Ercan Alp, Dr. Yue Meng, and Dr. Jiyong Zhao from APS, Argonne National Lab, for the great collaborations and their generous support during my experiments at their beamlines.

Dr. James Hamlin for introducing me to the ac susceptibility technique and the DAC system. Dr. Mathiewos Debessai for training me in the He-gas and DAC system. Dr. Takahiro Matsuoka for teaching me the electrical resistivity technique in the DAC. Prof. Schilling's other past and present group members Narelle Hillier, Hunter Banks, Gilberto Fabbris, Neda Foroozani, and Jinhyuk Lim for technical supports and discussions.

Dr. Ravhi Kumar, Prof. Andrew Cornelius, and Dr. Y. Zhang, for their great help in analyzing Eu's x-ray diffraction data and their hospitality during my stay at UNLV.

Dr. A. Gangopadhyay for his assistance with the PPMS measurements.

Prof. Joshua Maurer and Dawn Johnson from the Washington University chemistry department for their generous help in developing the photolithography technique for the DAC.

My parents Jiezhao Bi and Meiju Liu who raised me with a love of science and supported me in all my pursuits. Most of all, my husband Jahangir Alam, for his love, continual support, and encouragement.

Contents

List of Tables

List of Figures

Chapter 1

Introduction

Following the discovery of superconductivity in mercury in 1911 [1], the first high pressure studies on superconductors were carried out by Sizoo and Onnes on Sn and In in 1925 [2]. Applying pressure changes the inter-atomic distance and modifies the electronic structure of a material without introducing additional chemical complexity. With technological developments allowing static pressures as high as 350 GPa to be generated using diamond anvil cells, high pressure techniques have been extensively used in recent years to explore the physical states of condensed matter systems, to create new ground states, to test theoretical models, and to help develop new theories. For example, following the discovery of the superconductivity of 30 K in a ceramic material containing La, Ba, Cu, and O (LBCO) by Bednorz and Müller [3], the first so-called high T_c cuprate superconductors, Chu *et al.* [4] applied pressure on this superconductor and found that T_c drastically increased with increasing pressure, which motivated the authors to reduce the lattice parameters by replacing La with a smaller isoelectronic ion Y, leading to the discovery of the famous YBCO compound with T_c of 90 K, the first superconductor with T_c above the boiling temperature of liquid nitrogen. The current highest recorded T_c of $\sim$160 K was achieved by applying pressure of $\sim$30

GPa in $HgBa_2Ca_2Cu_3O_{8+\delta}$, which has an ambient T_c of 134 K [5].

Pressure can also change the physical properties of elemental solids. In the periodic table, only 30 elemental metals superconduct at ambient pressure, but under sufficiently high pressure, 23 more become superconductors. The most recent addition to the elemental superconductors is the pressure-induced superconductivity in Eu metal above 80 GPa discovered by Debessai *et al.* [7]. At ambient pressure, Eu is divalent and has strong local magnetic moment ($4f^7,\ J = \frac{7}{2}$), which suppresses superconductivity. Under pressure Eu is expeceted to lose one $4f$ electron, become trivalent and nonmagnetic ($4f^6,\ J = 0$), and possibly superconducting. However, the T_c of Eu was found to be only $\sim$2 K, almost an order of magnitude lower than for comparable trivalent *s,p,d*-electron metals (Sc, Y, La and Lu). To help understand the superconducting mechanism, a major portion of this thesis research is focused on high pressure studies in Eu, with respect to its crystal structure, valence, and magnetic states under pressures to 1 Mbar using several x-ray techniques including x-ray diffraction, XANES, XMCD, and SMS. The high pressure experiments were performed in diamond anvil cells at the Advanced Photon Source, Argonne National Lab.

Recently, the discovery of the new Fe-pnictide superconductors has attracted a lot of interest from theorists and experimentalists. Three years after the discovery of F-doped LaFeAsO compound with T_c of 26 K by Hosono's group [8], a vast number of research papers had been published on this topic. The weak antiferromagnetic interactions between Fe ions may play an important role in the superconductivity of the Fe-pnictides. It is believed the electron-phonon interaction alone in cuprates and the Fe-pnictides is not sufficient to overcome the Coulomb repulsion between electrons in order to form Cooper pairs. High pressure experiments provide a unique probe to further our understanding of the new type of superconductors. However, experiments with different pressure media show that Fe-pnictide superconductors are sensitive to lattice strains introduced by nonhydrostatic pressure media [6]. To understand the intrinsic dependence of the superconducting state on pressure, high pressure experiments under the most hydrostatic conditions with He as a pressure medium are desired.

The thesis is organized as follows: Chapter 2 gives general background information about the effect of high pressure on superconductivity, magnetism, and structure followed by a brief review of Eu and Fe-pnictides under pressure. Chapter 3 describes the high pressure synchrotron, ac susceptibility, and electrical resistivity techniques used in this thesis research. Chapter 4 details and discusses the experimental results, and Chapter 5 summarizes the results. Appendices A and B contain the results of ac susceptibility measurements on Na, K, and Nb.

Chapter 2

Background: Theory and Experiment

Pressure, like temperature, is a basic thermodynamic variable and has been applied in many areas of research. Under pressure, atoms and molecules get closer together, the volume decreases, and materials become denser. When the atomic volume decreases, the degree of atomic orbital overlap increases. This causes a wide range of changes in the electronic structure, leading to changes in the crystal structure, and in the electrical, magnetic, and superconducting states. This chapter presents a brief introduction to the effect of high pressure on superconductivity, magnetism, and structure in elemental solids with an emphasis on lanthanides, and provide some background information on Eu, and on superconductivity and magnetism in the Fe-pnictides.

2.1 High Pressure Effect

2.1.1 High Pressure Effect on Superconductivity

Superconductivity was discovered in 1911 by Heike Kamerlingh Onnes in mercury at 4.15 K [1]. Superconductors exhibit two primary phenomena when they are cooled below the critial temperature: (1) zero dc-electrical resistivity when the current in the superconductor is below a critical value, and (2) exclusion of magnetic flux from the interior of the superconductor (Meissener effect) when the applied field is below the critical value. In the 100 years since its discovery, many researchers have strived to understand this exotic phenomenon experimentally and theoretically. However, superconductivity was not clearly understood until Bardeen, Cooper, and Schrieffer formulated a complete microscopic theory in 1957 [10].

In BCS theory the electrons form pairs mediated by phonons. In the limit of weak electron-phonon coupling, the BCS theory gives the superconducting critical temperature as

$$T_c = 1.14 \left(\frac{\hbar\omega_D}{k_B}\right) \exp\left[\frac{-1}{N(E_F)V_{eff}}\right] \tag{2.1}$$

where ω_D is the Debye frequency, k_B is the Boltzmann constant, $N(E_F)$ is the density of states at the Fermi level, and $V_{eff} > 0$ is the net attractive potential between electrons. To illustrate the effect of pressure on superconductivity, Equation 2.1 can be rewritten in simplified form as

$$T_c \approx \sqrt{\frac{k}{m}} e^{-k/\eta} \tag{2.2}$$

where m is the cation mass, k is the lattice spring constant, and η is the Hopfield parameter, a purely electronic term. In this equation the Coulomb repulsion between electrons in the Cooper pairs has been ignored. The isotope effect, $T_c \propto \sqrt{\frac{1}{m}}$ can be seen in Equation 2.2.

Under pressure the spring constant k increases due to the lattice stiffening and η also normally increases. Since high pressure changes the lattice parameters and electronic structure, it changes the critical superconducting temperature. The pressure effect on the superconducting temperature dT_c/dP depends on the pressure-induced changes in

k and η. As k increases with pressure, the increase of the prefactor $\sqrt{k}$ is overwhelmed by the decrease from $-k$ in the exponent, leading to rapid decrease of T_c in simple metals like Al, In, and Pb. For transition metals, T_c may either increase or decrease under pressure due to the different changes in the electronic term η. An extensive review of pressure effect on elemental, binary and high T_c cuprate superconducting materials can be found in Reference [11].

Although T_c decreases under pressure in many elemental superconductors, applying pressure does induce superconductivity in some of the elements. As seen in Figure 2.1, upon the application of pressure, the number of elemental superconductors increases to 53 from the ambient pressure 30 superconductors [17]. Among the alkali metals, only Li superconducts at ambient pressure, but T_c is extremely low. Under pressure Cs also becomes superconducting due to pressure-induced *s*-*d* electron transfer [12]. Pressure-induced superconductivity is also observed in magnetic metals such as Fe and Ce when the magnetic state is destroyed by pressure. Insulating or semiconducting solids do not superconduct at ambient pressure. However, under pressure some materials such as Si, Ge, P, and S transform to a metallic phase and become superconducting. In lanthanides, only La superconducts at ambient pressure [14]. Under pressure, Ce [15], Lu [16], and Eu [7] become superconducting. The most recently discovered elemental superconductor, Eu, will be discussed in more details in Section 2.2 and in Chapter 4.

2.1.2 Effect of Pressure on Magnetism

Magnetism is another important property of a material. In the isolated neutral atomic state, 76 elements have a well-defined magnetic moment. When condensed in a solid

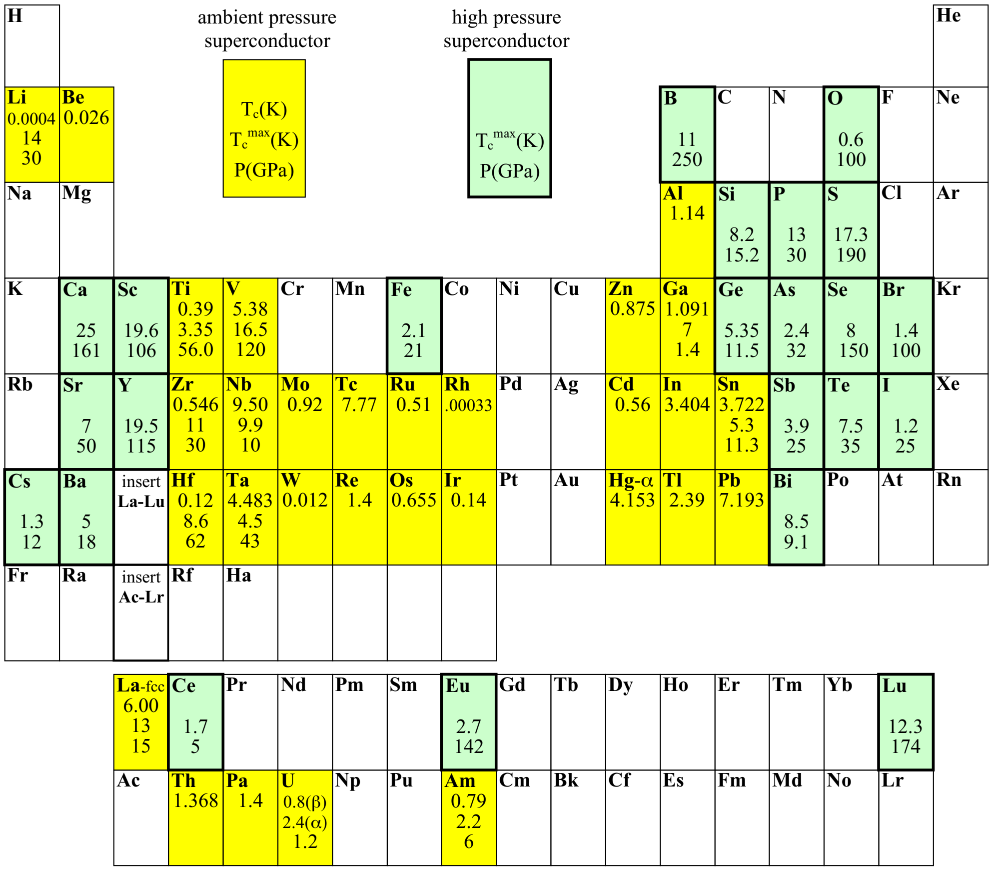

H				ambient pressure superconductor T_c(K) T_c^{max}(K) P(GPa)					high pressure superconductor T_c^{max}(K) P(GPa)								**He**
Li 0.0004 14 30	**Be** 0.026											**B** 11 250	**C**	**N**	**O** 0.6 100	**F**	**Ne**
Na	**Mg**											**Al** 1.14	**Si** 8.2 15.2	**P** 13 30	**S** 17.3 190	**Cl**	**Ar**
K	**Ca** 25 161	**Sc** 19.6 106	**Ti** 0.39 3.35 56.0	**V** 5.38 16.5 120	**Cr**	**Mn**	**Fe** 2.1 21	**Co**	**Ni**	**Cu**	**Zn** 0.875	**Ga** 1.091 7 1.4	**Ge** 5.35 11.5	**As** 2.4 32	**Se** 8 150	**Br** 1.4 100	**Kr**
Rb	**Sr** 7 50	**Y** 19.5 115	**Zr** 0.546 11 30	**Nb** 9.50 9.9 10	**Mo** 0.92	**Tc** 7.77	**Ru** 0.51	**Rh** .00033	**Pd**	**Ag**	**Cd** 0.56	**In** 3.404	**Sn** 3.722 5.3 11.3	**Sb** 3.9 25	**Te** 7.5 35	**I** 1.2 25	**Xe**
Cs 1.3 12	**Ba** 5 18	insert **La-Lu**	**Hf** 0.12 8.6 62	**Ta** 4.483 4.5 43	**W** 0.012	**Re** 1.4	**Os** 0.655	**Ir** 0.14	**Pt**	**Au**	**Hg-α** 4.153	**Tl** 2.39	**Pb** 7.193	**Bi** 8.5 9.1	**Po**	**At**	**Rn**
Fr	**Ra**	insert **Ac-Lr**	**Rf**	**Ha**													
		La-fcc 6.00 13 15	**Ce** 1.7 5	**Pr**	**Nd**	**Pm**	**Sm**	**Eu** 2.7 142	**Gd**	**Tb**	**Dy**	**Ho**	**Er**	**Tm**	**Yb**	**Lu** 12.3 174	
		Ac	**Th** 1.368	**Pa** 1.4	**U** 0.8(β) 2.4(α) 1.2	**Np**	**Pu**	**Am** 0.79 2.2 6	**Cm**	**Bk**	**Cf**	**Es**	**Fm**	**Md**	**No**	**Lr**	

Figure 2.1: Periodic table of superconductivity. At ambient pressure 30 elements superconduct (in yellow) and under pressure 23 more (in green with bold box) become superconducting. The highest observed critical temperature is given by T_c^{max} and the pressure at which T_c^{max} is achieved is given by P [17]. If T_c decreases under pressure, only the ambient pressure T_c is given.

state, however, only 24 of them retain in the magnetic state. The destruction of magnetism is due to the orbital interactions between the nearest-neighbor atoms. If the magnetic orbitals of the nearest-neighbor atoms overlap sufficiently, binding will be preferred instead of magnetism. The degree of the orbital overlap can be quantified as $\alpha \equiv R_{ws}/R_{mo}$, where $R_{ws} = (3V_a/4\pi)^{\frac{1}{3}}$ is the Wigner-Seitz radius , $V_a = V/N_A$ is the volume per atom, V is the molar volume, N_A is Avogadro's number, and R_{mo} is radius at the maximum charge density of the magnetic orbital taken from Reference [19]. For example, Eu has the atomic configuration $[Xe]\,4f^7 6s^2$ and the magnetism arises from the partially filled $4f$ shell. R_{mo} is given by the maximum of the charge density of the $4f - \frac{7}{2}$ orbital.

Figure 2.2 shows the ratio α for all the elemental solids with $Z \leq 98$. Those in circles display magnetic ordering in the elemental solid. Remarkably, a critical value of $\alpha_c = 3.2$ separates the magnetic and nonmagnetic elements. Above this critical value, the elemental solids are magnetic, and below this value the elemental solids are nonmagnetic, with the exception of Cr and O.

Large alpha values reflect negligible orbital overlap and well localized magnetic state. Rare earth metals (from La to Lu) have the highest values of alpha due to the very localized character of $4f$ orbitals. From Figure 2.2 it can be inferred that even pressures near 1 Mbar would not be sufficient to force the value of alpha below the critical value 3.2. This, however, does not imply that the rare earths are magnetically inert under pressure. Under pressure, one electron after another should be squeezed out of the local $4f$-shell until finally the $4f$-orbital overlap between neighboring ions

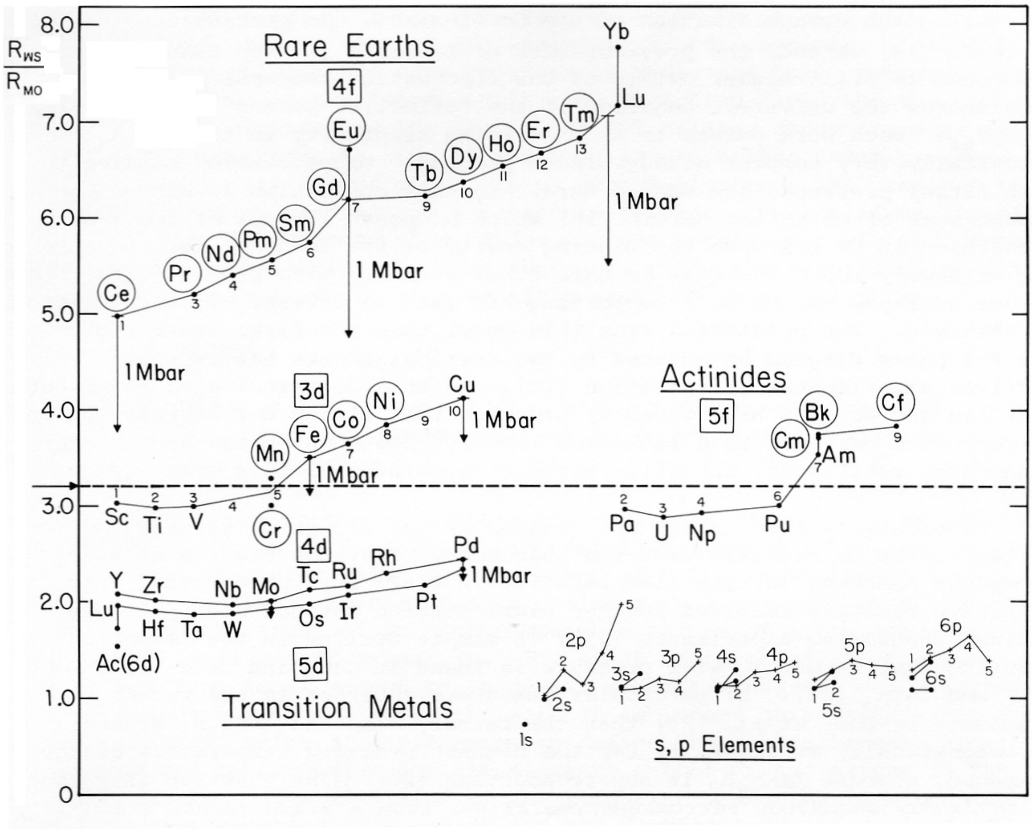

Figure 2.2: The value of $\alpha = \frac{R_{ws}}{R_{mo}}$ for all the elements in periodic table with $Z \leq 98$. The circled elements are magnetic in the condensed state. The straight dashed line shows $\alpha_c \simeq 3.2$ and separates magnetic and nonmagnetic elements. Figure adapted from Reference [18].

is sufficiently large so that a $4f$ band is formed. At high enough pressure, the band is broadened and the magnetism may be destroyed. It would, therefore, be expected that under pressure the rare earths would show the richest magnetic behavior of all elements. For example, when Eu loses one $4f$ electron ($4f^7 \rightarrow 4f^6$) it becomes nonmagnetic ($J = \frac{7}{2} \rightarrow J = 0$), whereas when Yb loses one $4f$ electron (($4f^{14} \rightarrow 4f^{13}$) it transforms from a nonmagnetic to a magnetic state.

If we know the equation of state (volume versus pressure), it is possible to estimate the pressure required to destroy the magnetism (Figure 2.2). For example, Fe has an α value close to 3.2, so a moderate pressure is expected to destroy the magnetism. In fact, Fe was found to become nonmagnetic after a pressure-induced phase transition from bcc to hcp around 14 GPa [9].

2.1.3 High Pressure Effect on Structure

At ambient pressure, most of the elemental metals including alkali (group 1), alkali-earth (group 2), transition, lanthanide and heavy actinide metals are in closed-packed structures: body-centered cubic (bcc), face-centered cubic (fcc) and hexagonal closed-packed (hcp) (Figure 2.3(a)) [20, 21]. Under pressure, however, they undergo a wide variety of structural transitions. As shown in Figure 2.3, the alkali and alkali-earth metals show anomalous behavior and transform to open structures. For example, Li becomes a semiconductor above 80 GPa [22], and Na becomes transparent around 200 GPa [23] accompanying phase transitions to complex open structures. Most transition metals either show no structural transition or have a transition to another closed-packed structure.

Many of the nonmetallic elements from group 13 to 17 are much more compressible than the transition metals due to the large initial atomic volumes. Under pressure they show a transition from open structures to closed-packed structures (see the shaded area in Figure 2.3(b)), resulting in an insulator-metal or semiconductor-metal transition. For example, oxygen transforms to a metallic state and becomes a superconductor at a pressure of 100 GPa (Figure 2.1).

Lanthanide metals have closed-packed structures at ambient pressure and transform to complex open structures under pressure. The molar volume of the lanthanides, with the exception of Eu and Yb, decreases smoothly with increasing atomic number, due to the lanthanide contraction effect [24]. With the exception of Eu and Yb, lanthanides show a general structure sequence (hcp→Sm-type→double hcp→fcc→distorted fcc) either with increasing pressure or with decreasing atomic number [26,27,39]. More discussion focused on Eu under pressures will be presented in Section 2.2. For a complete review of high pressure effects on elemental crystal structure, please refer to a series of excellent review papers [25,28–31].

Many forms of isothermal equation of state (EOS) have been used to describe the pressure-volume relation, such as Vinet universal EOS [33], Murnaghan EOS [34], logarithmic EOS [35], and Birch-Murnaghan EOS [36]. In this thesis research the third order Birch-Murnaghan equation is used, which is given by

$$P(V) = \frac{3}{2}B_0\left[\left(\frac{V_0}{V}\right)^{\frac{7}{3}} - \left(\frac{V_0}{V}\right)^{\frac{5}{3}}\right]\left\{1 + \frac{3}{4}\left(B_0' - 4\right)\left[\left(\frac{V_0}{V}\right)^{\frac{2}{3}} - 1\right]\right\}, \tag{2.3}$$

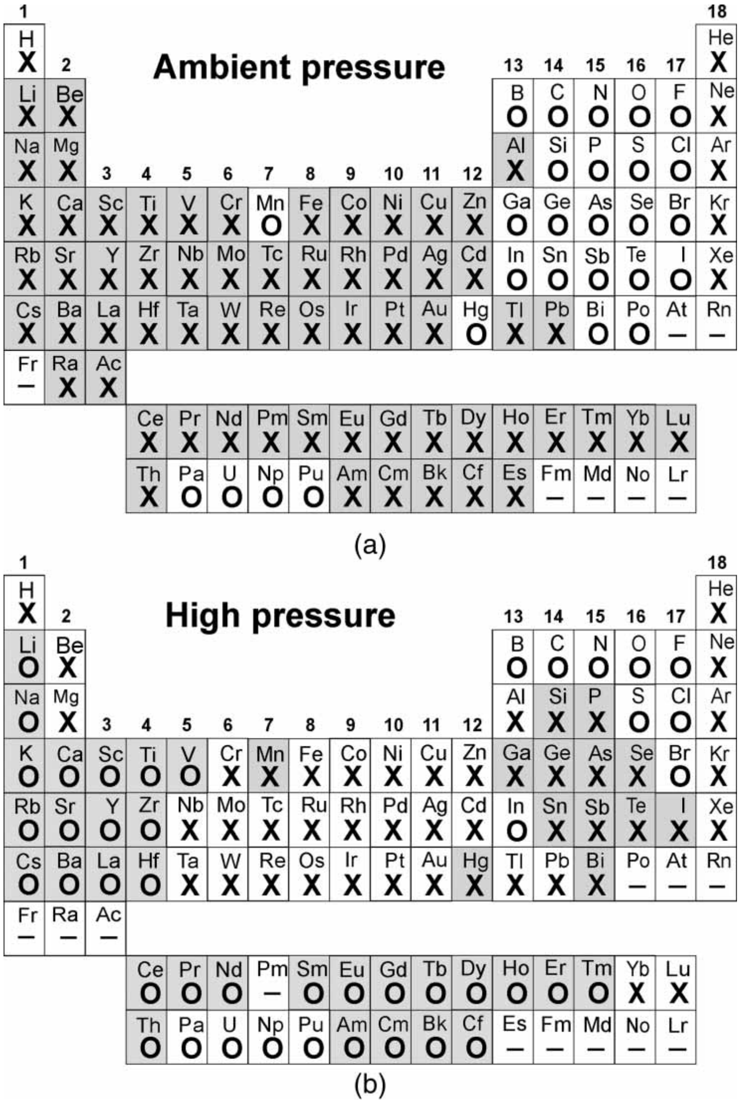

Ambient pressure

1	2	3	4	5	6	7	8	9	10	11	12	13	14	15	16	17	18
H X																	He X
Li X	Be X											B O	C O	N O	O O	F O	Ne X
Na X	Mg X											Al X	Si O	P O	S O	Cl O	Ar X
K X	Ca X	Sc X	Ti X	V X	Cr X	Mn O	Fe X	Co X	Ni X	Cu X	Zn X	Ga O	Ge O	As O	Se O	Br O	Kr X
Rb X	Sr X	Y X	Zr X	Nb X	Mo X	Tc X	Ru X	Rh X	Pd X	Ag X	Cd X	In O	Sn O	Sb O	Te O	I O	Xe X
Cs X	Ba X	La X	Hf X	Ta X	W X	Re X	Os X	Ir X	Pt X	Au X	Hg O	Tl X	Pb X	Bi O	Po O	At –	Rn –
Fr –	Ra X	Ac X															
			Ce X	Pr X	Nd X	Pm X	Sm X	Eu X	Gd X	Tb X	Dy X	Ho X	Er X	Tm X	Yb X	Lu X	
			Th X	Pa O	U O	Np O	Pu O	Am X	Cm X	Bk X	Cf X	Es X	Fm –	Md –	No –	Lr –	

(a)

High pressure

1	2	3	4	5	6	7	8	9	10	11	12	13	14	15	16	17	18
H X																	He X
Li O	Be X											B O	C O	N O	O O	F O	Ne X
Na O	Mg X											Al X	Si X	P X	S O	Cl O	Ar X
K O	Ca O	Sc O	Ti O	V O	Cr X	Mn X	Fe X	Co X	Ni X	Cu X	Zn X	Ga X	Ge X	As X	Se X	Br O	Kr X
Rb O	Sr O	Y O	Zr O	Nb X	Mo X	Tc X	Ru X	Rh X	Pd X	Ag X	Cd X	In O	Sn X	Sb X	Te X	I X	Xe X
Cs O	Ba O	La O	Hf O	Ta X	W X	Re X	Os X	Ir X	Pt X	Au X	Hg X	Tl X	Pb X	Bi X	Po –	At –	Rn –
Fr –	Ra –	Ac –															
			Ce O	Pr O	Nd O	Pm –	Sm O	Eu O	Gd O	Tb O	Dy O	Ho O	Er O	Tm O	Yb X	Lu X	
			Th O	Pa O	U O	Np O	Pu O	Am O	Cm O	Bk O	Cf O	Es –	Fm –	Md –	No –	Lr –	

(b)

Figure 2.3: Periodic table of crystal structures of elements (a) at ambient pressure and (b) under pressure [21, 32]. Crosses show the close-packed structures (bcc, fcc, and hcp). Zeros indicate the open or distorted structures. In (a) the close-packed (crosses) structures are shaded with grey. In (b), the changes from crosses to zeros and from zeros to crosses are highlighted in grey.

where V_0 is the volume at ambient pressure, B_0 is the bulk modulus and $B_0^{'}$ is its pressure derivative. The bulk modulus measures the resistance to compression. The higher the bulk modulus, the less compressible the material is. The EOS of a material can be obtained from the x-ray diffraction experiment. For materials with simple structure and known EOS under pressure (no phase transition preferred), they can be used as pressure markers in x-ray diffraction experiments. For a comprehensive review of the equations of state under pressure for elemental solids see, for example, Reference [37].

2.2 Eu under Pressure

The molar volumes of the lanthanides at ambient pressure and their pressure-induced structural transitions are summarized in Figure 2.4. Among the lanthanide series, Eu and Yb are divalent ($4f^{n+1}(5d^0 6s)^2$) while all the other lanthanides are trivalent ($4f^n(5d6s)^3$). The divalent nature of Eu ($4f^7$) and Yb ($4f^{14}$) leads to anomalous behaviors:

- Eu and Yb do not follow the lanthanide contraction at ambient pressure. As seen in Figure 2.4, the molar volumes of Eu and Yb are 45% and 38% larger, respectively, than those of their neighbors [38].
- Due to their large initial volumes, the compressibilities of Eu and Yb are larger than those of neighboring lanthanides.
- At ambient pressure and with increasing pressure, Eu and Yb do not follow the

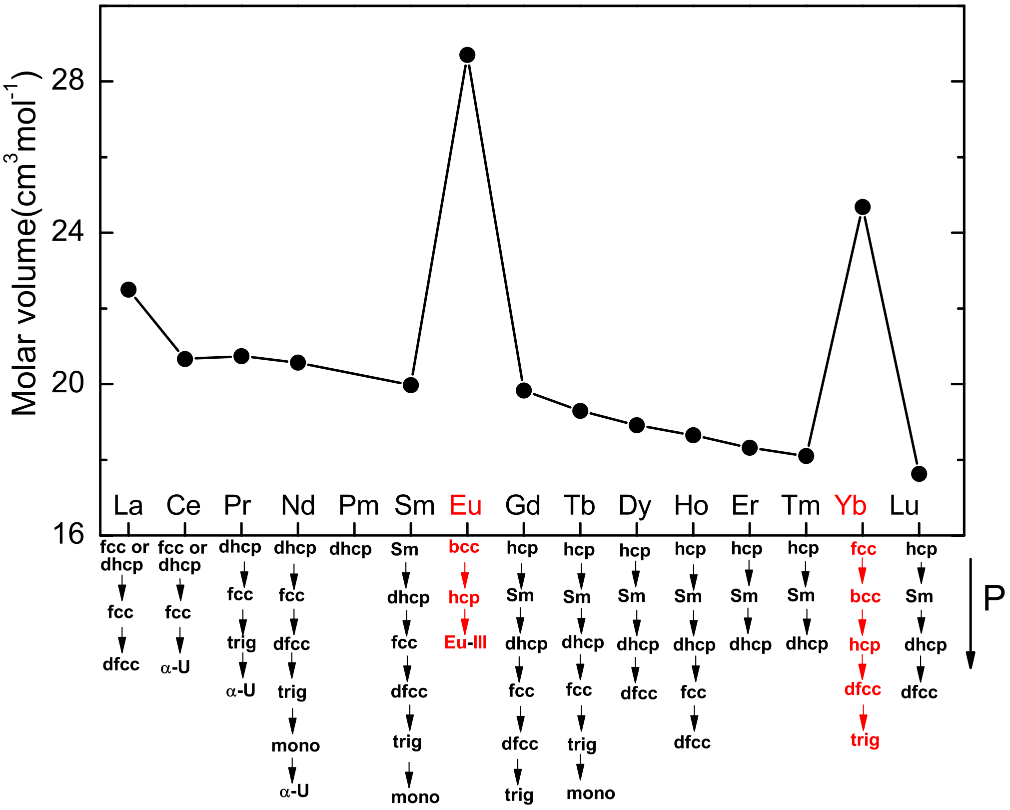

Figure 2.4: Molar volumes of lanthanide series at room temperature and ambient pressure and structural transitions with increasing pressure. Elements Eu and Yb are in red to emphasize that they show anomalous behaviors.

general structure sequence of the trivalent lanthanides.

At ambient pressure Eu has the bcc structure. Eu's structure under pressure was previously studied up to 10 GPa by McWhan *et al.* [43] and up to 27 GPa by Takemura and Syassen [38]. It was reported that Eu undergoes a bcc to hcp structural transition around 12 GPa with a volume discontinuity $\sim 4\%$ [38]. The bulk modulus in the bcc phase is 12.4 GPa from Reference [43] and 11.7 GPa from Reference [38]. Eu's bulk modulus is considerably lower than those of the trivalent lanthanides, for example, 34

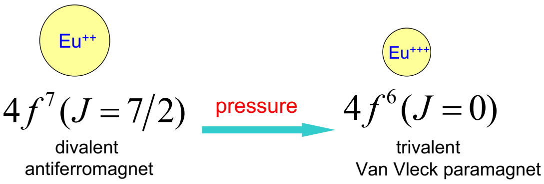

Figure 2.5: When high enough pressure is applied, Eu loses one $4f$ electron, becomes trivalent and enters the nonmagnetic ground state [39–41].

GPa for Gd [44]. In the hcp phase the c/a ratio of Eu is 1.60 and decreases with increasing pressure, approaching 1.56 at 18 GPa [38]. At pressures above 18 GPa, Eu was reported to enter an unresolved hcp-like phase up to 27 GPa [38].

At ambient pressure, divalent Eu is strongly magnetic with $4f^7$ $(J=\frac{7}{2})$ and orders antiferromagnetically below 90 K [43]. Under sufficient pressure, divalent Eu was predicted to lose one $4f$ electron to the conduction band, transform to the trivalent state, and take on the nonmagnetic ground state $(4f^7,\ J=\frac{7}{2}\rightarrow 4f^6,\ J=0)$ (see Figure 2.5). This would leave only Van Vleck paramagnetism, a very weak form of magnetism which, as we know from Am $(5f^6,\ J=0)$, is able to coexist with superconductivity [45]. The predicted pressures for a full divalent to trivalent transition vary from 34 GPa by Johansson and Rosengren [39, 40] to 70 GPa by Min *et al.* [41].

An experiment searching for superconductivity by Bundy and Dunn [46] through resistivity measurements shows no superconductivity above 2.3 K under pressures as high as 42 GPa. The measurements show that the antiferromagnetic ordering persists in 75-90 K range up to 42 GPa. Above 15 GPa, a second kink, the nature of which is undetermined, appears in the resistance at ∼150 K. At room temperature, the resistance increases under pressure and the resistance dependence of pressure shows anomalies near 12 GPa, 18 GPa, and 28 GPa, possibly related to structural transitions.

Previous studies on the valence state of Eu under pressure through XANES experiment at the L_{III} edge at room temperature to 34 GPa by Röhler [48] report that Eu's valence increases drastically with increasing pressure and saturates at 2.64 above 24 GPa. A Mössbauer experiment by Farrell and Taylor [127] performed at 44 K to 14 GPa reports that the valence reaches 2.4 at 12 GPa, and Eu still orders antiferromagnetically below 44 K but the hyperfine field decreases with increasing pressure. A more recent room temperature Mössbauer experiment by Wortmann *et al.* [49] reports that the valence increases to 2.55 at 17 GPa.

Recently, Eu was discovered to superconduct above 80 GPa by Debessai *et al.* [7] through resistivity and ac susceptibility measurements up to 142 GPa. However, T_c is only 1.7 K at 84 GPa and increases linearly under pressure with a slope of $\frac{dT_c}{dP} = +18$ mK/GPa, which is almost an order of magnitude lower than for comparable trivalent *s,p,d*-electron metals (Sc, Y, La, and Lu) (Figure 2.6). Three possible reasons for these low values were proposed by Debessai *et al.*:

1. The low T_c values indicate Eu may not be in the fully trivalent state when it becomes superconducting. It may be in a mixed-valent state.

2. The crystal structure of Eu may be less conducive for superconductivity. Am superconducts at 0.79 K at ambient pressure, while under pressure its T_c shows a complex dependence on pressure, reaching a maximum T_c of only 2.2 K at 6 GPa. It has been shown that this complex dependence is driven by structural transitions [50].

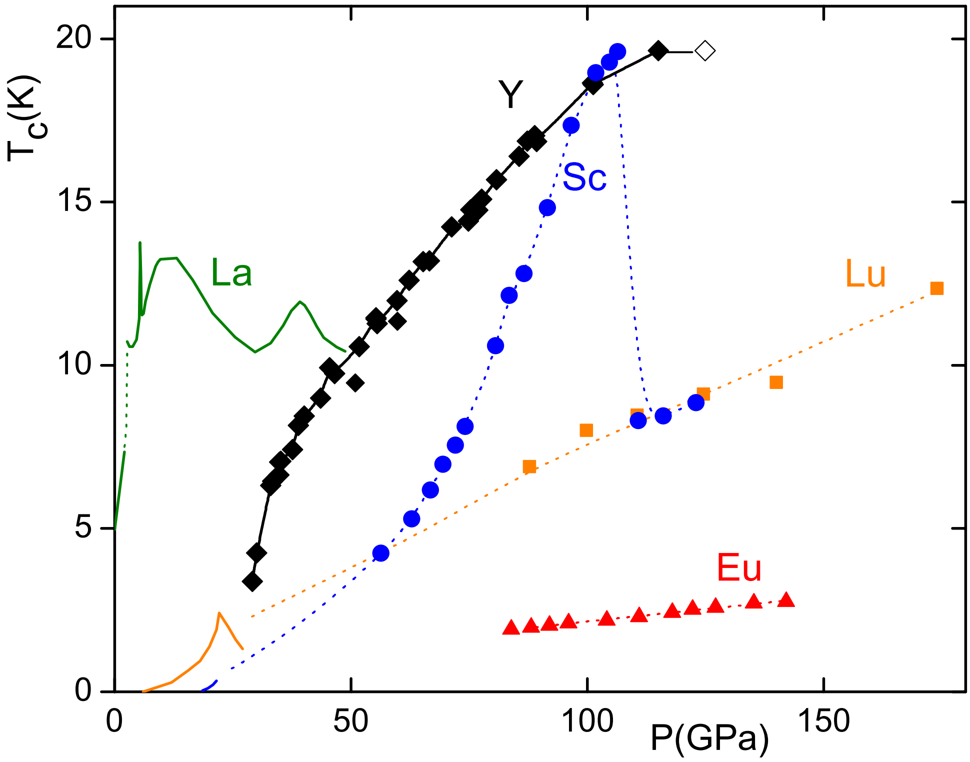

Figure 2.6: Superconducting critical temperature of Eu under pressure in comparison with trivalent *d*-electron metals Sc, Y, La, and Lu. Data for Eu are from Reference [7] and data for the trivalent metals are from Reference [47].

3. Eu is fully trivalent, but the Van Vleck paramagnetism weakens the superconductivity.

To investigate these possible reasons for the low T_c and $\frac{dT_c}{dP}$ values, experiments are needed to study Eu's valence state, crystal structure, and magnetic state in the superconducting pressure range above 80 GPa.

2.3 Fe-pnictides

The discovery of superconductivity in electron-doped LaFeAsO with T_c as high as 26 K by Kamihara *et al.* [51] started a new era of the high-temperature superconductivity. Motivated by the increase in T_c from 26 K at ambient pressure to 43 K at 4 GPa in the optimally doped sample (F doping level = 0.11) [52], substitutional replacement of the rare earth ion, denoted as R, for those with a smaller atomic volume has been carried out. The undoped RFeAsO compounds are referred to the 1111 family. The substitution has led to a rapid increase in superconducting transition temperature: 41 K for R = Ce [53] , 52 K for R = Pr [54], 52 K for R = Nd [55], 55 K for R = Sm [56], 36-50 K for R = Gd [58], 46 K for R = Tb [59], and 45 K for R = Dy [59]. Soon after the discovery of superconductivity in the electron-doped LaFeAsO, many other types of Fe-pnictide superconductors were discovered and were grouped into several families: 122 (AFe_2As_2, A = Sr, Ca, Ba, and Eu), 111 (AFeAs, A = Li and Na), and 11 (FeSe). Under optimal doping, the maximum T_c in these families is 56 K for 1111, 38 K for 122, 25 K for 111, and 15 K for 11 materials.

The structures of 1111, 122, 111, and 11 materials are shown in Figure 2.7. At room

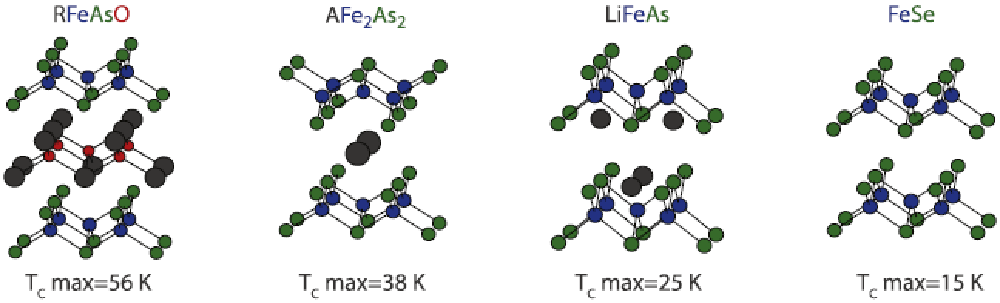

Figure 2.7: Crystal structure of 1111, 122, 111, and 11 Fe-pnictides from left to right. In all cases, the FeAs or FeSe plane is the same with different spacers between layers. Below each structure is the maximum T_c measured at ambient pressure in each family. [61]

temperature, the 122, 111 and 11 family materials have a similar layered tetragonal structure (see Figure 2.7). A common feature is the presence of the FeAs (or FeSe) layer. An interesting trend is noticed that from 1111 to 122 to 111 to 11 material the higher the optimal transition temperature, the larger the separation between the FeAs (or FeSe) layers. In fact, a theoretical study by Kurok *et al.* [62] proposed that the anion height from the Fe layer is a possible controlling parameter for the superconductivity in Fe pnictides. Motivated by this proposal, Mizuguchi *et al.* [63] systematically studied the anion height dependence of the superconducting transition temperature for typical Fe-based superconductors and found that the plot showed a symmetric curve with a peak around 1.38 Å (see Figure 2.8). The data at both ambient pressure and high pressure obey this curve, the only exception being the Pt-doped $BaFe_2As_2$ and Co-doped LaFeAsO, because the Fe-site substitution is unfavorable for superconductivity. The anion height increases in order of FeP, FeAs, FeSe and FeTe. The FeP-based superconductors have low anion heights and show lower T_c compared to the FeAs-based superconductors. For the 1111 materials, T_c increases drastically to 55 K as the rare earth at the R-site changes from La to Sm or Nd, when the anion height increases and approaches 1.38 Å. After passing the summit, T_c decreases along the curve.

It has been shown that undoped 1111 materials exhibit spin-density wave (SDW) order involving the Fe sublattice below 150 K [64] after undergoing a structural phase transition from tetragonal $P4/nmm$ to orthorhombic $Cmma$ at a temperature slightly higher than the SDW ordering temperature [65]. The magnetic transition temperature is suppressed by pressure as well as by doping while the superconducting temperature is enhanced, showing a close correlation between the magnetism and superconductivity.

Similarly, 122 materials exhibit a magnetic and a structural transition at the same temperature from a tetragonal $I4/mmm$ room temperature to an orthorhombic $Fmmm$ phase at low temperature [65–71]. In the case of $EuFe_2As_2$, its SDW from the Fe lattice orders below 185 K. Under pressure, the SDW ordering temperature shifts rapidly to lower temperatures, disappearing completely above ~2.5 GPa [72]. The pressure-temperature phase diagram is shown in Figure 2.9. In a very narrow pressure region around 3 GPa, bulk superconductivity near 30 K was reported [77]. The interactions between the strong local magnetic moments on each Eu site (Eu is divalent with a $4f^7$ orbital configuration) lead to type A antiferromagnetic order below 19 K, although the positive Curie-Weiss temperature points to predominantly ferromagnetic interactions [73]. Under pressure the antiferromagnetic ordering temperature remains constant to 2.6 GPa [74], increasing slowly at higher pressures before reaching a maximum near 55 K at ~8 GPa [72]. Above 8 GPa, $EuFe_2As_2$ orders ferromagnetically possibly due

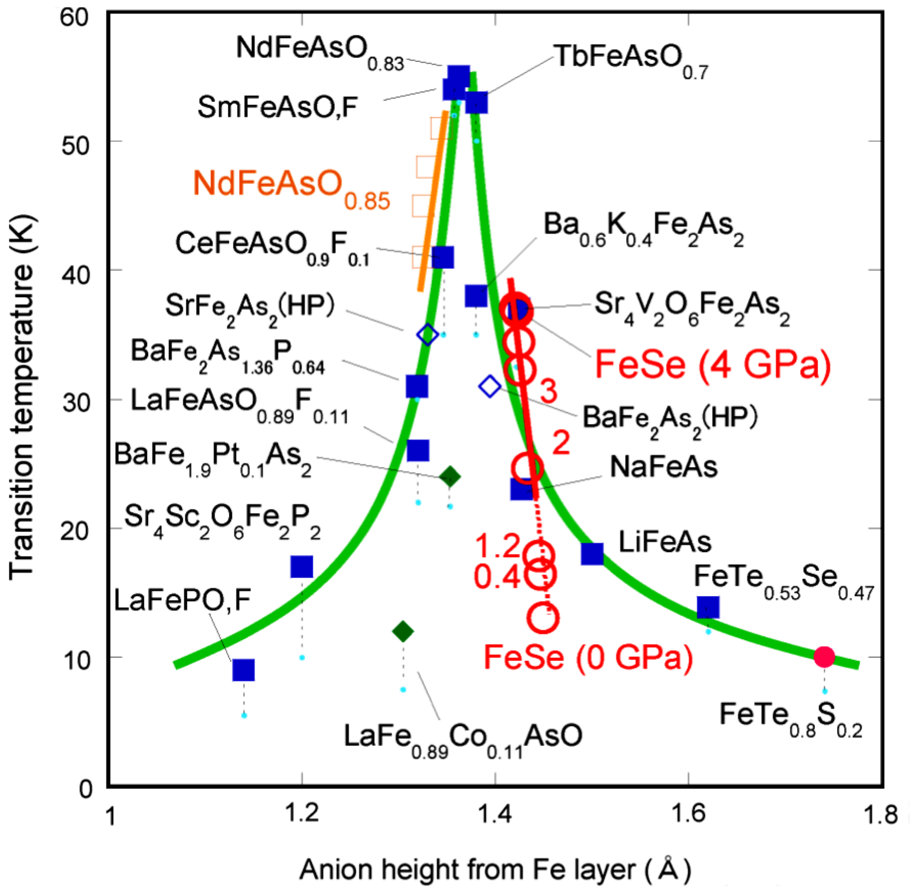

Figure 2.8: Anion height dependence of T_c for the typical Fe-based superconductors. Larger symbols indicate the onset temperature, while the very small light blue circles represent the zero-resistivity temperatures at ambient pressure. Solid and open diamonds indicate the data at ambient pressure and data of $SrFe_2Sr_2$ and $BaFe_2As_2$ under the optimal pressure, respectively. Open squares show the data of $NdFeAsO_{0.85}$ under high pressure. A solid circle shows the data of $FeTe_{0.8}S_{0.2}$ and open circles indicate the data of FeSe under high pressure. Solid green diamonds are the data for Pt-doped $BaFe_2As_2$ and Co-doped LaFeAsO. [76]

to the sign change in the RKKY interaction between the Eu^{2+} ions. Interestingly, a structural study on the EOS of $EuFe_2As_2$ by Uhoya *et al.* [78] up to 70 GPa reports a structural transition from tetragonal to collapsed tetragonal around 8 GPa, showing a large change in the c/a ratio. An x-ray magnetic circular dichroism study reports Eu's valence increases above 4 GPa, reaching $\sim$ 2.5 at 20 GPa, consequently suppressing the ferromagnetism above this pressure [72]. It would be interesting to know whether $EuFe_2As_2$ becomes superconducting above 20 GPa when the magnetism is suppressed. When the compound is doped with P or Co, it was reported that the ferromagnetism from Eu competed with the superconductivity, as the magnetic transition temperature was only a few degrees different from the superconducting transition temperature [79–82]. A complete review of the phase diagram in other Fe-pnictides can be found in References [6, 61, 75].

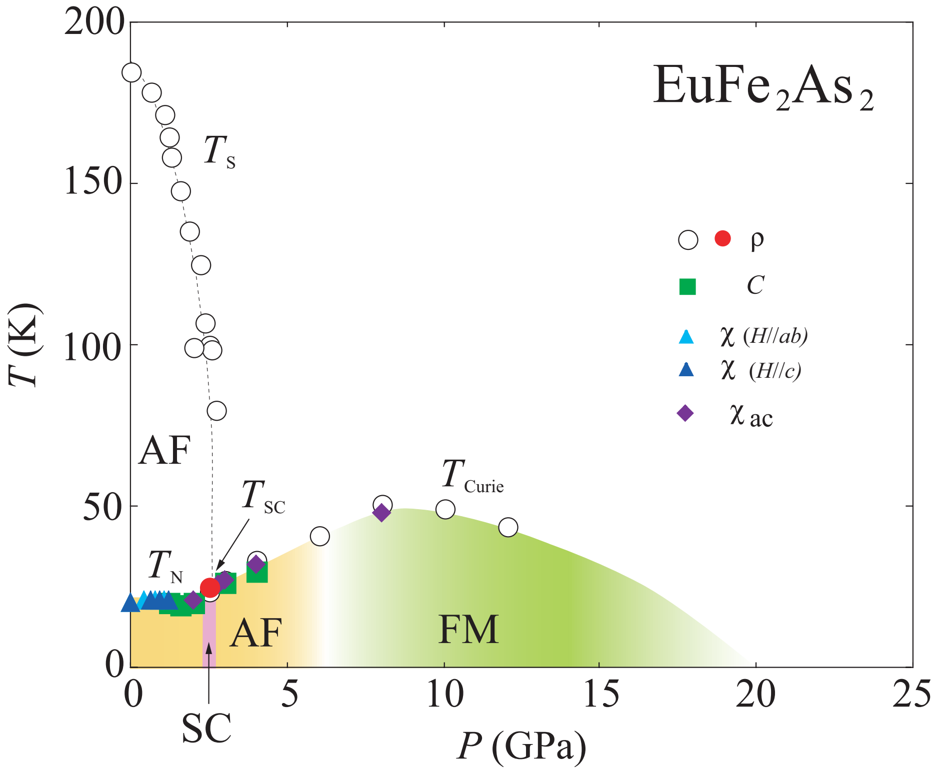

Figure 2.9: Pressure-temperature phase diagram of $EuFe_2As_2$. T_s is the SDW ordering temperature, T_{sc} is the superconducting transition temperature, and T_{Curie} is the Curie temperature. AF and FM represent antiferromagnetic and ferromagnetic ordering, respectively. [72]

Chapter 3

Experimental Methods and Apparatus

In this thesis work, structural, valence, magnetic, and superconducting properties of a few selected materials have been studied under pressure using synchrotron, electrical resistivity, and ac susceptibility techniques. The synchrotron experiments were carried out at a few beamlines at the Advanced Photon Source (APS), Argonne National Laboratory. Ac susceptibility and electrical resistivity experiments were performed here in our lab at Washington University. In this chapter I will discuss the high pressure experimental techniques.

3.1 High Pressure Synchrotron Techniques

3.1.1 X-ray Powder Diffraction

High pressure angle-dispersive x-ray powder diffraction experiments were performed at beamline 16ID-B of the High Pressure Collaborative Access Team (HPCAT) at the Advanced Photon Source (APS), Argonne National Laboratory with the assistance of

Dr. Y. Meng. At HPCAT symmetric cells (see the picture in Figure 3.18) are widely used in diffraction experiments. Pressure can be measured by ruby fluorescence or by measuring in-situ diffraction of a material with a known equation of state under pressure, e.g. NaCl, Au, Ag, Pt or Re.

At HPCAT, in angle-dispersive x-ray diffraction experiments, a monochromatic x-ray beam with wavelength ~ 0.4 Å is normally used. At this energy ($\sim$ 30 keV), the x-ray intensity passing through the diamond and the sample is high enough that sufficient data can be collected within the angular limits of the pressure cell. To achieve Mbar pressures, the sample size is typically less than $100\mu m$. Therefore, the x-ray beam is focused down to be smaller than 10 μm at the sample position. The small beam reduces the sampling pressure gradient and allows accurate determination of the critical pressure for a given phase transition. However, even with this small beam size, sometimes diffraction peaks from the gasket material are still observed under pressure because the shape of the gasket hole becomes irregular. Diffraction patterns are collected using an image plate detector (MAR345), typically with an exposure time of a few seconds. Before each experiment, a NIST CeO_2 standard is normally measured. Based on the diffraction pattern of CeO_2 the sample-to-detector distance is precisely calibrated in FIT2D software [83]. The two-dimensional diffraction image from the sample is then integrated to give intensity as a function of diffraction angle (2θ) in FIT2D. Figure 3.1 shows diffraction images and the corresponding integrated spectra of Eu at 4 GPa and 14 GPa. Larger diameter rings corresponding to higher angles in the diffraction image are only partial due to a slot opening in the WC diamond support, which will be discussed in Section 3.2.

In high pressure experiments, if the structure of the sample is known, the equation of state can be obtained by refining the cell parameters from the peak positions using the least-square method. Programs such as UNITCELL, MDI Jade, and POWDERCELL, *etc.* can be used to accomplish this task. However, very often unknown phases induced by pressure or temperature are observed in experiment. It is a difficult task to solve unknown phases, especially when the symmetry is low. The phase determination in this thesis work has been done with the help of R. Kumar and Y. Meng.

To identify an unknown phase, the diffraction spectrum can be indexed with the help of indexing software, such as MDI Jade, which was used in this thesis research or CRYSFIRE. After pattern-indexing possible structure models are listed with possible space groups. In high pressure experiments, some of the hundreds of possible structure models can be ruled out based on the value of the volume per formula unit, since the atomic volume must decrease under compression.

Keeping in mind some top candidates, a structureless fitting called Le Bail fitting is normally performed to get a background and diffraction profile fit. Le Bail type fitting differs from the more rigorous structurally based Rietveld fitting. It extracts peak intensities directly from the experimental data through profile fit, rather than from a structural model. Therefore, if the space group assignment is correct, the cell parameters are refined and the profile will fit well with the data. This can be done in programs like LHPM-RIERICA [84] and GSAS [85]. After the cell and peak parameters are optimized, parameters related to the atomic position can be refined using Rietveld

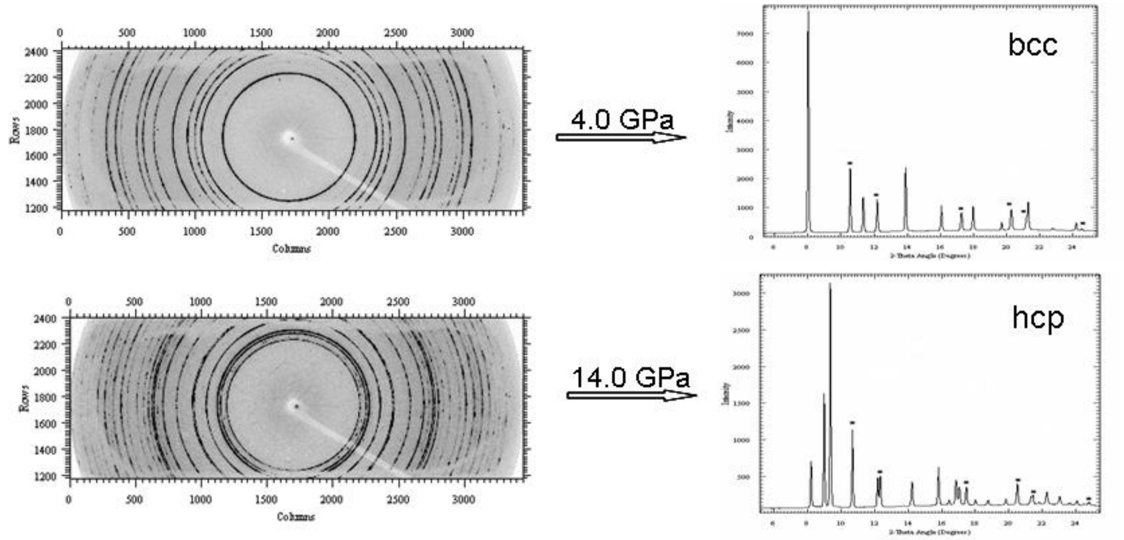

Figure 3.1: X-ray diffraction images of the Eu sample and Pt pressure marker at 4 GPa (in bcc phase), 14 GPa (in hcp phase) with $\lambda = 0.41493$ Å beam and 2 s exposure time.

refinement based on the information in International Tables for Crystallography [86]. For further details on the Le Bail and Rietveld refinements, an excellent resource of x-ray powder diffraction lectures and demos by Brian H. Toby can be found in Reference [87].

3.1.2 X-ray Absorption Near Edge Structure (XANES)

When x-rays are absorbed by an atom, the atom is excited with one of the core electron levels left empty (core hole) after a photo-electron is emitted. The core hole is subsequently filled with an electron either by emission of a fluorescence photon (characteristic radiation), or by emission of an Auger electron. This process is illustrated in Figure 3.2.

The x-ray intensity after passing a homogeneous sample with thickness x is given as [88, 89]

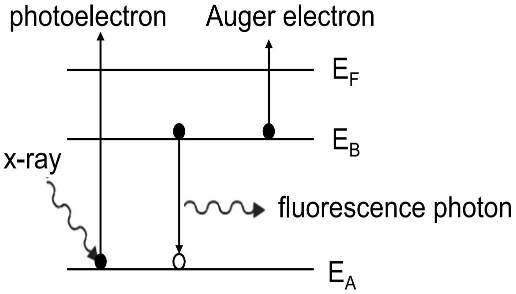

Figure 3.2: Energy diagram of the photo-absorption process and the subsequent filling of the core hole. E_A, E_B, and E_F are the core level A, B and fermi energy level, respectively.

$$I = I_o e^{-\mu x} \tag{3.1}$$

where I_0 and I are the x-ray intensity before and after the sample respectively, μ is the linear absorption coefficient and is dependent on x-ray energy and sample density. At certain x-ray energies, the absorption shows a series of sharp discontinuities (see in Figure 3.3). The sharp discontinuities are called *K, L, M,* etc., absorption edges, where the *K, L, M, ...* designation corresponds to the principal quantum number $n =$ 1, 2, 3, ... The absorption edge energies are the binding energies of electrons in the *K, L, M,* etc. shells. They are labeled in the order of increasing energy as K, L_I, L_{II}, L_{III}, M_I, ..., corresponding to the excitation of an electron from the $1s$, $2s$, $2p_{\frac{1}{2}}$, $2p_{\frac{3}{2}}$, $3s$, ... orbitals to a continuum state (see in Figure 3.4).

Since the binding energy of an electron in a given atomic shell is well defined and depends on its interaction with the core and all the other electrons, the absorption edge energy is a signature of the atomic species. Therefore, this technique is element

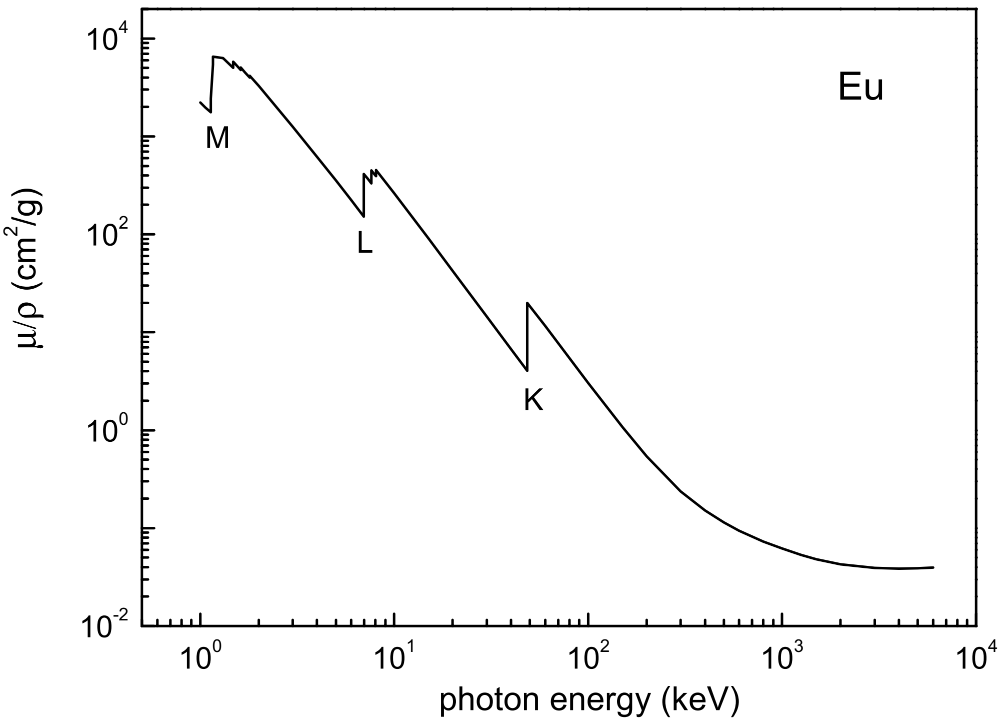

Figure 3.3: Absorption coefficient of Eu as a function of incident photon energy. The sharp discontinuities are the absorption K edge, three L (L_I, L_{II}, L_{III}) edges, and five M edges in the plotted energy range. Data are from Reference [100]. $\rho = 5.25$ g/cm^3.

specific. The position of the absorption edge depends on the resonant energy of the core state. The transition probability from a initial state $|i>$ to a final state $|f>$ is given by the Fermi Golden rule [90],

$$\Gamma_{i,f} = \frac{2\pi}{\hbar}\sum_{i,f} | < f|\overrightarrow{r} \cdot \overrightarrow{\varepsilon}|i > |^2 \delta\left(E_f - E_i - \hbar\omega\right) \tag{3.2}$$

where $\overrightarrow{\varepsilon}$ is the x-ray electric field vector and $\hbar\omega$ is the photon energy. The transition follows the electric dipole selection rules ($\triangle l = \pm 1$). The selection rules require that the final state for K and L_I edges is a p state, and an s or d state for L_{II} and L_{III} edges.

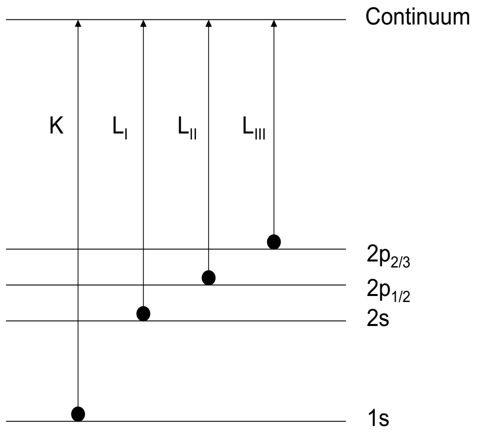

Figure 3.4: Diagram for K, L_I, L_{II}, L_{III} absorption edges.

Typically when the x-ray photon energy is $\leq$30 eV above the absorption edge energy, the emitted photoelectron can populate the unoccupied bound states or the low lying continuum states. This part of the absorption spectrum is called x-ray absorption near edge structure (XANES). In this region, the electron's kinetic energy is small and the scattering on the neighboring atoms is strong. Multiple electronic scattering events can occur. Therefore, the XANES spectrum depends not only on the electronic structure (valence and density of states) but also on the local symmetry around the absorbing atom and thus is sensitive to the structure phase transitions induced by pressure and temperature [94]. It is often interpreted by simulation. In this thesis work, XANES was used in studies of Eu's valence change under pressure, so XANES experiments at Eu's L_{III} edge will be discussed in detail.

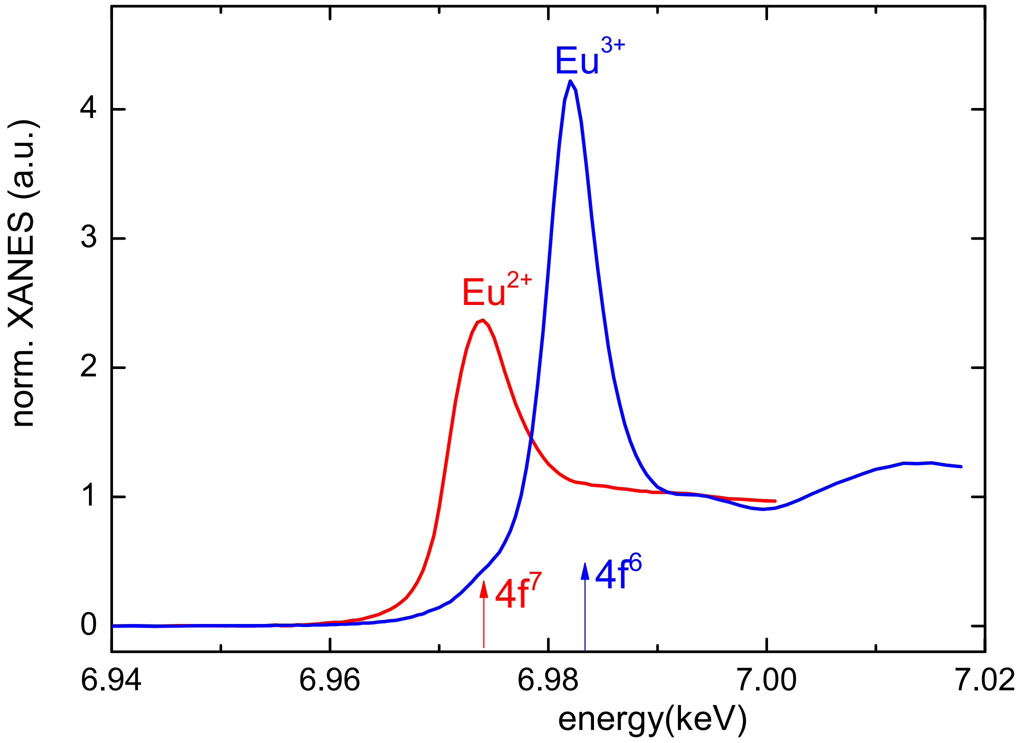

Figure 3.5: X-ray absorption spectra at Eu's L_{III} edge for Eu^{2+} and Eu^{3+}.

High Pressure XANES Experiment

The absorption peak at L_{III} edge in divalent Eu metal corresponds to the transition $2p^6_{3/2}4f^75d^06s^2 \rightarrow 2p^5_{3/2}4f^75d^16s^2$ and in trivalent Eu in Eu_2O_3 to $2p^6_{3/2}4f^65d^16s^2 \rightarrow 2p^5_{3/2}4f^65d^26s^2$ transition. As seen in Figure 3.5, the energy of the absorption peak from trivalent Eu is ~8 eV higher than the one from divalent Eu. If Eu becomes trivalent under pressure, the absorption peak energy is expected to shift up by 8 eV. When Eu is in mixed-valent state, a spectrum based on the superposition of two peaks (one located at Eu^{2+} resonant energy and one at Eu^{3+} energy) is expected.

Two geometries are typically used in x-ray absorption experiments: transmission and fluorescence. In transmission geometry the absorption is directly measured from the x-ray intensity transmitted through the sample according to $\mu \propto -\ln(I/I_0)$. In fluorescence geometry, on the other hand, the absorption is measured from re-filling the core hole based on $\mu \propto I_f/I_0$, where I_f is the intensity of the fluorescence [96]. Fluorescence detection is normally used in dilute systems or thin samples. In a concentrated or thick sample, however, it can yield a distorted spectrum due to the self-absorption effect in the sample [97]. In this case, transmission geometry is normally used. However, enough transmission through a sample has to be obtained to get a decent signal I. The sample thickness should meet two criteria, $\mu x \sim 2.5$ [98] to achieve an optimal signal-to-noise ratio and $\Delta\mu x < 1.5$, where $\Delta\mu$ is the edge step, to avoid spectrum distortion from thickness effects [99]. At Eu's L_{III} edge, setting $\mu x \sim 2.5$ with $\mu/\rho = 412.7$ cm^2/g [100] and ρ =5.25 g/cm^3 [101] gives $x \sim 12$ μm, while setting $\Delta\mu x < 1.5$ with $\Delta\mu/\rho = (412.7-152.2)$ cm^2/g = 269.5 cm^2/g gives ~ 11 μm. Therefore, the Eu sample should be thinner than 11 μm. However, in high pressure experiments it is difficult to control the sample thickness since the sample gets thinner and thinner upon applying pressure, from an initial thickness of 30-50 μm to 5-10 μm at the highest pressures in 180 μm anvils. Due to the large change in sample thickness, it may be too thick at ambient pressure and become too thin at high pressure. To solve this problem, both foil samples with Eu thickness 5 μm and bulk samples were used in the experiments to 87 GPa. More details will be discussed in section 4.2.1.

A sketch of the setup at synchrotron beamlines at the APS is shown in Figure 3.6. A double crystal monochromator is normally used to tune the x-ray to the desired energy. The beam size is reduced at the sample position with a slit or Kirkpatrick-Baez (KB) mirrors [102]. In transmission geometry, the incident x-ray intensity I_o, transmitted

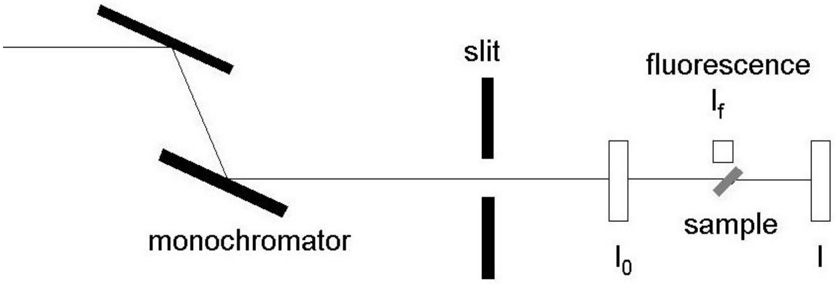

Figure 3.6: Schematic drawing of XANES experiment setup.

intensity I are measured simultaneously in the beam path. If fluorescence geometry is used, I_f is measured perpendicular to the beam.

For high pressure experiments using a diamond anvil cell, x-rays must pass through both diamonds. At certain energies diffraction of the incident beam by the single crystalline anvils occurs according to Bragg's law, resulting in deviation of the beam away from the incident beam path at those energies. The corresponding photons will not be able to reach the detector, resulting in "glitches" or spurious sharp peaks which appear in the absorption data (see in Figure 3.7). The number and intensity of these "glitches" is dependent on the orientation of the diamonds with respect to the incident beam and, of course, the energy range of interest. During an experiment, a quick scan of the spectrum is normally done to check this. If the diamond Bragg peaks are present, the diamond anvil cell has to be carefully rotated to move the peaks out of the spectral energy range.

Another issue with using diamond anvils in high pressure experiment is the strong

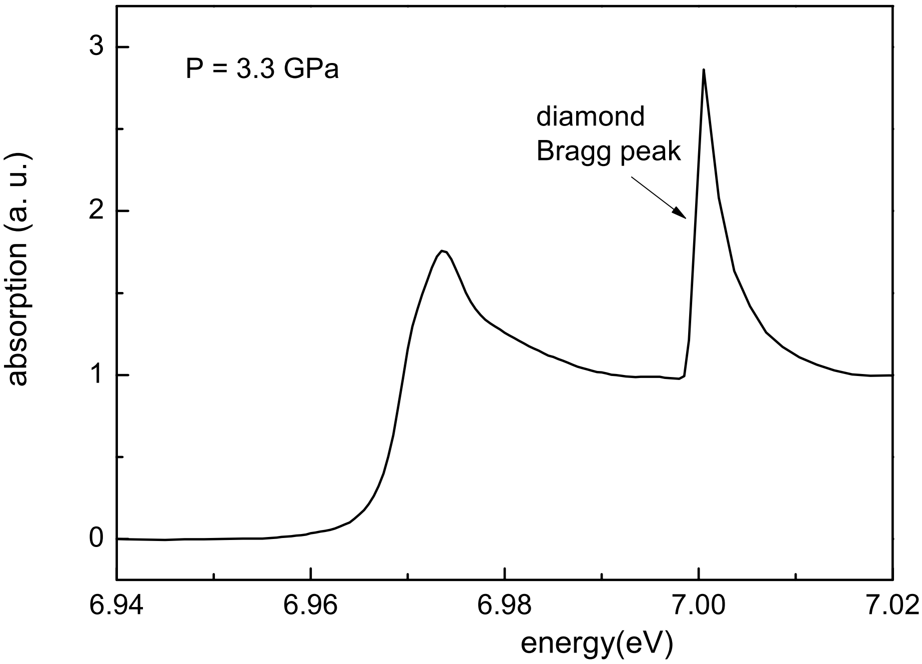

Figure 3.7: XANES spectrum of Eu at the L_{III} edge with a diamond Bragg peak.

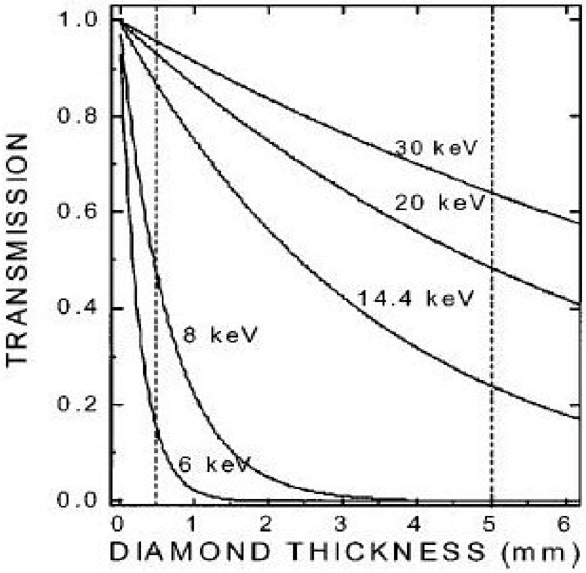

Figure 3.8: X-ray transmission versus diamond thickness at different photon energies [92].

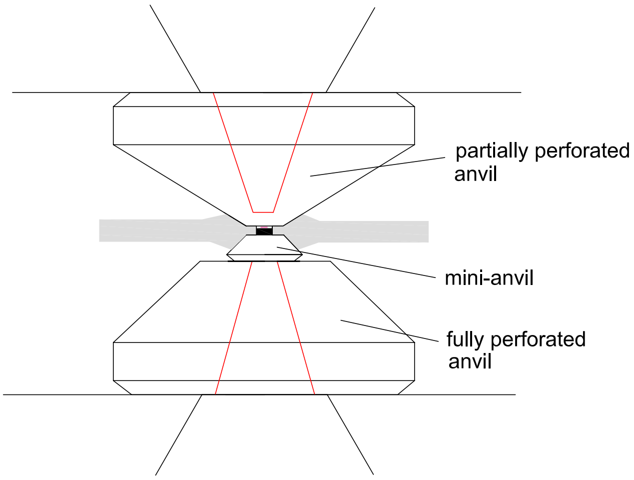

Figure 3.9: A sketch for experiment setup using one mini-anvil and a fully perforated anvil on one side and a partially perforated anvil on the opposing side.

diamond absorption at low photon energies. Figure 3.8 shows the relative transmission through diamond for different photon energies. The lower the photon energy, the lower the transmission through the diamond. For one pair of $\frac{1}{6}$ carat anvils with $\sim$ 4 mm combined thickness, the transmission of x-ray with energy near Eu's L_{III} edge energy at 6.97 keV is only $\sim 10^{-4}$. Sufficient transmission is important in the XANES experiment at Eu's L_{III} to reduce the data collection time. Therefore, to improve the transmission, a mini-anvil (thickness $<$ 1 mm) glued on a fully perforated anvil on one side, and a partially perforated anvil with inner wall of 0.1-0.15 mm thick on the opposing side are normally used (see Figure 3.9) [92, 93]. With 0.8 mm total diamond in the x-ray path, the transmission at 7 keV is $\sim$ 17%. However, since the mini-anvil sits directly on top of the fully perforated anvil, it is challenging to achieve pressures higher than 50 GPa.

Another possibility is to use one full anvil and one partially perforated anvil (Figure 3.10). The x-ray transmission through the diamonds is $\sim 10^{-2}$. The transmitted photon counts are much lower than the setup with mini-anvil but it is possible to achieve higher pressures. This setup was used in a room temperature XANES experiment up to 87 GPa which will be described in Section 4.2.1 and a low temperature XMCD experiment to 60 GPa which will be discussed in Sections 3.1.3 and 4.2.2.

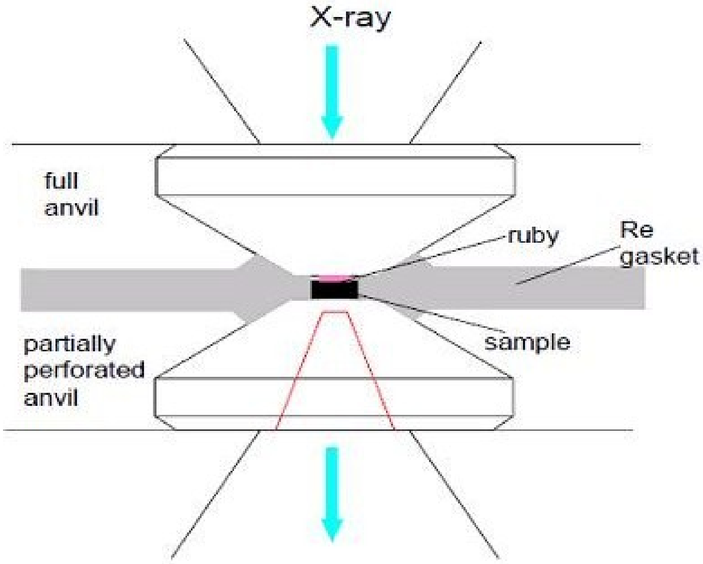

Figure 3.10: Sketch of one full anvil and one partially perforated anvil. The smooth optical surface on the full anvil side allows pressure measurement by ruby fluorescence.

3.1.3 X-ray Magnetism Circular Dichroism (XMCD)

In circularly polarized x-rays the electromagnetic field vector rotates around the propagation vector direction. Circularly polarized photons carry helicity (±1), i.e. a well defined projection of angular momentum along its propagation direction. XMCD uses a circularly polarized x-ray beam with energy near the absorption edge. The Fermi Golden rule in Equation 3.2 requires additional selection rules $\Delta m = \pm 1$ besides $\Delta l = \pm 1$ [90]. In the absorption process, the helicity is transferred to the spin of electrons. Opposite helicity generates opposite spin-polarization in the excited electrons. Magnetic materials have an imbalanced spin-up and spin-down unoccupied final states, giving a difference in the absorption cross section for opposite x-ray helicities. As seen in Figure 3.11 in Eu, for example, the 5d final states is split by spin-up and spin-down states by the intra-atomic $4f$-$5d$ exchange interaction. At L_{III} edge, a left circularly polarized (LCP) photon has a higher possibility to excite a spin-up photo-electron (62.5% of possibility) than to excite a spin-down photo-electron (37.5% of possibility), while a right circularly polarized (RCP) photon has a higher possibility to excite a spin-down photo-electron [90].

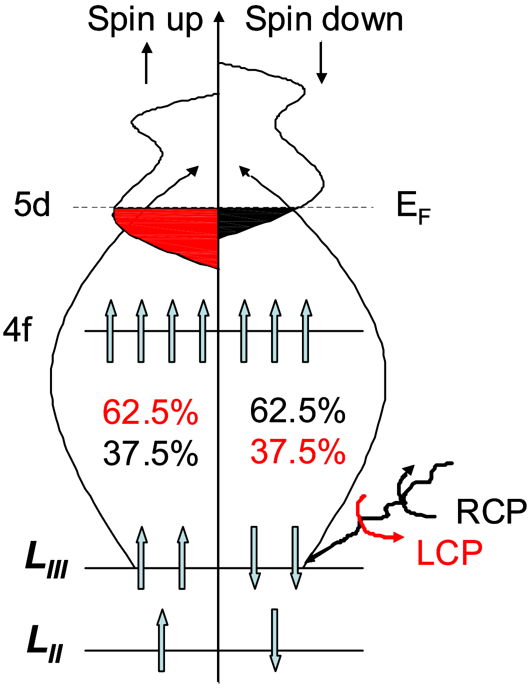

Figure 3.11: Schematic sketch of the electronic transitions for XMCD at Eu's L_{III} edge. The final state $5d$ band is split between spin-up and spin-down states by the intra-atomic $4f$-$5d$ exchange interaction.

The XMCD signal is defined as the difference in the absorption coefficient (μ) of magnetic atoms for left (μ^+) and right (μ^-) circularly polarized x-rays

$$\mu_{XMCD} = \mu^+ - \mu^-, \tag{3.3}$$

and $\mu_{XMCD} \propto \rho(\uparrow) - \rho(\downarrow) \propto M$, where $\rho(\uparrow)$ and $\rho(\downarrow)$ are the spin-up and spin-down densities of state, and M is the magnetization in the sample. The XMCD signal is normalized by the absorption edge jump obtained from the XANES spectrum $\mu_{XANES} = (\mu^+ + \mu^-)/2$.

In transition metal atoms and rare earth atoms, the XMCD signal is normally measured at $L_{II,III}$ ($2p \rightarrow 3d$ transition) and at $M_{IV,V}$ ($3d \rightarrow 4f$ transition) edges. Since the $3d$ states for transition metals or $4f$ states for rare earth systems carry most of the magnetization of the material, the direct probing of the spin polarization yields the largest dichroic effects. However, the excitation energies at M edges are in the range of 500-1500 eV and are too low for high pressure experiments in a diamond anvil cell. On the other hand, the relatively higher energies of transition metal K ($1s \rightarrow 4p$) edges and rare earth $L_{II,III}$ ($2p \rightarrow 5d$ transition) edges in the range of 5000-9000 eV, are more suitable for high pressure studies in DAC. However, the spin polarization in $4p$ and $5d$ states is much weaker, giving a XMCD signal of only $\sim 0.2\%$ - 6% of the absorption jump [103, 106].

In rare earth metals, the spin polarization in $5d$ states comes from the $4f$-$5d$ exchange interaction [106, 107]. XMCD at the $L_{II,III}$ edges has been used in studying the magnetic and valence state in Eu systems [72, 108–110]. In this thesis research, XMCD at the L_{III} edge was used to probe the change in pressure-induced magnetism in Eu metal. Since Eu orders antiferromagnetically below 90 K at ambient pressure, the induced spin polarization in 5d states is much smaller than in ferromagnetic and ferrimagnetic materials. A large magnetic field has to be applied to obtain a sufficiently large XMCD signal. In the experiments, XMCD spectra were measured in a 4 T magnetic field and at 4.6 K.

High-Pressure XMCD Experiment Setup

There are four key ingredients in XMCD experiments: (1) a source of circularly polarized x-rays, (2) a monochromator, (3) magnetized sample which gives imbalanced spin-up and spin-down states, and (4) an x-ray absorption detection system.

The XMCD experiment on Eu metal was carried out at beamline 4ID-D, APS. A schematic sketch of the high-pressure experiment setup is shown in Figure 3.12. The linearly polarized x-ray beam was first monochromatized by a Si (111) double-crystal monochromator and then converted to circularly polarized after a diamond crystal phase retarder [105]. The Pd toroidal mirror and Si flat mirror were used to focus the beam at the slit. A split ion chamber was used to monitor and maintain a fixed vertical beam position by adjusting the angle of the second Si crystal in the Si monochromator. The beam size was further reduced to $\sim 12\ \mu m$ by a KB mirror pair without reducing x-ray intensity. A superconducting magnet and He-flow cryostat were used to achieve a field of 4 T and 4.6 K.

Since the bore in the superconducting magnet is only $\sim$ 1 inch, a pressure cell

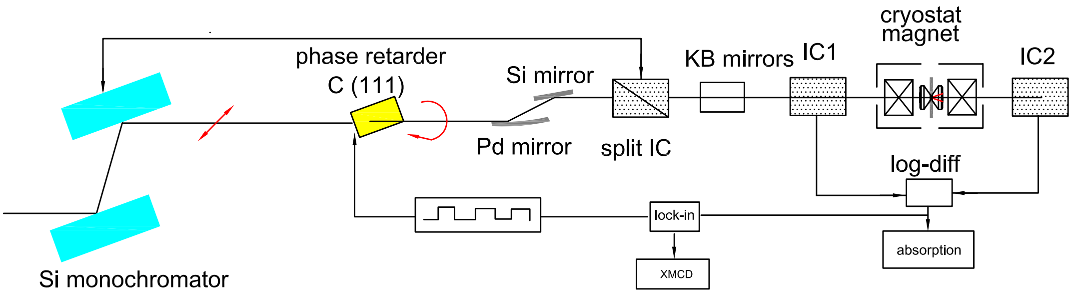

Figure 3.12: Experimental setup for high-pressure XMCD measurements. Modified from Reference [103].

with outer diameter smaller than this has to be used. In Eu XMCD experiments, a piston-cylinder miniDAC with 16 mm outer diameter was used. The pressure cell will be discussed later in Section 3.2.1. The high pressure cell was rotated to minimize the unwanted Bragg peaks from the diamond anvils. The XMCD data were recorded with a lock-in amplifier and in helicity-switching mode with a frequency of 12.7 Hz. The pressure cell had to be warmed up to room temperature in order to change pressure. A more detailed discussion of the beamline setup can be found in Reference [93, 103].

Ideally, changing the magnetic field direction for fixed polarization is equivalent to changing the x-ray helicity for a fixed magnetic field. The XMCD signal in 4 T field should be the same in magnitude but opposite in sign with the one in -4 T field. However, in experiments there are always artifacts in the XMCD signal coming from field/pressure gradient in the sample and impurity in the x-ray polarization, etc. To get rid of the artifacts, a field (4 T) was first applied and absorption was measured as the x-ray helicity is switched at a frequency of 12.7 Hz. Then the field was switched to -4 T and absorption was measured. The final artifact-free XMCD signal was obtained by subtracting the XMCD data with opposite field direction +/- 4 T and divided by two.

3.1.4 Synchrotron Mössbauer Spectroscopy (SMS)

The Mössbauer effect was first discovered in 1957-1958 by Rudolf Mössbauer [111] during his Ph.D. research work in Heidelberg, Germany. In 1961 he was awarded the Nobel Prize for this discovery. In the 50 years following the discovery, Mössbauer spectroscopy has been developed as a powerful tool and been applied to many fields of research. In the following section basics about Mössbauer effect and experimental techniques for conventional Mössbauer spectroscopy and synchrotron Mössbauer spectroscopy will be discussed.

Conventional Mössbauer Spectroscopy (CMS)

The Mössbauer effect results from the recoilless emission and absorption of γ-ray between nuclei. In a free nucleus, when the nucleus emits or absorbs a γ-ray it will recoil due to the conservation of momentum. The recoil energy causes an energy loss in the emitted radiation by E_R and is given by

$$E_R = \frac{E_\gamma^2}{2Mc^2}, \tag{3.4}$$

where E_γ is the γ-ray energy, M is the mass of the nucleus and c is the speed of light. Then the emitted γ ray has energy E_R less than the resonant transition energy. Although E_R is considerably smaller than E_γ, it is large compared to the resonant transition linewidth.

For the resonant transition to happen, the loss of recoil energy must be overcome. In a classical view, the nuclei are rigidly bound in a crystal lattice, and the recoiling mass is the effective mass of the whole system, leading to a very small value of E_R. This is in good analogy [112] with a boy (γ-ray) jumping from a boat (nucleus) and trying to land (be absorbed) on a pier (an excited state of another nucleus). Due to the recoil motion of the boat, the boy's kinetic energy will be reduced by E_R and he would fail to reach the pier. However, if the boat is frozen in the water (bound in a lattice), the recoil energy will be zero, and the boy would land on the pier safely.

However, in reality the nuclei are not rigidly bound, but vibrating about an equilibrium position. Besides the recoil energy loss, the vibration further reduces the γ-ray energy by a doppler energy $E_D = vE_\gamma/c$, where v is the vibrating velocity. In an Einstein solid, the vibrational oscillations have energy levels $\hbar\omega(n+{}^1\!/\!_2)$. When an emission occurs in a nucleus, if E_R is less than the separation of the vibrational levels $\hbar\omega$, the lattice can not absorb the recoil energy. Emission without excitation of phonons in the lattice is zero-phonon transition. The probability of such a process is known as the recoilless fraction, f. In a real solid, the phonon vibrational frequency distribution has to be considered. A quantitative expression for the recoilless fraction is given in the Debye model by

$$f = exp\left[\frac{-6E_R}{k\theta_D}\left\{\frac{1}{4}+\left(\frac{T}{\theta_D}\right)^2\int_0^{\theta_D/T}\frac{xdx}{e^x-1}\right\}\right] \tag{3.5}$$

After a resonant absorption the nuclear excited state will decay to the ground state through γ-ray emission with a mean lifetime τ. The emitted γ-ray energy shows a Lorentzian distribution with a natural linewidth Γ. From the Heisenberg uncertainty principle we have $\tau\Gamma \sim \hbar$.

Another important factor is the effective (maximum) cross-section of the resonant absorption given by

$$\sigma_0 = 2\pi\lambda^2 \frac{2I_e + 1}{2I_g + 1} \frac{1}{1 + \alpha} \tag{3.6}$$

where I_e and I_g are the nuclear spin quantum numbers of the excited and ground states, respectively, and α is the internal conversion coefficient of the γ-ray of wavelength λ. In the absorption process, not only the resonant absorption occurs, but also the electronic scattering, ejecting electrons from the atomic orbitals. The internal conversion coefficient α is defined as the ratio of the number of conversion electrons to the number of γ-ray photons emitted.

To successfully observe the Mössbauer effect in a sample, a few crucial conditions should be satisfied [113,123]:

- The energy of the nuclear transition (E_R) or the $\gamma-$ray energy should be between 10 and 100 keV, preferably less than 50 keV. Below 10 keV, the $\gamma-$ray is strongly absorbed by the sample. If the energy is too high, both the recoilless fraction, f and resonant cross-section σ_0 decrease as E_R increases based on equations 3.5 3.6.

- The half-life of the excited state $t_{\frac{1}{2}}$ ($t_{\frac{1}{2}} \equiv \tau \ln 2$) which determines the linewidth

Γ should be neither too long nor too short (1-100 ns). If $t_{\frac{1}{2}}$ is too long, Γ will be too narrow to measure, and if $t_{\frac{1}{2}}$ is too short then Γ will be too broad to resolve any hyperfine effects.

- The internal conversion coefficient α should be small ($<$10) so that there is a good probability of resonant transition happening to ensure a detectable emitted γ-ray intensity.
- The isotope should have a stable ground state, and have a high enough abundance. If the natural abundance is low, isotopic enrichment is necessary.

In the conventional Mössbauer experiments, a radioactive source is normally used to provide the resonant γ-ray for the absorber (sample). The emitted γ-ray from the source should have the exact energy for the nuclear transition to happen in the absorber. However, the resonant lines from the source and the absorber are extremely sharp and they may not match. To solve this problem the source normally moves at a relative velocity v of the order of 1 mm/s to the absorber. Because of the doppler effect, the γ-ray energy is varied by a small amount $E_\gamma v/c$. By this small adjustment the nuclear transitions in the source and absorber can be accurately matched and resonance occurs.

In the Mössbauer effect, three types of hyperfine interactions play an important role in studying the microscopic environment surrounding a nucleus: electrical monopole interaction (causing isomer shift), magnetic dipole interaction (causing Zeeman splitting or magnetic hyperfine splitting) and electric quadrupole interaction (causing quadrupole splitting of the spectral lines).

The isomer shift, IS, originates from the finite size of a nucleus, which gives an interaction energy between the external electronic charge and the nucleus as a function of nuclear radius. The isomer shift is given by

$$IS = C\frac{\delta R}{R}\Delta\rho_e(0) \tag{3.7}$$

where C is a constant containing nuclear parameters for a given isotope, $\frac{\delta R}{R}$ is the relative change of nuclear radius between excited state and ground state in the absorber, and $\Delta\rho_e(0)$ is the difference in the s-electron density at the nucleus in the source and absorber material. The isomer shift is also determined by the sign of the $\frac{\delta R}{R}$. If $\frac{\delta R}{R}$ > 0, a positive isomer shift implies that in the absorber the s-electron density at the nucleus is higher than in the source. For $\frac{\delta R}{R} < 0$, this is reversed. The last term is not only affected by the number of s-electron population in the atom, but also by the screening effects of p-, d- and f-electrons and by chemical bonding. Under pressure, all the s-electron shells ($1s$, $2s$, $3s$ ...) contribute to the change in IS, but only the outermost occupied s-orbital have a significant effect.

When a magnetic field H is present at the nucleus, the interaction of the nuclear magnetic dipole moment μ with the magnetic field splits the nuclear state with spin I to $2I + 1$ sublevels with the eigenvalues

$$E_m = \frac{-\mu H m_I}{I} = -g\mu_N H m_I \tag{3.8}$$

where $\mu_N = e\hbar/2Mc$ is the nuclear Bohr magneton, μ is the nuclear magnetic moment,

$g = \mu/(I\mu_N)$ is the Landau g factor , and $m_I = I$, $I-1$,..., -I is magnetic moment number. The transition between different sublevels occurs when $\Delta m_I = 0$, ± 1.

The interaction of the nuclear electric quadrupole moment eQ with the diagonalized electric field gradient tensor $V_{zz} = \partial^2 V/\partial z^2$ at the site of the nucleus splits the nuclear state into sublevels with the eigenvalues

$$E_Q = \frac{eQV_{zz}}{4I(2I-1)}\left[3m_I^2 - I(I+1)\right]\left(1+\frac{\eta^2}{3}\right)^{1/2}. \tag{3.9}$$

The asymmetry parameter η is defined as

$$\eta = \frac{V_{xx} - V_{yy}}{V_{zz}} \tag{3.10}$$

and $0 \leqslant \eta \leqslant 1$. For $I = \frac{1}{2}$, there is only one level, but for $I = \frac{3}{2}$ there are two distinct eigenvalues with $m_I = \pm\frac{3}{2}$ and $m_I = \pm\frac{1}{2}$. For a detailed discussion about the nuclear hyperfine interactions please refer to Mössbauer Spectroscopy by Greenwood and Gibb [123].

In this thesis research the Mössbauer effect is used primarily to study the valence change of Eu metal under pressure by measuring the pressure-induced isomer shift. Parameters of ^{151}Eu commonly used in Mössbauer spectroscopy are listed in Table 3.1 in comparison with the mostly studied isotope ^{57}Fe.

The Mössbauer spectroscopy has been proven to be an effective tool to probe the hyperfine interactions in an atom because of its outstanding energy resolution, in the case of ^{151}Eu, $\Gamma/E_0 = 4.70\times10^{-8}$ eV/21.5 keV $\approx 2.2\times10^{-12}$. In ^{151}Eu Mössbauer experiments,

Isotope	E_0(keV)	Γ(neV)	$t_{\frac{1}{2}}$ (ns)	Abund. (%)	α	σ_0 (10^{-20}cm^2)
^{57}Fe	14.41	97.8	4.665	2.14	8.21	255.7
^{151}Eu	21.54	47.0	9.7	47.8	28.6	23.8

Table 3.1: Parameters of ^{151}Eu and ^{57}Fe [122]. Γ is the natural linewidth, $t_{1/2}$ is the half-life, abund. is the natural abundance, α is the internal conversion coefficient, and σ_0 is the effective cross-section.

the $\frac{7}{2} \rightarrow \frac{5}{2}$ transition at 21.54 keV is mainly studied. When divalent Eu is transformed to mixed-valent or trivalent state under pressure, the change in the electronic configuration induces a change in the s electron density at the nucleus resulting in an isomer shift. The phenomena of mixed-valence, temperature- and pressure-dependent valence transition in various Eu compounds have been studied comprehensively using the Mössbauer spectroscopy technique [124].

In ^{151}Eu CMS experiments ^{151}Sm is commonly used as the source. The decay scheme of ^{151}Eu from its parent nucleus ^{151}Sm is shown in Figure 3.13. The long lifetime of the radioactive source ^{151}Sm makes it convenient to measure the Mössbauer spectroscopy in ^{151}Eu. However, the relatively short lifetime of ^{151}Eu gives a rather large natural linewidth and the high spin of the nuclear state makes it difficult to resolve any quadrupole splitting [121]. In this case, synchrotron Mössbauer spectroscopy (SMS) with better energy resolution was used in our experiments to study Eu's valence transition under pressure.

Synchrotron Mössbauer Spectroscopy (SMS)

Synchrotron radiation is generated by charged particles moving at a relativistic speed. At APS, the electrons are first accelerated to 450 MeV in the linear accelerator and

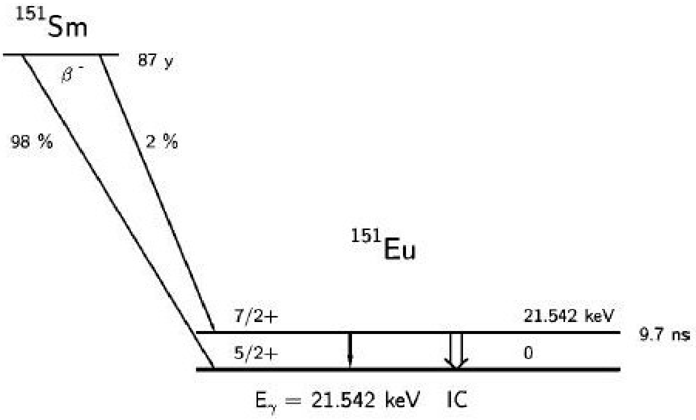

Figure 3.13: Partial decay scheme for ^{151}Eu from ^{151}Sm [121].

then boosted to 7 GeV in 0.5 s. The 7 GeV electrons are injected into the 1104 m circumference storage ring. In the storage ring, the electrons occupy 1296 stable positions in the orbit called buckets. The buckets are separated by 1104/1296 = 0.85 m or 2.84 ns. Electrons fill the buckets as bunches with 23 bunches in each bucket and a separation of 152 ns. When the electrons pass through the spatially periodic magnetic field (undulator), an intense x-ray pulse with a duration of 70 ps is produced. In an SMS experiment it is critical that the time between bunches is longer than the detector dead time ($\sim$ 20 ns) and comparable or longer than the nuclear lifetime in order to obtain appreciable signal counts [114].

After the nuclei are excited to the excited state by an x-ray pulse with the resonant energy, the nuclei will decay into the ground state. During this process, it may emit a photon, 21.5 keV in the case of ^{151}Eu, or transfer the excitation energy to electron shell causing electronic scattering. The electronic scattering normally happens promptly ($< 10^{-12}$ s) after the nucleus is excited, and has an intensity almost 10 orders of magnitude higher than the resonant scattering, while the nuclear resonant scattering is delayed because the typical lifetime (10's of ns) is long compared to the incident radiation pulse.

A schematic of the experimental setup [114] at beamline 3-ID, APS is shown in Figure 3.14. The synchrotron radiation from the undulator has a rather broad energy range. The x-ray is tuned in two steps through a premonochromater (PM) and a high-resolution manochromater (HRM). After HRM the x-ray is tuned to the sample's resonant energy and kept stable at this energy. The x-ray excites the resonant nuclei in the sample and re-emits radiation which is detected by the avalanche photodiode detector (APD) [125] with time resolution ~ 1 ns. The timing circuit measures the time elapsed since the x-ray pulse and filters the prompt nonresonant electron scattering. The delayed events are then collected as a function of elapsed time between the excitation and the re-emission, giving the Mössbauer spectrum of the nuclei in the time domain. For a more detailed discussion of the setup please refer to References [114,115].

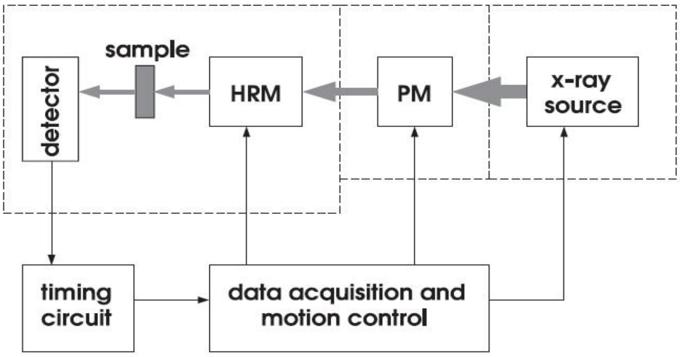

Figure 3.14: SMS experiment setup [114]. Thick grey arrows indicate the x-ray beam. Thin black solid lines symbolize the flow of data or control information. The dashed lines indicate lead enclosures for protection of experimenters from exposure to the x-rays.

To evaluate the SMS data, a CONUSS program developed by W. Sturhahn and E.

Gerdau [117, 118] is widely used. In CONUSS, a set of hyperfine parameters together with the coordinates of the sample Mössbauer atoms (^{151}Eu) in the unit cell are assigned as one site, and the parameters from the reference material as the second site. In SMS data analysis, the sample interaction parameters (isomer shift, quadrupole splitting, magnetic hyperfine field, etc.) and the physical properties (texture, thickness etc.) can be refined. Through Fourier transformation the time domain spectrum in SMS can also be converted to energy domain as is measured in CMS .

A Comparison of CMS and SMS

In SMS experiments, the synchrotron radiation at the resonant energy is used to excite the nucleus in the sample, whereas a radioactive source is used for CMS. Compared to the radioactive source the synchrotron radiation has a unique time structure, high intensity, and adjustable energy for different isotopes, and is highly polarized and suitable for a small beam and thus small samples in high pressure experiment [116]. Figure 3.15 illustrates the principle of the CMS and the SMS [114]. In CMS, the isomer shift is observed between the source and the absorber. A radioactive source moving at a speed v relative to the absorber causes a small shift in the γ-ray energy by $E_\gamma v/c$ due to the doppler effect and therefore a perfect resonant energy is achieved for the absorber. The absorption is measured as a function of the doppler velocity, which is equivalent to energy when multiplied by a factor E_γ/c (energy domain). In contrast to the CMS, a short x-ray pulse at the resonant energy is used to excite the nucleus in SMS. The delayed resonant scattering from the decay to the ground state is collected

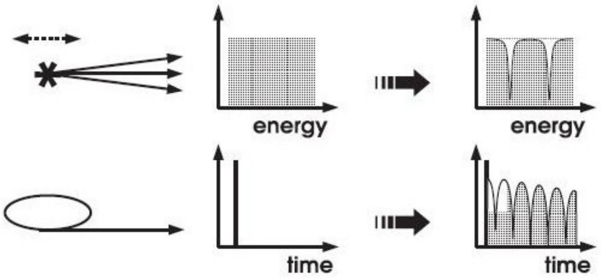

Figure 3.15: Illustration of conventional Mössbauer spectroscopy (top row) and synchrotron Mössbauer spectroscopy (bottom row) [114]. In CMS, a vibrating radiactive source is used and the absorption is measured in energy domain. In SMS, a synchrotron radiation source is used to measure the decay of the resonant scattering in time domain. For more discussion please see the text.

as a function of time elapsed after the excitation (time domain). In SMS experiments, the isomer shift is measured with respect to a reference scatter in the time domain by placing both the sample and the reference material in the x-ray beam path.

Agreement between SMS and CMS has been explicitly demonstrated with a powdered sample [119]. ^{151}Eu has lifetime of 14 ns, which is much shorter than the bunch separation (153 ns) and suitable for SMS studies at the APS. SMS is superior to CMS in high pressure experiments for several reasons:

- Isomer shift accuracy is improved since the nuclear decay data are measured over several lifetimes.
- A significantly smaller beam size (10 μm) avoids the complication of pressure gradient present in the DAC.
- The combination of in-situ x-ray diffraction and Mössbauer data provides unprecedented accuracy in both pressure and isomer shift scales.

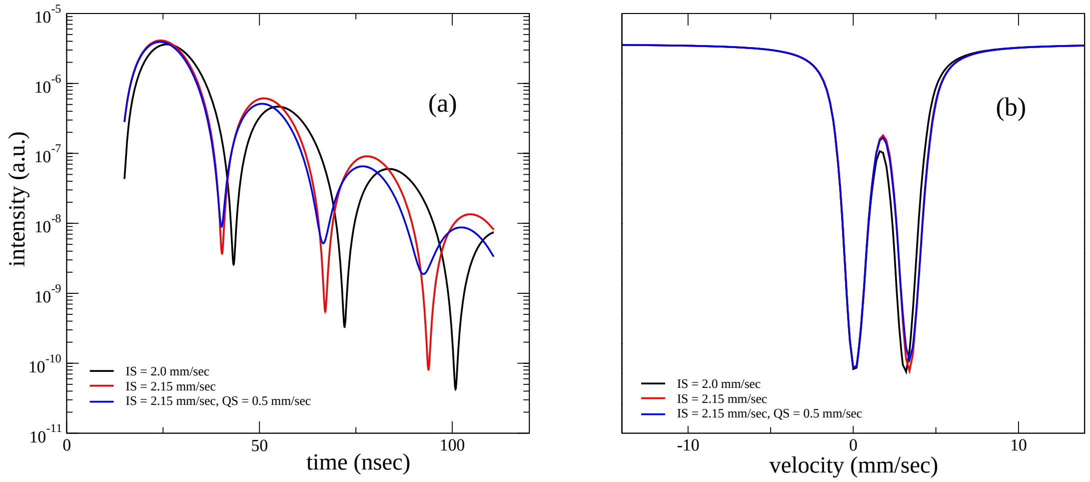

Figure 3.16: Simulations of Mössbauer spectra in time (a) and energy domain (b). The spectra in time domain has much higher sensitivity with the same parameters tuned in energy domain.

- Significantly reduced data collection time (from days to hours) allows scanning of a large pressure and temperature range.

The natural linewidth for the 21.5 keV resonance of ^{151}Eu isotope is 4.70×10^{-8} eV (or 0.654 mm/sec), corresponding to a half-life of 9.7 ns. From the energy conversion 1 mm/s $= 7.1823\times10^{-8}$ eV [120], the linewidth is 37.67 ns. If the isomer shift changes by 0.15 mm/sec in energy domain, which is almost $\frac{1}{4}$ of one linewidth, in time domain it corresponds to 9.4 ns, almost one half-life. In the time of one half-life, there are normally a few beating sites within which 9.4 ns change makes a rather big difference in the spectrum. Therefore, time domain Mössbauer spectroscopy (SMS) has a much higher resolution to measure sample dependent properties including isomer shift, quadrupole splitting, texture, *etc.* compared to energy domain Mössbauer spectroscopy (CMS).

Figure 3.16 shows simulations of the Mössbauer spectra in both time and energy domain with Eu site 1 located at 0 mm/sec and Eu site 2 at 2.0 mm/sec, 2.15 mm/sec and with quadrupole splitting 0.5 mm/sec. It can be seen that changes observed in the time domain are much more drastic than those observed in the energy domain. In the time domain, the spectra change significantly when the parameters are tuned. Therefore, it is possible to fit the data and extract the parameters more accurately. However, in the energy domain, changing the isomer shift of Eu site 2 by 0.15 mm/sec or turning on quadrupole splitting of 0.5 mm/sec results in a much smaller change in the spectrum.

3.2 Diamond Anvil Cell

3.2.1 Diamond Anvil Cells

The diamond anvil cell (DAC) was invented more than 50 years ago by A. V. Valkenburg, C. E. Weir, E. R. Lippincott, and E. N. Bunting at the National Bureau of Standard (NBS), following the work of Percy Bridgman at Harvard. Since then, the high pressure field has flourished and been greatly revolutionized, extending the pressure from a few GPa in the Bridgman cell to multi-Mbar (a few hundred GPa). For an excellent review of the history of diamond anvil cell, please refer to Reference [130].

Different research areas have different requirements on the design of a diamond anvil cell. For example, in x-ray diffraction studies, a wide opening in the diamond anvil cell is desired in the x-ray path. For magnetic susceptibility studies and studies requiring a high magnetic field, a pressure cell made of a nonmagnetic material is desired. In addition, the dimension of the cell is strongly limited by the environment the cell will be used in, for example the inner diameter of the cryostat in low temperature experiments. A few different diamond anvil cell designs were used in the experiments carried out in this dissertation. In ac susceptibility and electrical resistivity experiments carried out at Washington University, a nonmagnetic diamond anvil cell designed by J. S. Schilling was used. This cell is made of Cu:Be alloy, except for parts near the sample and pickup coils which are made of nonmagnetic Cu:Be. A cross-section view of the cell is shown in Figure 3.17. To achieve high pressure and ensure the stable alignment of the two anvil culets, the difference between the piston diameter and the cell bore must be less than $\sim 10\ \mu m$. However, over time the piston gradually wears and the fit between the piston

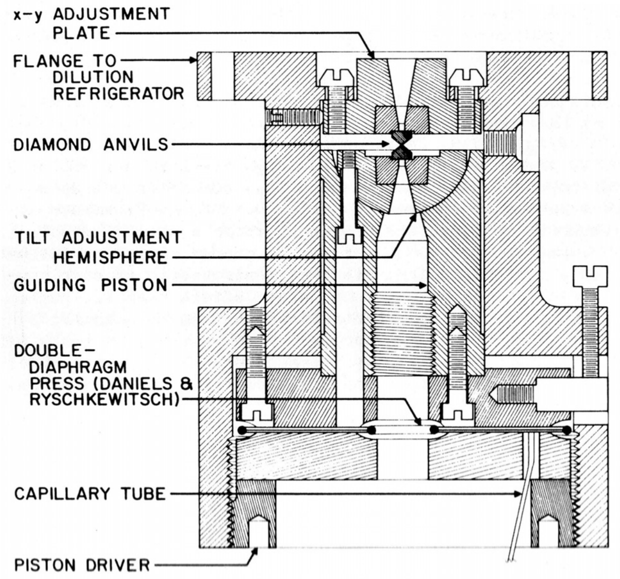

Figure 3.17: A cross-section schematic drawing of the diamond anvil cell designed by J. S. Schilling [131].

and the cell becomes worse. To solve this, the piston is occasionally electroplated with copper and then uniformly polished using diamond paste with particle size less than $\frac{1}{4}$ μm until the piston fits snugly in the cell.

Two diamonds are glued onto a backing material using Stycast 2850 FT Black mixed with catalyst 24 LV in a set of aligning jig. Stycast 2850 FT has a shelf life of 12 months when stored between 18°C and 25°C. When it is stored longer than 12 months, the stycast tends to develop crystallisation. One way to reverse the crystallisation is to warm the stycast at a temperature between 50°C and 60°C until all crystals have dissolved. Normally a piece of zirconium foil with 25 μm thickness is placed between the diamond and the backing material to reduce the local stress on the diamond table under pressure. After the diamonds are mounted in the cell and before the glue is completely dry, they are carefully aligned both laterally and angularly by adjusting the screws on the cell piece and the rocker on the piston piece. The cell is then baked at 74°C in a oven until the glue is completely dry (normally 12 hours). A stainless steel double-diaphragm membrane is used to apply pressure to the diamonds. By applying He gas pressure to the membrane, large forces can be applied to the sample contained in hole of a metal gasket placed between two diamonds. The gas driven membrane has the advantage that pressure can be changed at any temperature above the melting temperature of the loading gas, in contrast to mechanical loading DACs which require the cell to be warmed up to room temperature in order to change the pressure. In order to be able to accurately measure the pressure in the membrane when the He gas pressure is applied from a high-purity He gas bottle, a digital pressure transducer from Omega has been inserted in the pressure system. The transducer uses a 9-30 Vdc excitation voltage. High pressure can be measured accurately in the digital transducer up to 3000 psi or 207 bar. The pressure is determined from the output voltage V. The voltage reads 1.002 V at ambient pressure and increases linearly with pressure to 11 V at 3000 psi. Any intermediate pressure can be extrapolated from

$$P(bar) = 1 + \frac{(3000 - 14.5) \cdot (V - 1.002)}{14.5 \cdot (11 - 1.002)}. \tag{3.11}$$

To carry out high pressure x-ray diffraction experiment at APS, two Mao-type symmetric cells were purchased from the Princeton shop (Figure 3.18(a)). This type of cell is routinely used at APS and is made of stainless steel. Its wide opening and symmetric design is suitable for x-ray studies and laser heating experiments. Pressure

(a) (b) (c)

Figure 3.18: Diamond anvil cells used in synchrotron experiments at APS. (a) symmetric cell, (b) Cu:Be membrane cell from easyLab and (c) piston-cylinder miniDAC in comparison with the size of a nickle.

is applied using two right-handed and two left-handed screws with thin stainless steel washers. When pressure is applied, one right-handed and one left-handed screw are tightened at the same time and by the same angle to ensure that each screw is tightened by the same amount. The thin washer plates have a slight curvature. The washers are stacked in opposing directions when placed on a screw. In a group of 8 washers, 4 washers will be stacked in one direction and the next another 4 will be stacked so that their curvature is in the opposite direction. In Mbar pressure experiment, 3 groups of 8 washers are usually used on each screw.

In the symmetric cell, there is no rocker to adjust the parallel alignment of the culets as in Schilling's cell mentioned above. Therefore, the top and bottom surfaces of the diamond backing plate have to be perfectly parallel in order to achieve high pressure. The diamonds can be aligned laterally by adjusting the 4 set screws that hold the tungsten carbide (WC) plate in place. The WC plate is designed to have a small angle ($\sim 6°$, as shown in figure 3.18(a)) on the outer diameter so that the plate stays on the bottom of the cell when the set screw is tightened.

For x-ray absorption experiments, a membrane type Cu:Be cell from easyLab (Figure 3.18(b)) was also used. This cell can also be used in XMCD experiments where a magnetic field 0.6 T is applied at beamline 4ID-D, APS. When a higher field is required, a superconducting magnet can be used. However, the bore in the magnet is often very small ($<$ 1 inch). In this case, a diamond anvil cell with a small outer diameter is needed. In the high pressure XMCD experiment in Eu where a 4 T magnetic field was applied, a piston-cylinder miniDAC from D'ANVILS (Figure 3.18(c)) made of the nonmagnetic material Inconel 718 was used. This miniature piston-cylinder cell has a diameter of 16 mm and length $\sim$ 19 mm (it varies with anvil height).

3.2.2 Backing Material

The backing materials used in Schilling's DAC are tungsten-carbide (WC) or a Ni-Cr-Al precipitation alloy. The previous design for the backing plate includes only a 1 mm wide bore through the backing plate, suitable for accessing the sample space for determining pressure by measuring the ruby fluorescence or from Raman measurements on the diamond vibron. Optical measurements can be improved by using a bigger aperture on the backing material. If a 15° half angle is added to the bore, a ten fold increase in the intensity can be gained. Since coils used in the ac susceptibility measurements sit right on top of the backing material, it has to have a low magnetic impurity content. Recently a new batch of WC backing pieces (ROCTEC 500) with a 30 degree cone and 1 mm opening on the top surface were ordered from Kennametal

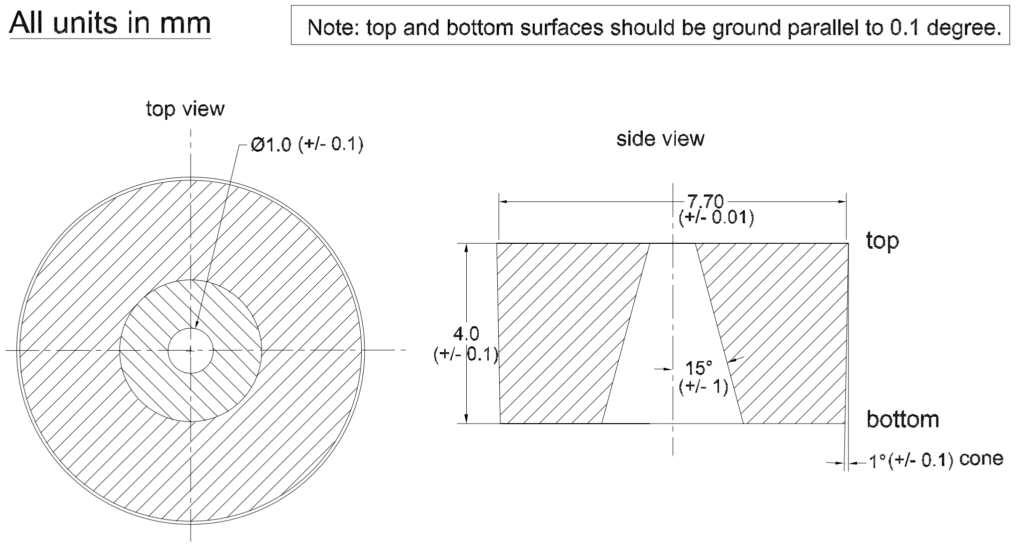

Figure 3.19: Sketch of the WC backing with 15° half angle.

(see Figure 3.19). However, this WC material is more brittle than the ones previously used, possibly due to the large aperture. So care should be taken when pushing the backing plate out of the holder.

The magnetic properties of this backing material were measured in the PPMS. The measurements show that there is a small amount of ferromagnetic impurity in this material at room temperature (see in Figure 3.20), but the temperature dependence is small. PPMS measurements on a different material from Kennametal (PBT 800) show a similar temperature and field dependence to the sample from ROCTEC 500 and ac susceptibility measurement in DAC coil gives a signal change (real part of the susceptibility) of $\sim 3\ \mu V$ from room temperature to 4 K, which is much smaller than the background change ($\sim 16\ \mu V$) in the coil with the previously used WC backing

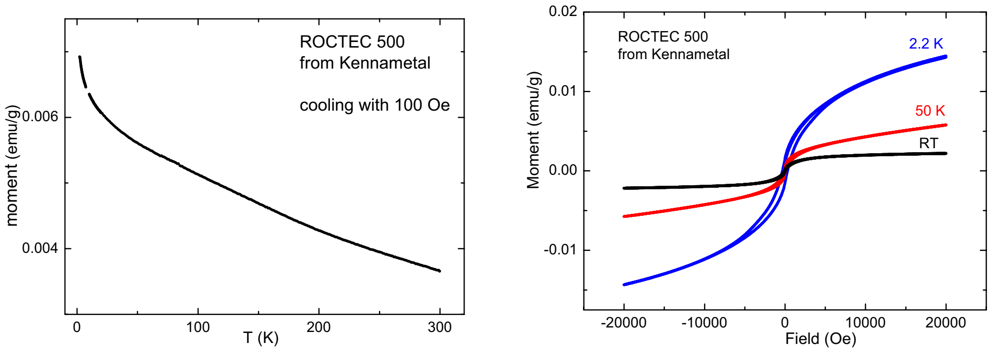

Figure 3.20: PPMS measurement of a cylinder sample (ROCTEC 500). The mass of the sample is 0.3 g. Figure on the left shows the cooling measurement with a filed 100 Oe applied. Figure on the right shows the measurement when the magnetic field is ramping up and down from -2 T to 2 T at room temperature, 2.2 K and 50 K.

plates. Since ROCTEC 500 shows similar magnetic response to temperature and field to PBT 800 in PPMS measurements, the signal change from room temperature to 4 K in DAC coil should be comparable as well. The new backing plates have been used in several optical and electrical resistivity experiments up to 60 bar in membrane pressure and have worked well so far.

In high pressure x-ray diffraction experiments, the backing plate has to have a big enough aperture to allow a diffraction pattern which includes enough diffraction peaks to identify the unknown structure to be obtained. One way to ensure this is to use cubic boron nitride (c-BN) material as backing due to its low absorption to x-rays. If an opaque backing material like WC is used, an aperture angle has to be big enough to give high enough diffraction angle. As seen in Figure 3.21, the maximum diffraction angle 2θ is limited by the angle α and the aperture angle β in the backing plate. One possible solution to achieve this while still having enough supporting material for the diamond is to use a WC backing plate with a normal aperture like a 1 mm cone on the side of the incoming x-rays, and to use a backing plate with a slit-shaped aperture on the side where x-rays exit from the sample. For example, for a 2 mm high diamond height, a slit of 0.8 mm×2.4 mm will give a maximum 2θ angle $\sim 31°$, which is large enough for synchrotron diffraction experiments with a wavelength ~ 0.4 Å. A new anvil design by R. Boehler [133] with a conical anvil sitting directly into the backing plate greatly increases the x-ray aperture, typically to 70° - 75° and is ideal for x-ray work.

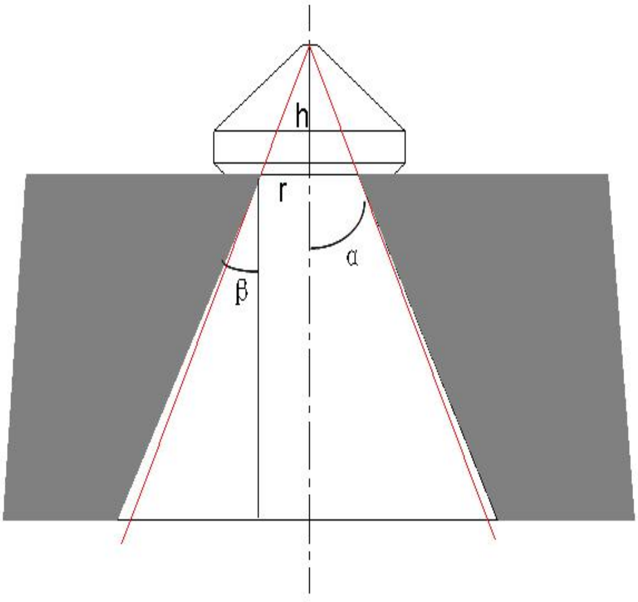

Figure 3.21: Diamond backing sketch shows the relation of the aperture angle and the allowed maximum 2θ angle obtained in x-ray diffraction experiment. h is the diamond height which is normally 2 mm or less. r is the radius of the opening on the top surface. $\alpha = \arctan(h/r)$, and $\beta \geq \alpha$ is preferred.

3.2.3 Gasket

A critical component to achieving high pressures in diamond anvil cells is the gasket. The gasket reduces the strain at the diamond culets and contains the sample and the

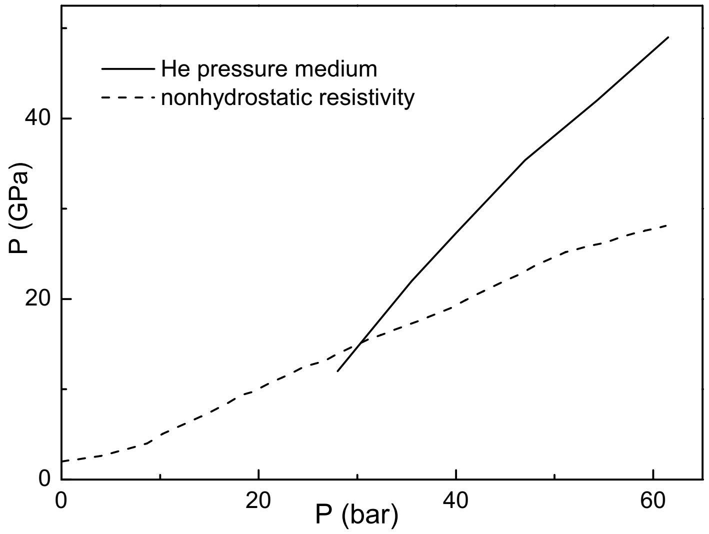

Figure 3.22: Sample pressure versus membrane pressure using Re gasket and anvils of 0.5 mm culet in hydrostatic ac susceptibility experiment and nonhydrostatic electrical resistivity experiment with c-BN and epoxy as the insulation layer.

pressure medium under high pressure. The gasket material has to have both high hardness and good ductility. For magnetic susceptibility measurements, the gasket has to be nonmagnetic and non-superconducting in the measured temperature region. In most of the experiments during this thesis research Re gaskets with a initial thickness $\sim$ 250 μm were used. Re has been extensively used as gasket material. It has a low magnetic response and a hardness of 51 HRC. Typical sample pressure dependences on membrane pressure in a hydrostatic experiment with He as pressure medium and nonhydrostatic electrical resistivity experiment in 0.5 mm anvils are plotted in Figure 3.22.

Re superconducts at 1.4 K [132] at ambient pressure, but T_c goes up to $\sim$ 4 K under strain, which limits the lowest temperature in ac susceptibility measurements to

4 K. In order to be able to carry out measurements to the lowest temperature (∼1.3 K) achieved in the continuous flow cryostat used in DAC system, we also use Cu:Be gaskets (initial thickness $\sim 300\ \mu m$). However, it has a hardness of 25 HRC and has to be annealed before use. After being annealed at 315 °C for 3 hours, Cu:Be can have a hardness of 41 HRC. It is hard and ductile enough for Mbar pressure experiments and has a very low magnetic response at all temperatures. The highest pressure attained with this gasket material was of 143 GPa by M. Debessai in experiments on Eu's superconductivity [7]. Since the hardness of Cu:Be gasket after annealing (41 HRC) is lower than Re (51 HRC), it becomes much thinner than Re under pressure. At 1 Mbar, the thickness of Re becomes $\sim 15\ \mu m$ while the thickness of Cu:Be is only $\sim 5\ \mu m$. In hydrostatic experiments with He as pressure medium, it is critical that the diamonds do not touch the sample directly under pressure, which requires that the gasket can not be thinner than the sample. In this case, Re is preferred as gasket material.

Before the experiment, a gasket is normally preindented to a thickness of approximately $\frac{1}{9}$ of the culet diameter or $\frac{1}{3}$ of the hole diameter to prevent the gasket from large deformation and to ensure stability of the hole. A hole of $\frac{1}{3}$ the diameter of the culet is then drilled with an electrical discharge machine (EDM). Laser drilling of the hole at GeoSoilEnviroCARS (GSECARS), APS was also used in one of the XMCD experiments. When liquid He is used as pressure medium, the gasket hole should be $\frac{1}{2}$ of the culet size due to the high compressibility of He. The gasket has to be carefully selected to make sure no crack or scratch on the preindented area. It is then gold plated on both sides to improve the sealing. For hydrostatic measurements, when pressure is applied initially, the diamond anvil cell is cooled below 2 K so that He is in the superfluid state and can flow into the sample space without any bubble. Then membrane pressure is applied to trap the superfluid He inside the sample space. Therefore, any crack or scratch in the gasket could lead to failure of the experiment.

In some synchrotron experiments which require a low x-ray energy, a fluorescence geometry or radial diffraction has to be used where x-ray goes through gasket material rather than through the diamonds in transmission geometry. In this case, typical high strength gasket like Re cannot be used due to the strong absorption. A gasket material with relatively low absorption to x-ray such as Be [134, 135] or mixture of amorphous boron and epoxy [136] could be used. However, Be is extremely toxic and pulverizes when it fails. Therefore, the application is restricted due to safety issues. The high shear strength, low x-ray absorption and low thermal conductivity also make amorphous boron a good gasket filling material with boron-epoxy replacing the center part of the normal gasket material and giving a clean diffraction pattern in x-ray diffraction experiment and a good thermal insulation in laser heating experiment [137, 138].

3.3 Pressure Measurement in the Diamond Anvil Cell

In high pressure experiments, several different methods of pressure determination can be used in a DAC by monitoring pressure-induced physical property change of a known sample. In x-ray diffraction experiments, pressure can be determined from the EOS of a well-calibrated sample. In transport measurements, the pressure can be determined by the shift of superconducting transition temperature. This section presents a description of pressure measurements using ruby fluorescence below 100 GPa and using the Raman shift of the diamond vibron above 100 GPa.

3.3.1 Ruby Manometer

In high pressure experiments, ruby (Al_2O_3 doped with Cr^{3+}) is widely used as a manometer. The sharp and high intensity peaks of the ruby fluorescence spectrum display a red shift under pressure, which makes it possible to be used as a manometer in a diamond anvil cell when a small piece is loaded on top of the sample.

The fluorescence mechanism is due to optical "pumping" from the ground state to the excited band U (centered at 24800 cm^{-1}) or Y (centered at 18200 cm^{-1}) by a green or a blue laser (see Figure 3.23). The excited state then decays quickly to the metastable state ^2E and $^2T_1$ by nonradiative decay (phonon-assisted relaxation) followed by a radiative transition to the ground state by emitting a photon which gives R_1 and R_2 lines. At ambient condition, they are observed at 694.3 and 692.9 nm, respectively. Under pressure, both ^2E and $^2T_1$ levels shift to lower energy and thus R_1 and R_2 lines experience red shift under pressure [139]. The populations of ^2E and $^2T_1$ follow the

Boltzmann distribution. Therefore, at room temperature, ^{2}E and ^{2}T$_1$ populations are roughly the same and thus the R$_1$ line intensity is comparable to that of the R$_2$ line. At low temperature, however, the (lower energy) ^{2}T$_1$ population decreases and the R$_2$ line is suppressed, resulting a higher intensity of R$_1$ at low temperature. For this reason, the shift of R$_1$ line is used in experiments to determine pressure. The temperature dependence of R$_1$ line is given by [140]

$$\nu_0(t) = 14422.0 - 36.612t^{3/2} + 169.77t^2 - 264.54t^{5/4} + 112.54t^3, \tag{3.12}$$

where $\nu_0(t)$ is given in cm^{-1} and $t = \frac{T}{300(K)}$. The temperature dependence of R$_1$ wavelength is plotted in Figure 3.24.

The ruby fluorescence shift under pressure has been calibrated by different groups [141–145]. The calibration used in this thesis is given in Reference [145] as

$$P(GPa) = \frac{1876}{10.71}\left[\left(\frac{\lambda}{\lambda_0}\right)^{10.71} - 1\right], \tag{3.13}$$

where λ_0 is the wavelength of the R$_1$ line at ambient pressure. Ruby fluorescence lines are very sensitive to the hydrostaticity of the pressure condition. The lines are broadened and the separation of R$_1$ and R$_2$ lines increases under nonhydrostatic pressure due to an increase in the pressure gradient. Under pressure the U and Y bands shift to higher energy. Therefore, above 70 GPa the energy of Ar ion laser with wavelength 514 nm becomes insufficient to pump the ruby fluorescence and the R$_1$ intensity becomes too low to measure. A laser with higher energy such as a blue He-Cd laser with wave-

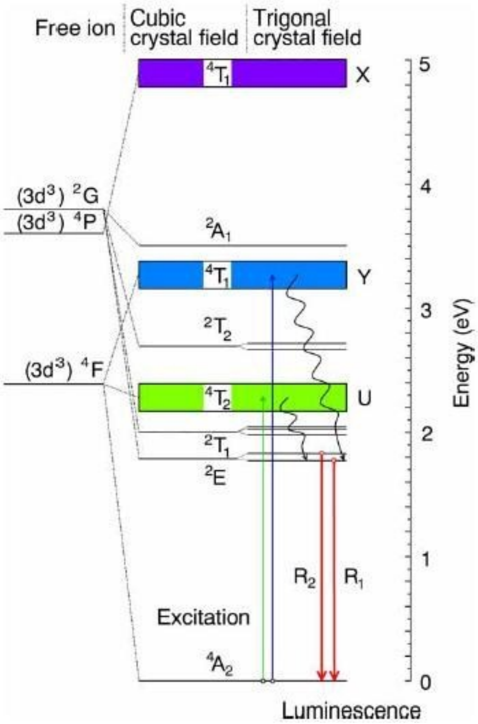

Figure 3.23: Excited states of Cr^{3+} in ruby. Figure taken from Reference [139].

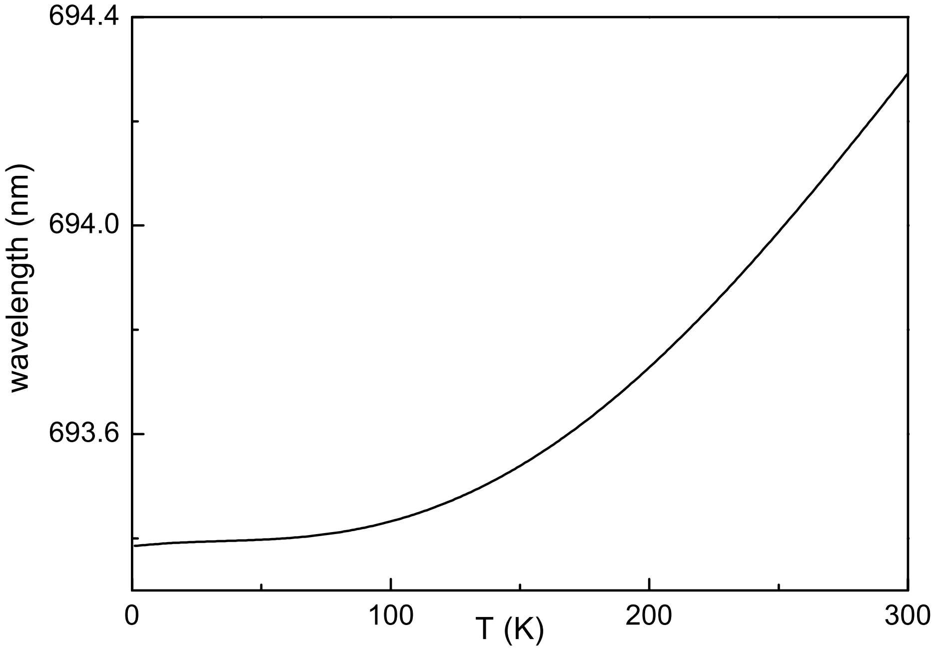

Figure 3.24: Temperature dependence of R_1 fluorescence line at ambient pressure given by Reference [140].

length 441.6 nm is needed to populate the absorption band. However, above 1 Mbar, the energy of He-Cd laser becomes too low to measure the ruby R_1 line. In addition, above 1 Mbar the increasing background from the diamond fluorescence makes the extraction of the weak R_1 line extremely difficult. Above 1 Mbar the diamond vibron can be used to determine the pressure which will be described in Section 3.3.2. For the optical system setup to measure the ruby fluorescence inside and outside the cryostat please refer to J. Hamlin's thesis [150].

3.3.2 Diamond Raman Gauge

When light is scattered by a material, most of the photons are elastically scattered (Rayleigh scattering), i.e. the scattered photons have the same energy with the incident light. About 1 in every 10 million photons, however, is scattered inelastically (Raman scattering). The incident photons exchange energy with the atoms through vibrational energy levels and are scattered by an excitation, emitting (Stokes scattering) or absorbing (anti-Stokes scattering) of phonon.

Hanfland and Syassen first proposed using the Raman high frequency edge from the diamond anvil as an in-situ pressure gauge [147]. The Raman spectrum of diamond consists of a single peak located at 1333 cm^{-1} at ambient pressure and shifts monotonically to higher frequency under pressure. Since the pressure on a diamond anvil varies from ambient pressure on the anvil table to the maximum pressure at the center of a anvil tip, the high frequency edge corresponds to the highest pressure region at the center of the culet where the sample is loaded.

The diamond Raman high frequency edge was calibrated by Akahama *et al.* [146] up to 310 GPa against the sample pressure determined from the equation of state of Pt. It was found that this calibration is independent of the geometry of the anvil, gasket and pressure medium. A universal relationship between the edge frequency and the pressure is given by

$$P(GPa) \simeq K_0 \frac{\Delta\nu}{\nu_0}\left[1 + \frac{1}{2}\left(K_0^{'} - 1\right)\frac{\Delta\nu}{\nu_0}\right] \tag{3.14}$$

where $\nu_0 = 1333 \pm 1$ cm^{-1}, $K_0 = 547(11)$ GPa and $K_0^{'} = 3.75$ (20).

One advantage of using diamond as a pressure gauge is that no pressure marker is needed inside the pressure cell. By measuring the Raman edge shift at the center of the culet, accurate pressure can be determined in nonhydrostatic experiments. If ruby is used as a pressure calibrant, it has to be placed right at the center of the sample in order to measure the pressure accurately.

The optical system for measuring the diamond vibron outside of the cryostat was developed and modified by M. Debessai based on the ruby system using the Nikon Optiphot microscope. Although higher energy lasers give higher Raman scattering intensities, it has been reported that laser illumination, especially shorter wavelength (blue light), can induce a catastrophic growth of defects in the high pressure region and cause diamond failure [148]. For this reason, in our experiment, the 514 nm line from Ar ion laser is used. Since Raman scattering is only a small fraction of the Rayleigh (elastic) scattering, a high pass 515 nm edge filter is used to filter out the intensely scattered laser light. More detailed discussion on the optical setup can be found in Reference [149].

3.4 Ac Susceptibility Measurements

The coil system used in ac susceptibility measurements was designed by V. G. Tissen and wound in the lab with 60 μm Cu wire. It consists of two identical coils, a coil to measure the signal change induced by the sample's magnetic property changes and another coil acting as compensation coil to cancel out the large background signal. A picture of the coils is shown in Figure 3.25.

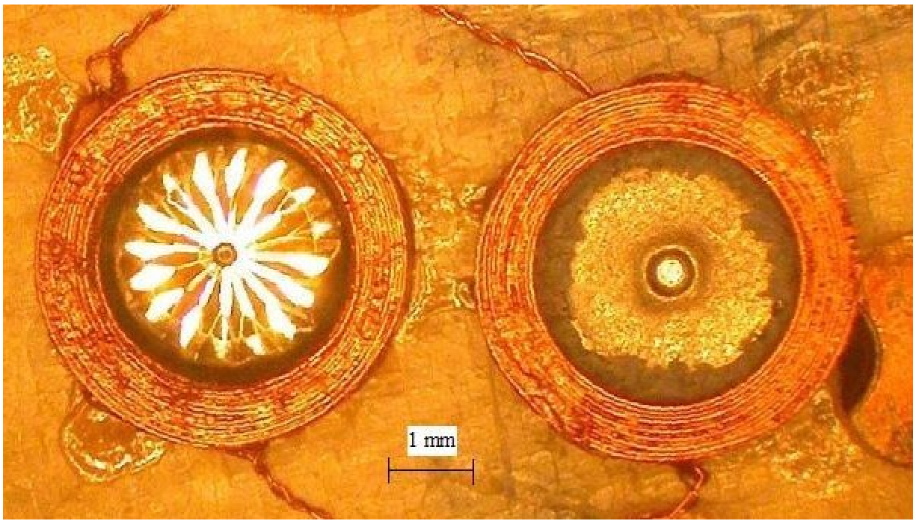

Figure 3.25: Coil system used in ac susceptibility measurements. The coil on the left surrounds the diamond anvils, the gasket, and the sample. The coil on the right is the compensation coil with a dummy gasket placed at the center of the coil. The coil has an inner diameter of 3.5 mm and a height of 1.95 mm.

In each coil, 6 layers of primary coil are wound around 6 layers of secondary coil. Each layer consists of 30 turns. Diluted GE varnish is applied on top of each layer to hold the coil together. The two primary coils are connected in series in the same direction to generate the same field at the center of the coil, while two secondary coils are connected in series in opposite directions so that the signal induced in one coil is canceled by that from the other. The connections are made using spark-welding instead of lead soldering to avoid signal contamination from the superconducting transition in lead around 7 K. To cancel out the signal from the gasket in the pick-up coil, a dummy gasket of the same material and dimensions is placed in the compensation coil as seen in Figure 3.25.

An alternating magnetic field is generated by the primary coil and induces an ac voltage in the secondary coil. When a superconductor is placed in the coil, the magnetic flux penetrates the sample above T_c. When it is cooled below T_c, the flux is expelled out of the sample due to the superconducting shielding effect. Similarly, in the case of a magnetic sample, when it is cooled below the ordering temperature, the secondary coil picks up the signal change induced by magnetic flux change from the sample. However, the transition from a magnetic sample is very often smaller and broader than a superconducting transition. It is very challenging to measure the ordering temperature to high pressures with this coil system.

A setup of the ac susceptibility measurements is shown in Figure 3.26. An ac current of 6.8 mA is applied to the primary coil to generate a magnetic field of 3 Oe at the center of the coil. Since the resistance of the coils decreases significantly with temperature, a 700 Ω external resistor is used to ensure that the change in the current through the primary coil, and therefore strength of the magnetic field, is negligible upon cooling. The signal from the secondary coil is amplified by a factor of 100 times using a pre-amplifier (SR554) outside of the cryostat. A lock-in amplifier (SR830) is then used to enhance the signal-to-noise ratio. The temperature of the sample is measured

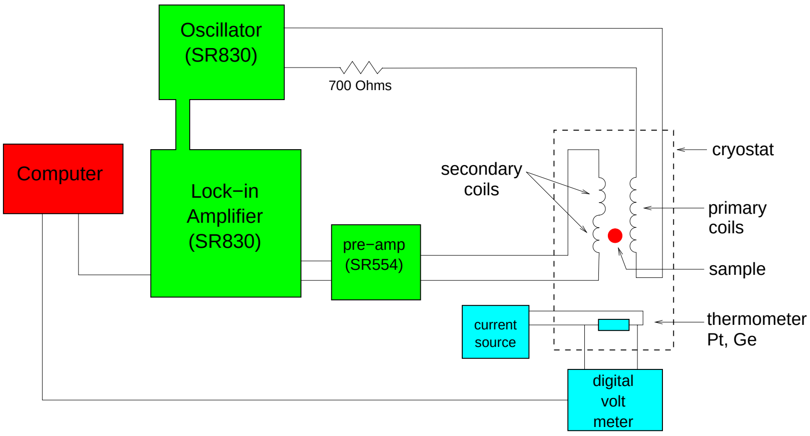

Figure 3.26: Schematic of ac magnetic susceptibility circuit in DAC system. Taken from [150].

using two calibrated resistors Pt and Ge. As a metal, the resistance of Pt decreases upon cooling and thus becomes less sensitive at low temperatures. Ge, on the other hand, is a semiconductor, so the resistance increases during cooling, making it more sensitive at low temperatures. Typically, Pt is used down to 50 K and Ge below 50 K. The digitized signals from the lock-in amplifier and the temperatures/resistance of the thermometers are recorded by a LabVIEW program on the computer.

The induced voltage in the secondary coil in MKS units is given by

$$S = \frac{\pi f \alpha H V N}{R(1-D)} \chi. \tag{3.15}$$

f : frequency of the applied field (Hz)

$\alpha \equiv 1/\sqrt{1+(L/R)^2}$, $2L$: length of the coil (m)

H : magnetic field (T)

V : volume of the sample (m^3)

N : number of turns in the pick-up coil

R : radius of the pick-up coil (m)

D : demagnetization factor.

$\chi = -1$ for a superconductor

A frequency of 1.023 kHz is used to optimize the signal-noise ratio. The demagnetization factor D depends on the geometry of the sample. For a sample of 80 μm in diameter and 20 μm thick, $D \sim 0.6$ [151], giving a superconducting signal of 20 nV.

During L. Sun's visit in our group, a modified version of the coil system was made and tested. The diamond anvils in her cell are larger (girdle size 3.4 mm diameter and height 2.4 mm) than the ones we normally use (girdle size 3 mm diameter and height ~2 mm). Therefore, the coils were modified to have a 3.8 mm inner diameter and height of 2.6 mm to accommodate the bigger anvils. Similar to our coil system, 6 layers of secondary and 6 layers of primary coils were wounded with 40 turns per layer. The coil system was loaded in her Cu:Be cell and tested at low temperature. To test the sensitivity of the coil, a piece of MgB_2 sample ~ 95 μm diameter was loaded in a 130 μm diameter hole drilled in a Re gasket. The measured superconducting transition of MgB_2 with this coil system is about 40 nV, comparable to the transition size measured with our coils.

However, using the modified coil in Sun's Cu:Be cell the temperature dependence of the background is more than 10 fold higher than what we normally measure with the original coil system inside our Cu:Be cell (Figure 3.27). One possible reason for this high background change upon cooling is that Sun's cell is made from BeCu-25 alloy which contains of 0.25% of magnetic impurity of Ni, Co and Fe, while in our cell the parts near the sample and coil are made of nonmagnetic Cu:Be. The magnetic impurity in the cell can greatly increase the signal change upon cooling and the noise level can make it difficult to resolve a transition of only a few nV.

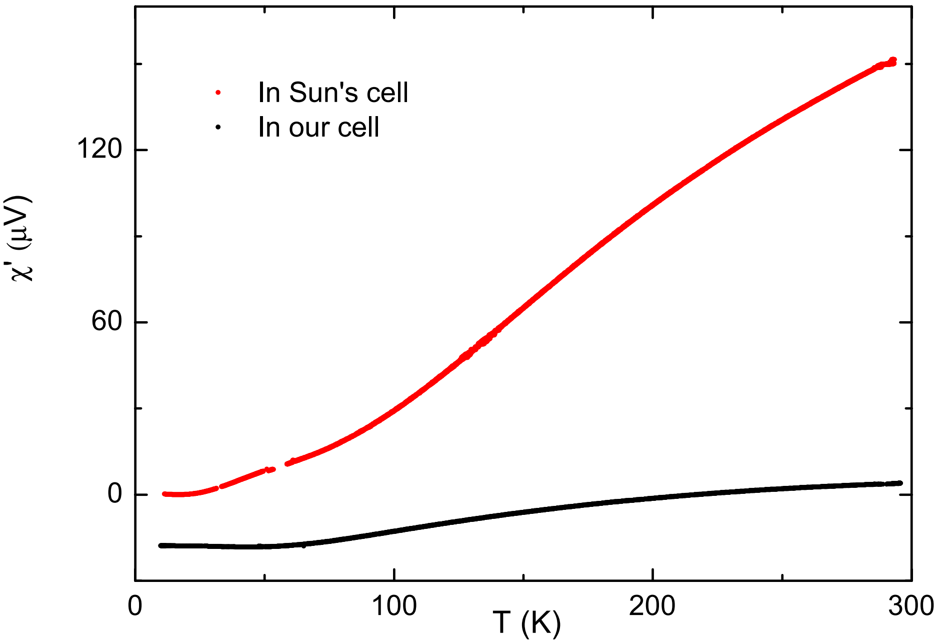

Figure 3.27: Comparison of the background change upon cooling with the modified coils in Sun's Be:Cu cell and our coils in the Be:Cu cell of Schilling's design.

3.5 Resistivity Measurements in the Diamond Anvil Cell

The resistivity measurement technique in a diamond anvil cell was introduced to our group by T. Matsuoka from Osaka University, Japan. In the setup, a metal gasket is first preindented and drilled. The preindented area is then filled with c-BN, diamond, or Al_2O_3 fine powder mixed with epoxy mixture. The powder is then pressed to a few GPa by the diamonds. Electrodes with sharp tips cut from a 5 μm Pt foil are placed on the preindented area in the gasket (see Figure 3.28). Contact is achieved by pressing the sample directly onto the electrodes with the diamond anvils. Further details of the resistivity technique are outlined in the DAC manual.

Although solid pressure media like NaCl can be used in the resistivity experiment, this technique is inherently nonhydrostatic. It is challenging to achieve four-point resistivity measurements under pressure. Very often one or more electrodes will fail under pressure, or short to the metal gasket. When this happens, a pseudo-four-point configuration can be used with one electrode serving as both a current and voltage lead. However, in studies searching for insulator-metal transition, four-point configuration has to be achieved, because contact resistance in a pseudo-four-point configuration becomes significant when the sample turns to metal under pressure.

In Schilling's cell, due to the cell geometry, the Pt electrodes are prepared on the gasket sitting on the diamond anvil located on the piston side. In order to be able to check the contacts between the Pt electrodes and the metallic gasket, a fifth Pt electrode is connected to the gasket with silver paste. Then the five wires from the sample and the gasket are extended outside the cell by five Cu wires with a 140 μm

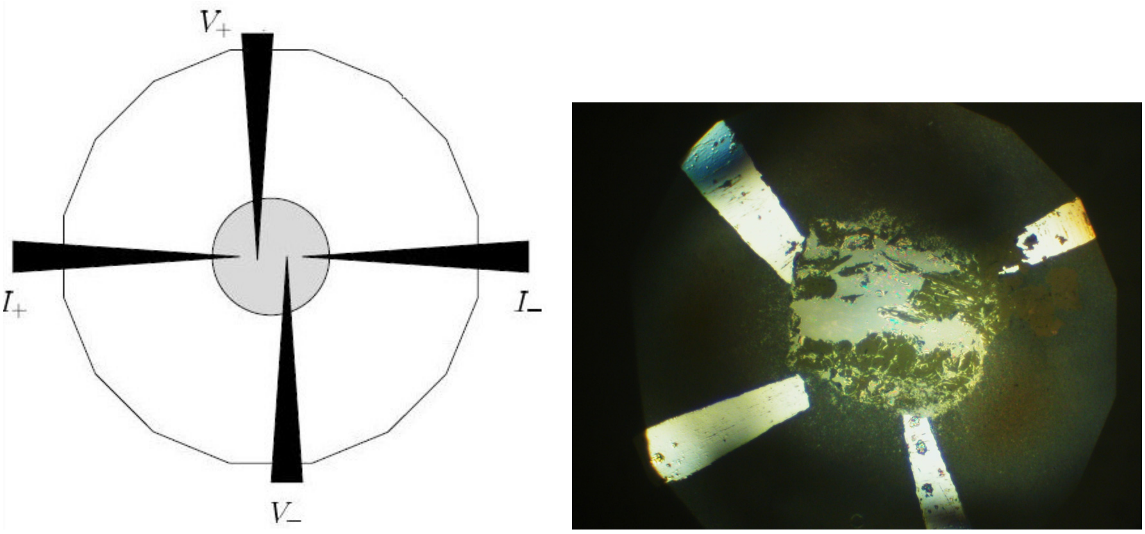

Figure 3.28: Schematic of four-point resistivity measurements (left) and picture of EuO sample pressed against the four Pt electrodes at 2 GPa (right).

diameter. When the wires are taken outside of the cell through the two side holes, care should be taken to make sure the insulation on the Cu wire are not stripped by the sharp edge on the holes. During the sample loading, it is critically not to touch the electrodes. The sample has to be loaded first and then ruby is loaded at the center of the sample, which is very challenging, especially for air sensitive samples the sample loading has to be done inside the glove box. In this case, it is easier to load the sample in the sample chamber and place ruby on the upper diamond.

DC-like resistivity measurements can be done with the lock-in amplifier SR830 with a sinusoidal current sent to the sample at an optimized frequency of 13 Hz. This frequency has been tested out by M. Debessai and is high enough to get a smooth sinusoidal wave from the oscillator and low enough to avoid parasitic voltages due to the inductive coupling between the wiring. However, DC resistivity measurements are preferred and should be done whenever it is possible.

3.6 Photolithography in the Diamond Anvil Cell

Ac susceptibility and resistivity measurements are two widely used techniques to investigate magnetic state changes of a matter under pressure using diamond anvil cell. Resistivity measurements are superior to ac susceptibility measurements when a structural phase or magnetic transition occurs since the signal change in resistivity is much larger than in ac susceptibility. In experiments over 1 Mbar, anvils with culets 100 μm or smaller are normally used. The sample size is thus limited to 50 μm or less. In ac susceptibility measurements, the transition size then becomes too small to be resolved by the coil system. In electrical resistivity measurements, the extremely small sample makes it very challenging to manually set up the four electrodes.

To overcome these difficulties, electrodes and miniature coils can be deposited onto diamond anvils by lithography [22, 152]. Photolithography can fabricate features as small as 1 μm while electron-beam lithography has a resolution of 20 nm. The micron size electrodes for four-point resistivity measurement are deposited on the culet and are more robust under extreme pressure than four electrodes physically contacting the sample in the regular resistivity technique. For ac susceptibility, a miniature coil much closer to the sample gives more sensitivity to detect the signal change accompanied by structural and magnetic transition.

A photomask with patterns of electrodes and coils for resistivity, Hall effect, and ac susceptibility measurements has been designed in AutoCAD and fabricated at Photo Sciences. The smallest feature size of the patterns is of 3 $\pm$ 0.5 μm. The photomask ($4'' \times 4''$) is patterned with Cr on soda-lime glass. Resistivity patterns are designed

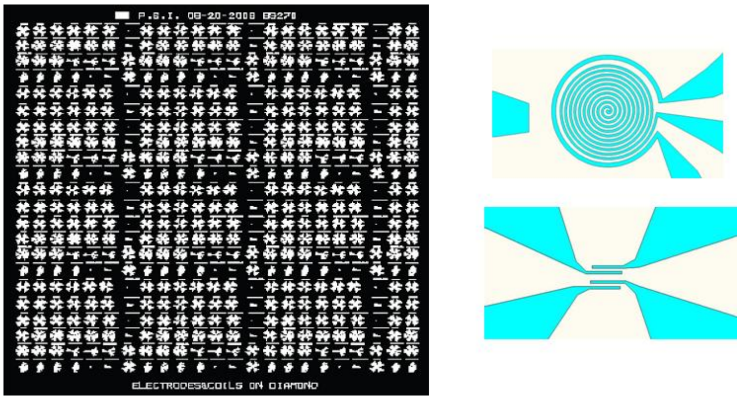

Figure 3.29: Positive photolithography mask of chrome on soda-lime glass with the electrical resistivity and ac susceptibility patterns (left), the first layer pattern of a 10 turns secondary coil and 1 turn primary coil (right top) and a pattern for electrical resistivity measurements.

for anvil culet sizes ranging from 20 to 900 μm and miniature coil patterns from 100 to 500 μm culet size. A picture of the photomask, a coil and resistivity patterns are shown in Figure 3.29.

The fabrication process is being carried out in Prof. Joshua Maurer's lab in the chemistry department on campus. Figure 3.30 shows the fabrication procedure. Firstly, the positive photoresist is deposited uniformly on the clean substrate (diamond culet) mounted on a Brewer Science CE-200 spin coater while it is spinning at a rate $\sim$ 3000 rpm. Then the diamond substrate is soft-baked at 90-100 °C on a hot plate for about 5 minutes to remove the solvent in the photoresist and promote its adhesion to the diamond. The diamond holder is then mounted on a HTG mask aligner with the desired pattern on the photomask centered on top of the diamond culet. The UV is turned on to expose the photoresist for $\sim$ 1 minute through the pattern. The patterned photoresist is then developed for 45 seconds in a developer solution. For a positive photoresist, the UV exposure decomposes the development inhibitor in the photoresist

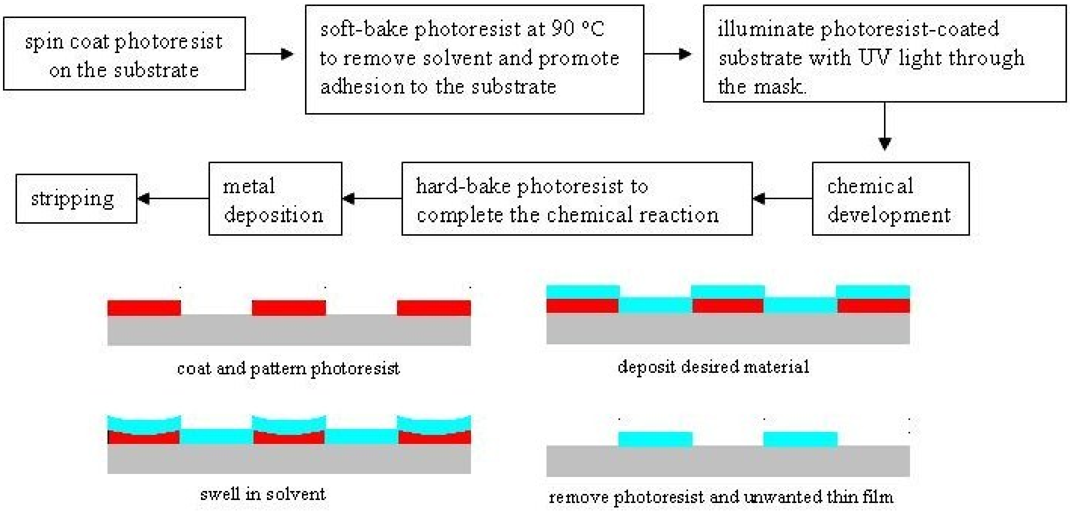

Figure 3.30: Photolithography flow chart and diagram of fabrication process.

and developer solution dissolves only the exposed area. If a sharp pattern is achieved on the photoresist, the diamond is then hard-baked to complete the chemical reaction. The thin film with desired material is then deposited onto the diamond in the PVD-75 electron beam evaporator. Finally, the diamond is immersed in stripping solution such as acetone to remove extra photoresist and therefore the unwanted film, leaving only the desired film deposited on the diamond.

For electrical resistivity electrodes, Au or Cu will be deposited onto the diamond culet due to the high electrical conductivity. However, Au does not stick to diamond very well. Ti can be used as a binder between the diamond and the Au layer. For miniature coil fabrication, a multilayer deposition is necessary. After deposition of the first layer of pattern (top right pattern in Figure 3.29), an electrode has to be deposited at the center of the pattern to extend the lead out of the diamond culet area without shorting to the other part of the coil pattern. Therefore, a layer of insulating material is needed. Then an electrode is deposited to extend the lead at the center out of the diamond culet region. In the chemistry lab, a rather large and flat glass substrate is normally used. Due to the much smaller area on the diamond culet, the standard fabrication process must be modified to make it work in the case of diamond. During the fabrication the diamond is glued onto the cylindrical holder used in Schilling's diamond anvil cell. Chucks for holding the diamond substrate onto the spin coater, mask aligner, and the e-beam evaporator were modified (see Figure 3.32 3.33 3.31 for drawings). Fabrication of the miniature coil is underway. Low temperature tests should be done with the mini-coil and compare with the conventional coil system.

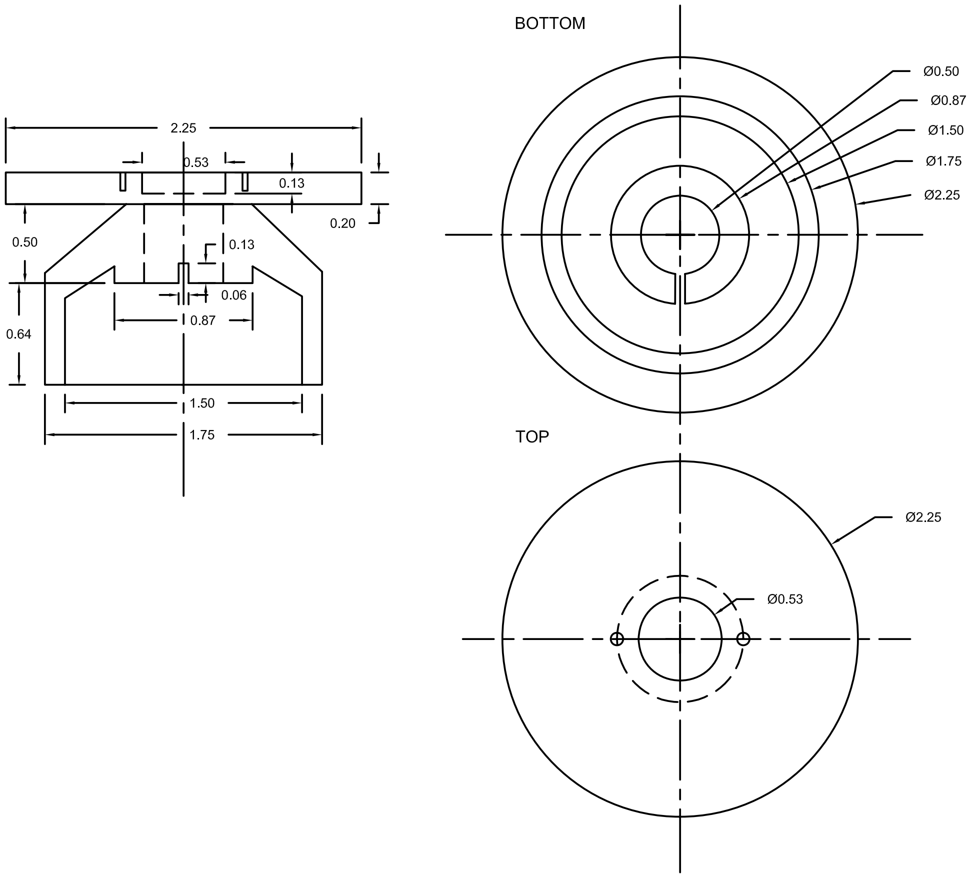

Figure 3.31: Drawing of the revised aluminum chuck for Brewer Science CE-200 spin coater. All units are in inches.

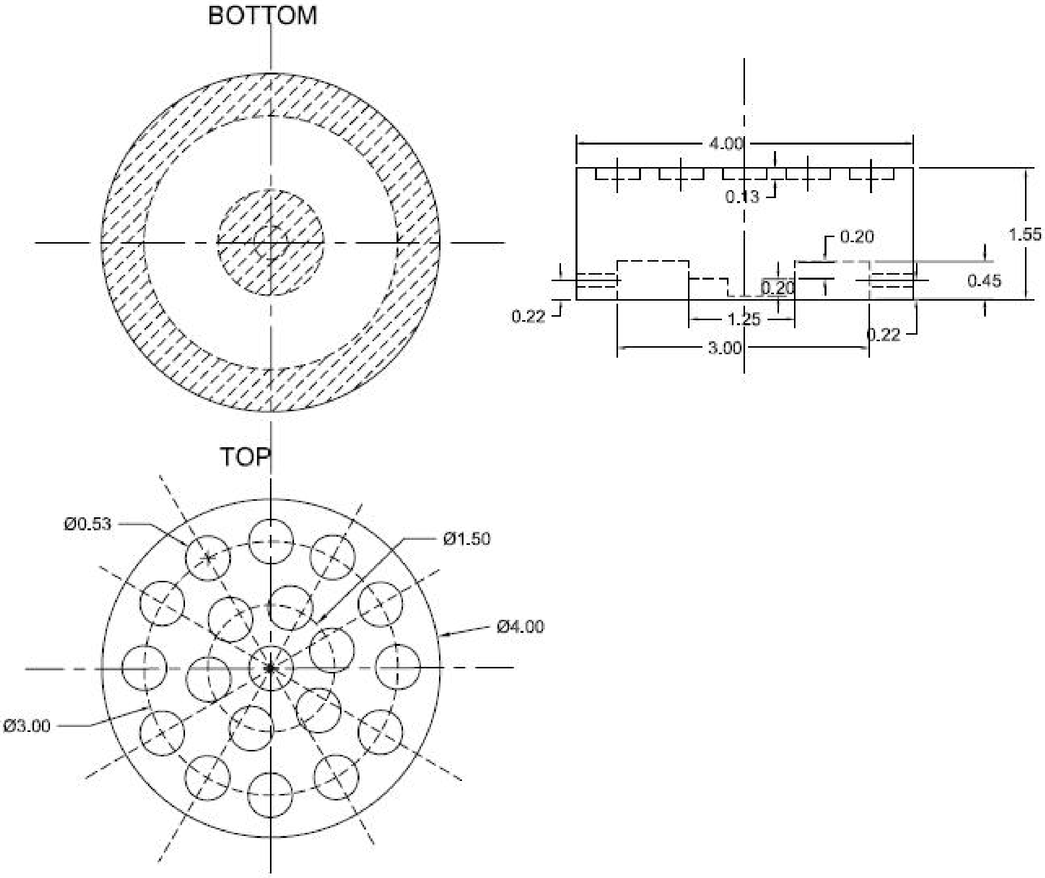

Figure 3.32: Design of HTG mask aligner. All units are in inches.

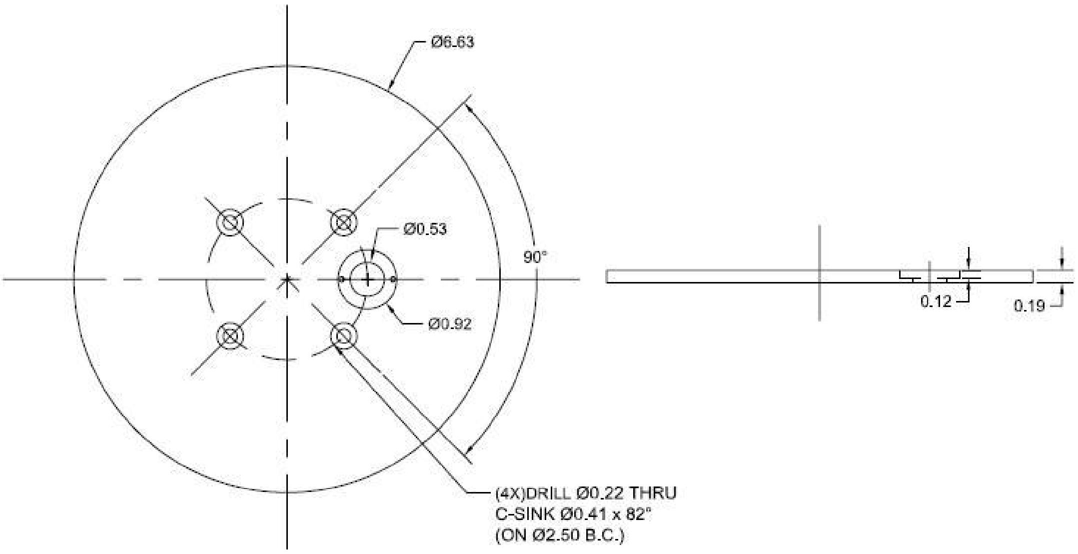

Figure 3.33: Drawing for the substrate holder used on PVD-75 e-beam evaporator. All units are in inches.

3.7 He-Gas Pressure System

The He-gas pressure system uses He as pressure medium and can achieve pressures as high as 1 GPa. The ultra-high purity He gas is first compressed by a two-stage compressor (Newport Scientific) up to 1.7 kbar. The pressurized He gas is then further compressed by an intensifier (Hardwood Engineering). The high pressure gas is transmitted to the pressure cell through a flexible Cu:Be capillary with an outer diameter of 3.0 mm and inner diameter of 0.3 mm. The pressure can be changed at any temperature above the freezing temperature of He. The pressure cell is made of Cu:Be with an inner diameter of 7 mm and length of 38.4 mm. A digital manganin gauge located at room temperature monitors the pressure. An additional room temperature volume reduces the pressure change at low temperature. A sketch of the He-gas pressure system is shown in Figure 3.34. A closed-cycle cryostat is used to cool the high pressure cell down to 10 K. By pumping on the sample space slowly, temperature as low as 5 K can be achieved.

A home-made coil is placed inside the high pressure cell to measure the ac susceptibility of the sample. The coils are wound from 60 μm Cu wire onto a Vespel holder which does not have any magnetic response. The coil system consists of two secondary coils with 6 layers, and each with 60 turns/layer, and one primary coil with 6 layers and 260 turns/layer. The two secondary coils are counter wound and carefully balanced. The 2 mm diameter cavity of the Vespel holder serves as the sample space. The sample is loaded and centered in either one of the secondary coil to maximize the signal in the coil. A schematic drawing of the coil is shown in Figure 3.35. Two pairs of Pt and Ge thermometers are placed at the bottom and the top of the pressure cell to measure the sample temperature and monitor the temperature gradient. During measurements, the temperature gradient is controlled below 50 mK by adjusting heaters placed at the cold head inside the closed cycle cryostat and around the pressure cell.

Helium starts to freeze above 27 bar at around 1 K. Under pressure the melting temperature increases drastically, reaching 44 K at 6 kbar with about an 8% pressure loss. Therefore, cooling or warming through the melting curve must be done slowly to avoid sudden pressure changes in the cell. The coldest part of the closed-cycle cryostat is about 20 cm above the top of pressure cell. Near the melting temperature a good temperature gradient must be maintained so that the capillary is warmer than the top of the cell and top of the cell is warmer than the cell bottom to make sure He solidifies from the bottom to the top to avoid any blockage in the capillary. If He freezes first

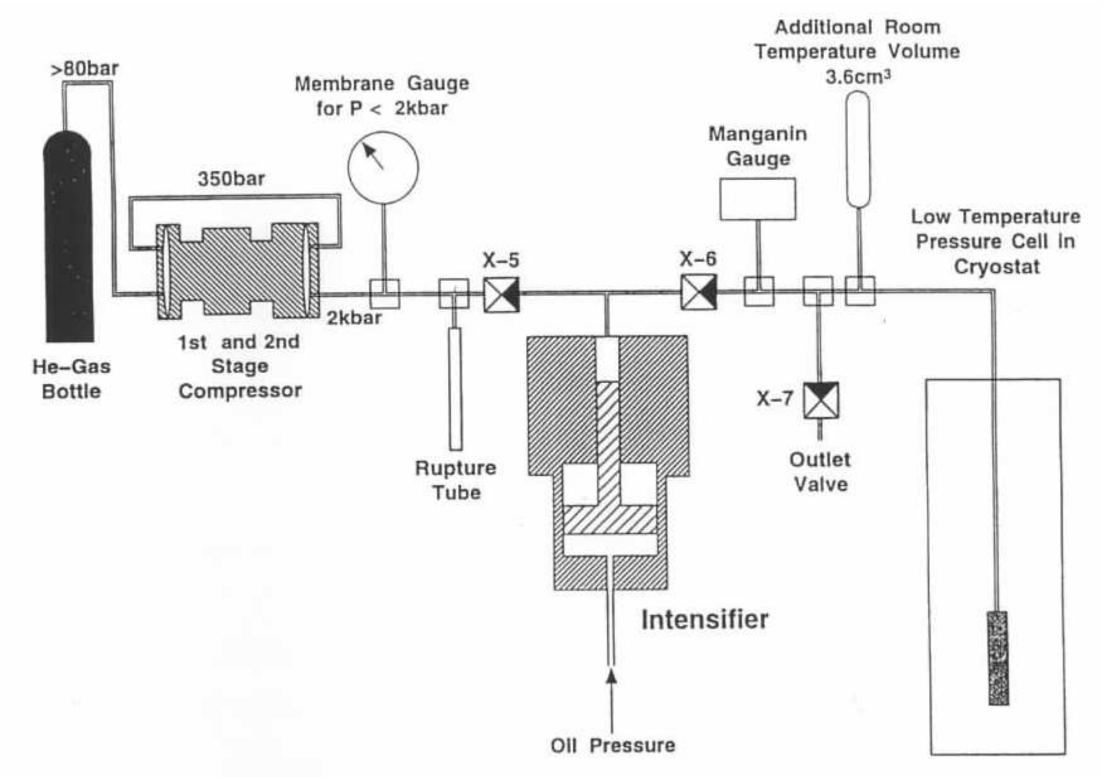

Figure 3.34: A sketch of the He-gas pressure system. X indicates high pressure valves.

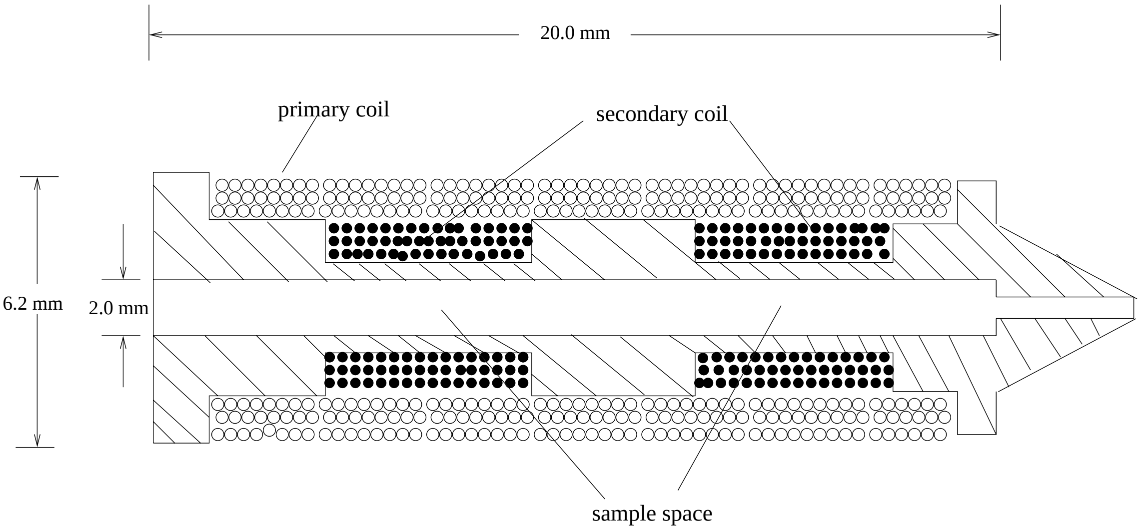

Figure 3.35: A schematic drawing of the coil system for He-gas pressure system [149].

in the capillary, the manganin gauge at room temperature no longer measures the pressure in the sample space. Upon warming, if the pressure cell is warmer than the He blocked capillary, a sudden pressure increase from He melting could destroy the coils. A good temperature gradient can be achieved by applying heaters on the cold head, capillary, and pressure cell. The capillary temperature is typically kept at least 20 K above the melting temperature and the cell top kept at least 1 K warmer than the bottom when passing through melting curve. More detailed discussion about the He gas pressure system can be found in T. Tomita's thesis [153].

Chapter 4

Results and Discussion

4.1 Pressure-Induced Structural Transition in Eu Metal

The results presented in this section were published in Reference [165] and a good portion of this section is taken from this paper.

As discussed in Section 2.2, in contrast to the other lanthanide metals, which are trivalent, Eu and Yb are divalent. As a result, Eu and Yb have much larger atomic volumes than the neighboring metals and do not fit into the general structure sequence across the trivalent lanthanides series under pressure.

A previous XANES study on Yb's valence by Syassen *et al.* [154] using a lab x-ray source reports Yb's valence increases between 4 and 30 GPa and becomes trivalent above 30 GPa. A more recent study by Fuse *et al.* [155] using a synchrotron source shows Yb's valence saturates at 2.65 at 34.6 GPa instead of becoming fully trivalent. At pressures near 1 Mbar, Yb takes on the hexagonal structure exhibited by Sm and

Nd under pressure, providing evidence that above 1 Mbar Yb becomes fully trivalent and joins the regular lanthanides series.

Structure studies on Eu metal at ambient temperatures, on the other hand, have only been carried out to 43 GPa [38, 157], revealing a bcc-to-hcp transition at 12 GPa accompanied by a 4% volume collapse, with a new close-packed structure appearing near 17 GPa. From the fact that the EOS of Eu approaches that of trivalent Gd near 20 GPa, it was concluded that at this pressure a significant increase in Eu's valence must have occurred [38]. L_{III} absorption [48] and Mössbauer effect [49,127] studies reportedly indicate that at 10 GPa Eu's valence has already increased to approximately 2.5, with a further increase to 2.64 at pressures of 34 GPa. Theoretical predictions of the pressure necessary for the full divalent-to-trivalent transition in Eu vary from 35 GPa [39, 40] to 71 GPa [41].

Should sufficiently high pressure be applied to bring Eu to full trivalency Eu^{3+} ($4f^6$ where J = 0), its divalent magnetic ground state Eu^{2+}($4f^7$ where J = 7/2) would be destroyed, leaving only weak Van Vleck paramagnetism which can coexist with superconductivity. Indeed, trivalent $Am^{3+}(5f^6)$ is a Van Vleck paramagnet which superconducts below 0.79 K [45]. Since other trivalent s,p,d-electron metals, Y, Sc, La and Lu all superconduct at temperatures 10-20 K at 1 Mbar pressure [7], one would anticipate that trivalent Eu superconducts at comparable temperatures. Eu was recently found to become superconducting for pressures higher than 80 GPa. However, we note that the value of its superconducting transition temperature $T_c \approx 2$ K and pressure derivative $\frac{dT_c}{dP} \approx +0.018$ K/GPa are both much less than those reported for the trivalent *s,p,d*-metals Sc, Y La, and Lu [47]. This was taken to indicate that to 142 GPa Eu does not become fully trivalent, but rather mixed-valent [7]. Other possibilities are that the Van Vleck paramagnetism of trivalent Eu weakens the superconducting state or that the crystal structure taken on by Eu in the pressure range of 80-142 GPa is not favorable for higher values of T_c.

Extending the previous x-ray diffraction studies on Eu metal to pressures above 80 GPa is important for several reasons: (1) to establish whether the sudden appearance of superconductivity near 80 GPa is associated with a structural phase transition, (2) to check whether Eu's EOS does indeed approach that of trivalent Gd near 20 GPa as reported earlier [38], (3) to test for pressure-induced trivalency in Eu by establishing whether at extreme pressures the structures taken on by Eu follow those of the regular trivalent lanthanide series.

In the present experiments on Eu metal to 92 GPa, three structure phase regions are observed: a bcc-to-hcp transition near 12 GPa, a mixed phase region from 18 to 62 GPa, and then a transition to a single-phase orthorhombic (*Pnma*) structure at 66 GPa which is retained to the highest pressure applied 92 GPa. This pressure-induced structure sequence is compared to the results of a theoretical calculations based on density function theory (DFT) carried out by Dr. R. Hennig's group at Cornell University and Dr. Y. Zhang at University of Nevada, Las Vegas. The present results suggest that above 15 GPa Eu is neither divalent nor fully trivalent to pressures as high as 92 GPa.

4.1.1 Experiment

High-pressure synchrotron angle-dispersive x-ray diffraction experiments were performed at beamline 16ID-B, HPCAT at the (APS) with the help of Y. Meng. A symmetric cell was used with 1/6-carat, type Ia diamond anvils with 0.18 mm culets beveled at 7 degrees out to 0.35 mm. The Re gaskets were preindented from the original thickness of 250 micron to 30 micron central thickness; a 60 µm dia. hole was electro-spark drilled through the center to form a sample chamber. The high-purity Eu sample (99.98% metals basis), obtained from R. W. McCallum and K. W. Dennis of the Materials Preparation Center of the Ames Laboratory [158], was loaded into the sample chamber in an Ar glove box due to the high reactivity of the sample. A small amount of Pt powder (∼20 µm) was placed on the sample as a pressure marker [159].

The monochromatic x-ray beam (29.879 keV, 34.221 keV and 29.130 keV) used in three separate experiments was focused to less than 10 µm at the sample location in both horizontal and vertical directions. Due to the soft nature of the sample, the pressure difference between the center and edge of the sample chamber is only 1 GPa at 88 GPa, allowing us to determine the critical pressure for a given phase transition quite accurately. Normally, the diffraction pattern shows only peaks from the sample and the Pt marker. However, for pressures of 55 GPa and above, weak peaks from the Re gasket were observed in some measurements due to the irregular shape of the gasket hole. Diffraction patterns were collected at room temperature and high pressures using an image plate detector (MAR345) with an exposure time of typically 2 to 15 s. The sample-to-detector distance was precisely calibrated using a NIST CeO2 standard.

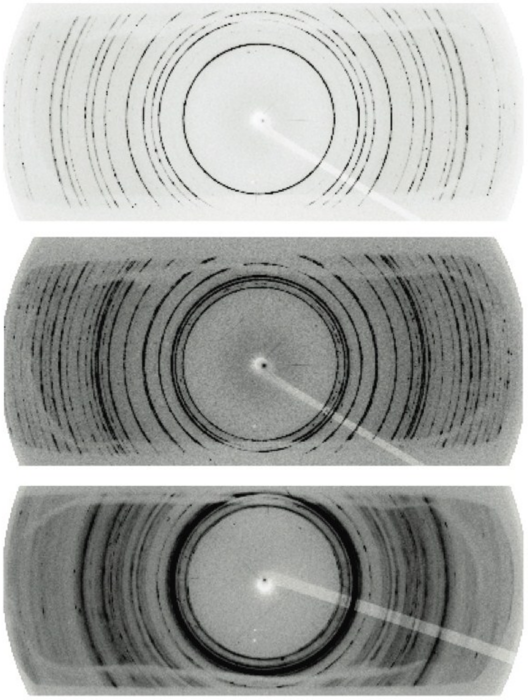

Figure 4.1: X-ray diffraction images of the Eu sample and Pt pressure marker at 4 GPa (top, bcc phase), 14 GPa (center, hcp phase) with $\lambda = 0.41493$ Å beam and 2 s exposure time, and at 92 GPa (bottom, orthorhombic phase) with $\lambda = 0.36229$ Å beam and 15 s exposure time.

Figure 4.1 shows x-ray diffraction images of Eu at pressures of 4, 14 and 92 GPa. In order to be consistent with the superconductivity experiments [7], no pressure medium was used in the present studies. The x-ray diffraction peaks became quite broad at the highest pressures (see the data at 92 GPa), presumably due to sizable strains in the sample from the non-hydrostatic pressure environment. The results of these diffraction experiments are discussed in detail.

4.1.2 Results from Density Functional Theory Calculations

Structure searches carried out by Prof. R. Hennig's group at Cornell University were performed with the random search method and in-house evolutionary algorithm at pressures of 0, 20, 40, 60 and 80 GPa for structures with up to 8 atoms per unit cell for the random search method and up to 30 atoms per unit cell for the evolutionary algorithm. The search discovered a large number of candidate crystal phases with low enthalpies (bcc, fcc, hcp, $Fdd2$, $Pnma$, $Fddd$, Cc, $Imm2$, R-$3m$, $C2/m$ and $C2/c$). All of these structures have enthalpies within a range of 50 meV/atom.

The enthalpy as a function of pressure for all of these trial structures were calculated. Figure 4.2 shows the enthalpies of the predicted ground state structures and their stability ranges. It is found the bcc phase at low pressures and a transition to the hcp structure at 10 GPa. At a pressure of 16 GPa a transformation to the $C2/c$ structure, at 22 GPa to the $Fdd2$ structure, and at 34 GPa to the Pnma structure were predicted. The $Pnma$ structure is nearly degenerate to the $C2/c$ structure, and the $C2/c$ phase is slightly lower in enthalpy above 46 GPa. However, these enthalpy differences are below the accuracy limits of current approximations of the exchange-correlation functional in DFT calculations [164].

Another DFT calculation using unit cells containing four Eu atoms was carried out independently by Y. Zhang from University of Nevada, Las Vegas. The known bcc and hcp of Eu at ambient pressure and at 15 GPa were predicted successfully. It is then used to search for structures at higher pressures. Structural searches at 25, 30, 45, 70, and 90 GPa were performed. As shown in Figure 4.3, these calculations find that orthorhombic Eu with the space group $Pnma$ (No. 62) is stable from 25 to 70 GPa. At a pressure of 90 GPa, hcp Eu with the space group $P6_3/mmc$ (No. 194) reappears.

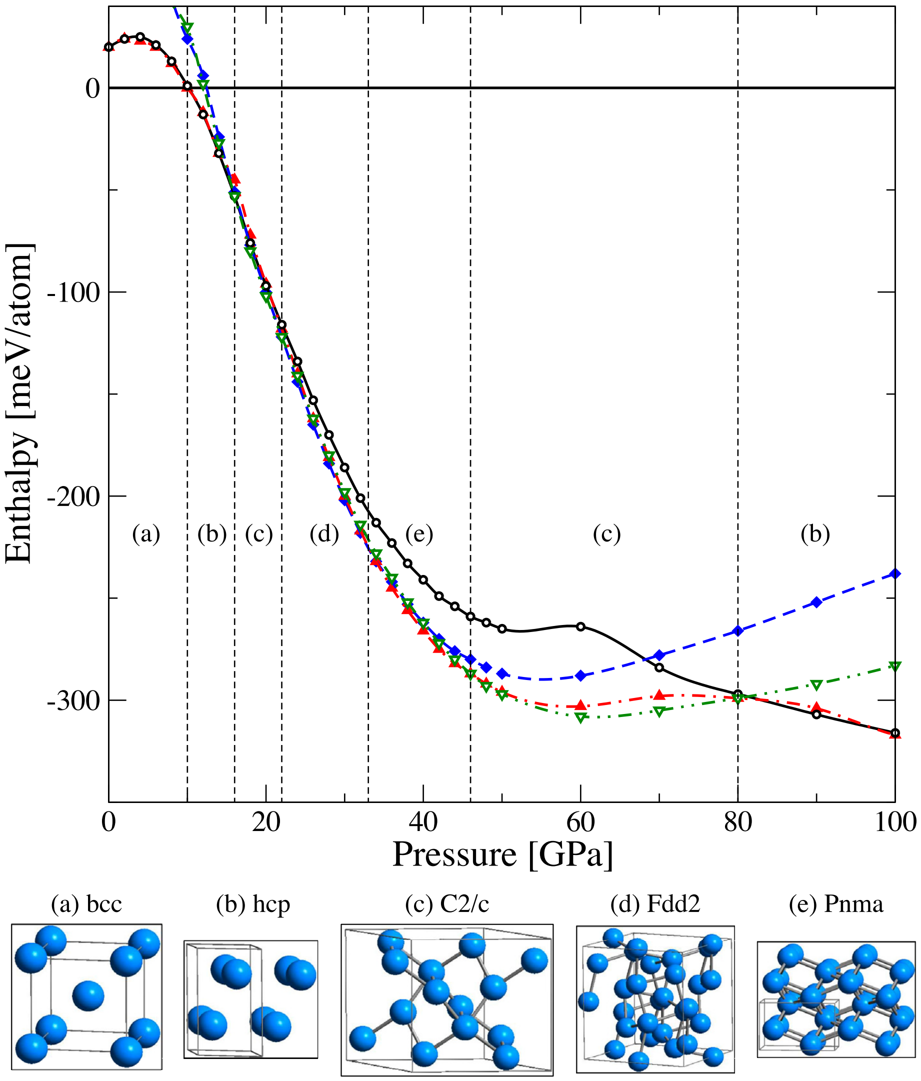

(a) bcc (b) hcp (c) C2/c (d) Fdd2 (e) Pnma

Figure 4.2: Results of structure search at Cornell University showing the enthalpies of possible crystal structures of Eu relative to the bcc phase as a function of pressure up to 100 GPa. The calculation predicts a structure sequence from bcc$\rightarrow$hcp$\rightarrow C2/c\rightarrow Fdd2\rightarrow Pnma\rightarrow C2/c\rightarrow$hcp. Figure legend: (a) bcc (horizontal line), (b) hcp (open circle), (c) $C2/c$ (open triangle), (d) $Fdd2$ (diamond), (e) $Pnma$ (solid triangle).

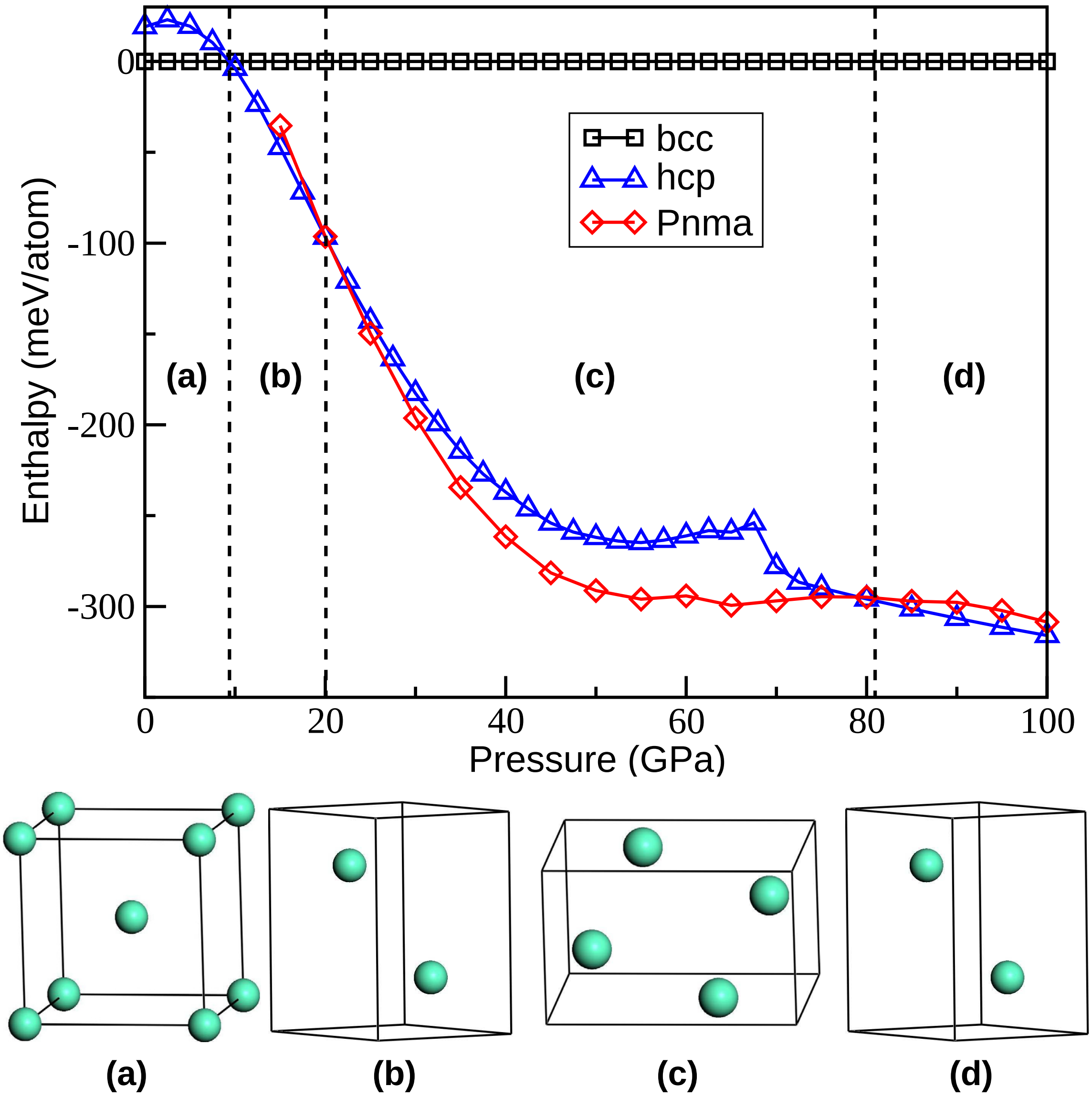

Figure 4.3: Results of density function theory calculations at University of Nevada, Las Vegas showing the enthalpies of possible crystal structures of Eu metal relative to that for the bcc phase as a function of pressure to 100 GPa: (a) bcc (square), (b) hcp $P6_3/mmc$ (triangle), (c) orthorhombic $Pnma$ (diamond), (d) hcp $P6_3/mmc$ (triangle).

The calculated enthalpies as a function of pressure for the hcp and *Pnma* structure relative to that of bcc Eu are plotted in Figure 4.3. They show that bcc Eu would be expected to transform to hcp at about 10 GPa and then to *Pnma* above 20 GPa. In the calculations the hcp structure with four-atom orthorhombic unit cell was used by applying the transformation $a' = 2a + b$, $b' = b$, $c' = c$, where a, b and c are lattice vectors of the primitive hcp cell. The corresponding atomic position is (1/6, 1/2, 1/4) and the ratio of $|a'|/|b'|$ is $\sqrt{3}$. For the *Pnma* structure, the typical atomic position has the form $\{(1/6, -x + 1/2, 1/4)\ 0 < x < 0.1\}$ and the ratio $|a'|/|b'|$ deviates from that of hcp structure. Therefore, the *Pnma* structure can be viewed as a distorted hcp structure in the orthorhombic cell. However, new intermediate structures with more than four atoms per unit cell could still be possible in this pressure region. The hcp structure has lower enthalpies than the *Pnma* structure above 80 GPa.

Differences in the findings of the two genetic algorithms of the Cornell University and University of Nevada groups are likely due to constraints placed on the search space. The 2nd search was constrained to 4-atom unit cells whereas the in-house code considered structures with up to 30 atoms per unit cell. Indeed, the stable structures found by Zhang are a subset of those found by the other search, and the two that it missed, $C2/c$ and $Fdd2$, both have unit cells of greater than 4 atoms.

In the pressure-induced superconducting state in Eu metal, the underlying electron pairings could be mediated by lattice vibrations (BCS framework) as for Sc, Y, La, and Lu [47]. It is, therefore, interesting to calculate the lattice dynamics of Eu at high pressures. To this end the phonon density of states (PDOS) calculations were

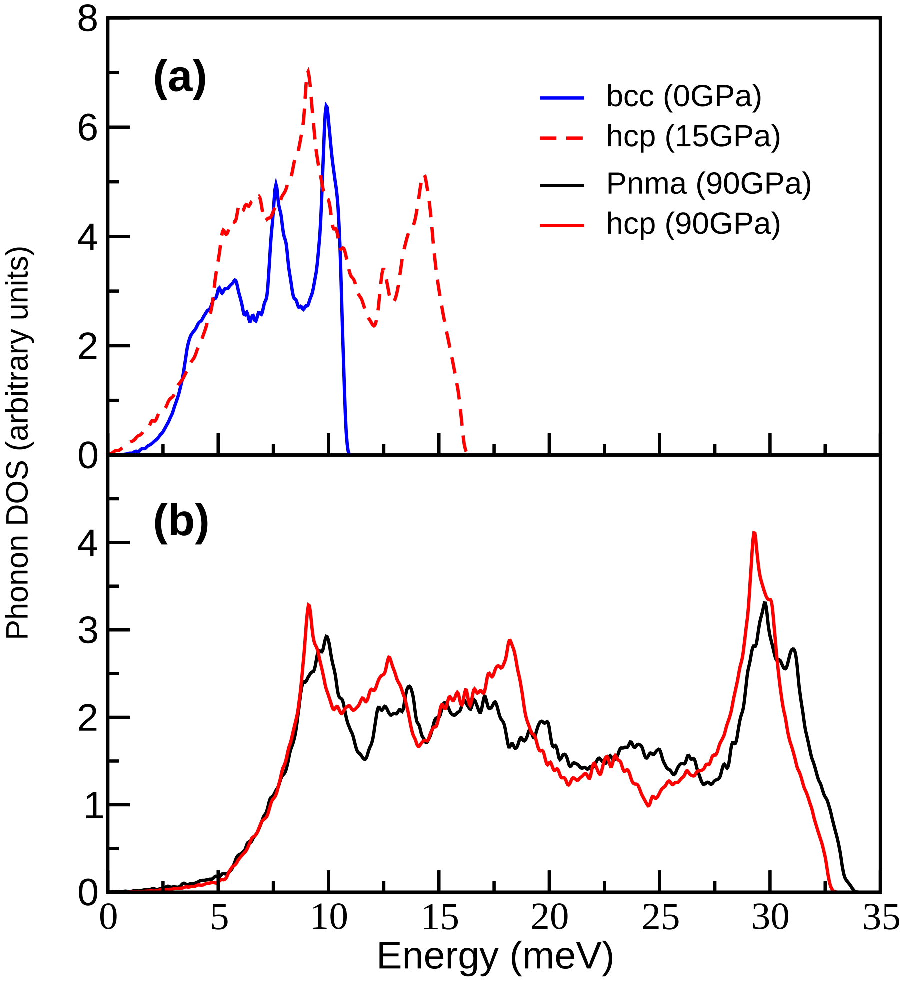

Figure 4.4: Density of phonon states of Eu versus energy for structures in Figure 4.3 at different pressures.

performed by Y. Zhang. The PDOS of bcc and hcp Eu at 0 and 15 GPa were first studied and are shown in Figure 4.4 (a). The obtained phonon peaks are consistent with previous calculations and experiment [49, 162]. Then the PDOS of both hcp and *Pnma* phase at 90 GPa were carried out (Figure 4.4) (b). The similarly positioned major peaks at 9 and 30 meV for both phases are ascribed to their close structural features. It is interesting to note that a major low-frequency PDOS peak at 9 meV is present in both the lower pressure (15 GPa) and higher pressure (90 GPa) hcp phases. Further evaluations of the electron-phonon coupling strength, as well as parallel work on La and Lu, are needed to gain a detailed understanding of superconductivity in Eu at high pressures.

We note that Nixon and Papaconstantopoulos [166] have recently calculated the electronic structure of Eu for the bcc, hcp, and fcc structures to 90 GPa pressure using the augmented-plane-wave method in the local-density approximation. Using a simple Debye model to approximate the change in the average phonon frequency under pressure, they find that in both the bcc and hcp phases Eu becomes superconducting above 60 GPa, increasing to a value near 2 K at 80 GPa, in agreement with experiment [7].

4.1.3 Experimental Results

The data analysis was carried out with the help of Dr. Y. Meng from HPCAT and Dr. R. Kumar from Nevada University, Las Vegas. In our data analysis the two-dimensional images (see Figure 4.1) were integrated to give intensity as a function of diffraction angle (2ϑ) using the software FIT2D [83]. The integrated spectra were then indexed in software Jade. The Le Bail and Rietveld refinements were performed using LHPM-RIETICA [84] and GSAS [85].

Three separate high-pressure experiments were carried out. In the first run, XRD data were collected at pressures from 4 to 43 GPa; a gasket failure prevented measurements to higher pressures. In the other two runs, the highest pressure reached was 92 GPa. In all three experiments, diffraction images were collected at 2-5 GPa intervals with increasing and decreasing pressure. The observed phase transition pressures in these experiments are consistent with each other.

Typical x-ray diffraction spectra for Eu metal at four pressures to 35 GPa, including the results of a full-profile Rietveld refinement for bcc (Im-$3m$) and hcp ($P6_3/mmc$), are shown in Figure 4.5. Since Pt was used as an internal pressure standard, its fcc (Fm-$3m$) phase is included as a second phase in the refinement. The anticipated abrupt phase transition in Eu from bcc to hcp near 12 GPa is clearly observed. Above 18 GPa several new peaks begin to appear as shown with arrows in Figure 4.5, indicating a sluggish phase transition. This result is consistent with studies by Takemura and Syassen [38] where silicone oil served as pressure medium. In the present experiments the spectra up to 28 GPa can still be indexed with hcp if the weak peaks are excluded. Above 30 GPa the phase change proceeds more rapidly. The anomalies at 18 and 28 GPa observed by Bundy and Dunn [46] in the room-temperature electrical resistivity are possibly related to these changes in structure.

In our first attempt to solve the post-hcp phase we tried a multiple hcp cell with

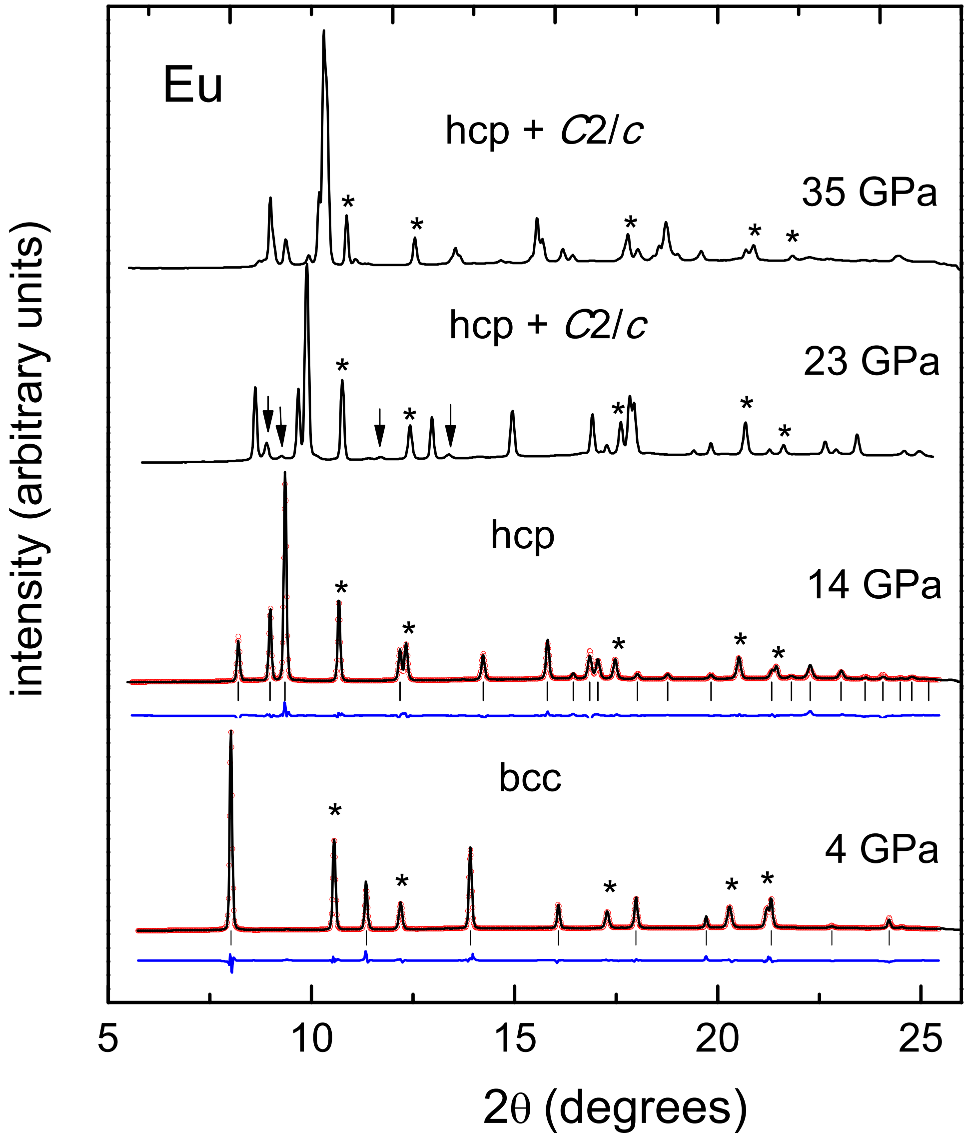

Figure 4.5: Representative high pressure x-ray diffraction spectra of Eu (black lines, wavelength λ = 0.41493 Å) from 4 to 35 GPa with Rietveld full-profile refinements (red lines) for bcc and hcp phases. The tickmarks in the 4 GPa and 14 GPa plots correspond to positions of diffraction peaks of Eu. Below the tickmarks are the difference plots between calculated and observed spectra. Pt peaks are identified by asterisks in all spectra.

36 atoms ($a' = a$, $c' = 18c$, a and c are the cell parameters from previous hcp phase), as proposed by Takemura and Syassen [38]. However, such a multiple hcp cell, which is quite unusual, would yield a large number of diffraction peaks not observed in the present experimental data. We also considered the orthorhombic $Fdd2$ space group suggested by the theoretical prediction shown in Figure 4.2. However, Fdd2 has a large unit cell with 40 atoms and has high-intensity peaks at angles lower than the first peak observed in our experiments, irrespective of the actual atomic positions. Even though the indexing of the XRD patterns above 18 GPa show agreement with both $P1$ and $C2/c$ space groups, the $C2/c$ space group seems more likely as the symmetry is higher and also the theoretical calculations above 18 GPa find the enthalpy of the monoclinic $C2/c$ structure to be the lowest among the candidates examined (see Figure 4.2). Hence, this phase is assigned as the post hcp phase and further refinements were carried out in the mixed-phase region between 18 and 62 GPa.

As pressure is increased to 41 GPa, an orthorhombic phase $Pnma$ coexisting with $C2/c$ appears (Figure 4.6). The refinement of the mixed phase at 55 GPa is shown in Fig. 6 including the Le Bail fit of $C2/c$ with cell parameters a = 3.134(3) Å, b = 4.970(7) Å, c = 9.301(5) Å, $\beta = 106.65(10)^\circ$ and Rietveld fit of $Pnma$ with cell parameters a = 5.042(2) Å, b = 4.357(2) Å, c = 3.023(1) Å with Eu on 4c sites and $x = 0.327(1)$, $y = 1/4$, $z = 0.035(1)$. From 41 to 92 GPa, the two peaks (see arrows in Figure 4.6) belonging to the $C2/c$ phase, which cannot be indexed with $Pnma$, gradually merge into the next peak at higher angle. Above 66 GPa both peaks have vanished and the spectra can be indexed as single phase $Pnma$. The cell parameters of

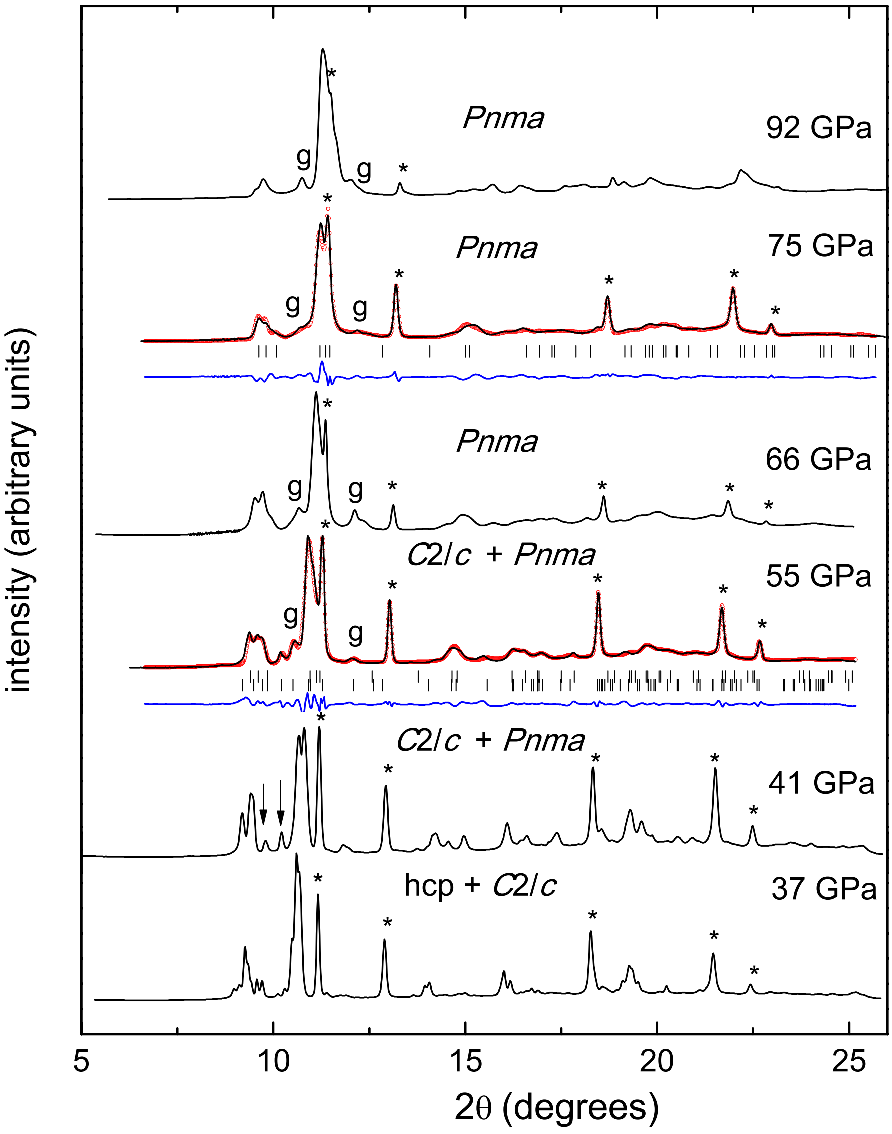

Figure 4.6: Selected x-ray diffraction spectra of Eu (black lines, wavelength $\lambda = 0.4256$ Å) including the refinements (red lines) at 55 and 75 GPa showing the sluggish transition from $C2/c$ to *Pnma*. In the plot for 55 GPa, the tickmarks correspond to the positions of diffraction peaks from Eu's *Pnma* phase (upper) and $C2/c$ phase (lower). In the plot for 75 GPa, tickmarks show the peak positions from Eu's *Pnma* phase. The blue lines below the tickmarks show the difference plots between fits and data. Asterisks indicate peak positions from Pt. The letter "g" marks peaks from Re gasket.

	P = 4 GPa *Im*-3*m* (bcc)	P = 14 GPa $P6_3/mmc$ (hcp)	P = 75 GPa *Pnma* (orthorhombic)
Cell parameters (Å)	a = 4.1961 (1) [4.14]	a = 3.3501(1) [3.32] c = 5.2962(2) [5.00]	a = 4.977(1) [4.77] b = 4.264(1) [4.13] c = 2.944(1) [2.78]
Atomic position parameters	$x = 0$ $y = 0$ $z = 0$	$x = 1/3$ $y = 2/3$ $z = 1/4$	x = 0.325(1) [0.33] $y = 1/4$ z =0.029(2) [0.08]
Refinement residue (R_{wp}) (%)	5.4	5.6	5.8

Table 4.1: Cell and atomic position parameters and refinement residues of Eu in bcc, hcp and orthorhombic structure at room temperature. Calculated lattice parameters keeping the f-electrons in the core are given in square brackets. The deviations between the experimental and computed lattice parameters increase with pressure, reaching values up to about 6%.

Pnma at 75 GPa are a = 4.977(1) Å, b = 4.264(1) Å, c = 2.944(1) Å and the Rietveld refinement is shown in Figure 4.6.

Table 4.1 summarizes the cell and atomic position parameters and refinement residues for bcc, hcp, and orthorhombic *Pnma* at selected pressures. Since the phase transition from hcp to $C2/c$ and then to *Pnma* is sluggish and continuous, we are unable to determine the detailed atomic arrangement for $C2/c$.

4.1.4 Discussion

The lattice parameters and their ratios are plotted under pressure to 92 GPa in Figure 4.7. Between 12 and 35 GPa the parameters are obtained based on the peaks from the hcp phase ($P6_3/mmc$), while above 35 GPa the peaks from orthorhombic (*Pnma*) are used. The agreement with the lattice parameters from Reference [38] is reasonable. As seen in the Figure 4.7 (b) , the c/a ratio shows a slope change near 18 GPa when Eu enters a mixed phase. The change in the slope of c/a versus pressure may signal a

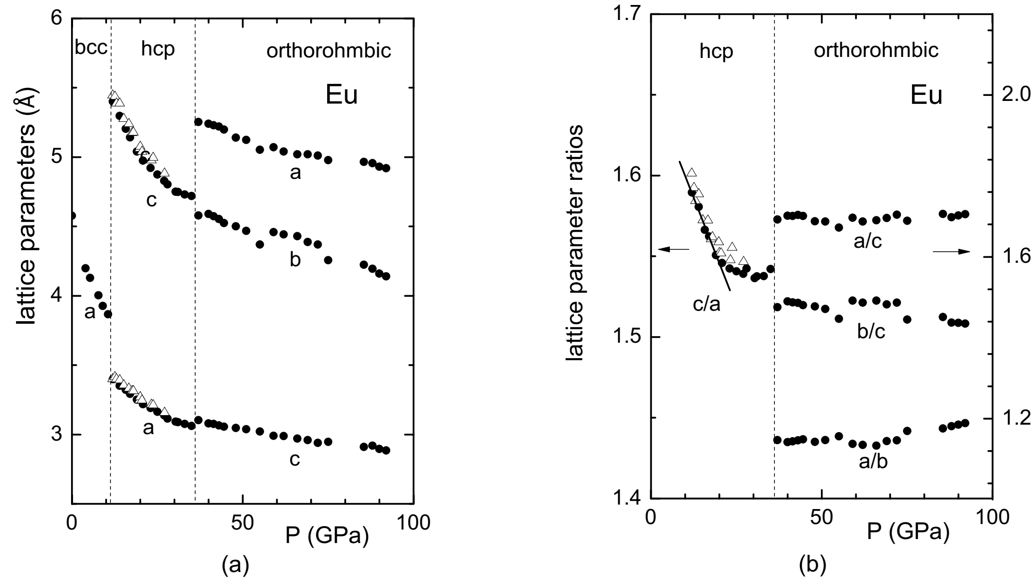

Figure 4.7: For Eu pressure dependence of (a) lattice parameters and (b) ratio of lattice parameters above 12 GPa. In the pressure range 12 - 35 GPa, the lattice parameters are obtained from the hcp phase, while 35 - 92 GPa from the orthorhombic phase. The agreement of the c/a values from this study (solid circles) with those from Reference [38] (open triangles) is reasonable.

pressure-induced magnetic transition [167,168].

In Figure 4.8 the relative volume V/V_o of Eu metal, where V_o is the molar volume at ambient pressure, is plotted versus pressure and compared to previous results [38, 43,157]. For pressures between 18 and 37 GPa, where Eu shows a mixed phase of hcp and $C2/c$, the volume is calculated from the hcp structure and at higher pressures from the *Pnma* structure. Corresponding to the change in slope of c/a in Figure 4.8 (b), there is a slight anomaly in V(P) near 18 GPa. All V/V_o data are tabulated in Table 4.2. The volume-pressure dependence found in the present study is seen to be in good agreement with the previous static data to 43 GPa [157]. The fit of the V(P) data in the bcc phase to 12 GPa using the third order Birch-Murnaghan equation [36]

bcc (Im-$3m$)		hcp ($P6_3/mmc$)		orthorhombic ($Pnma$)	
P (GPa)	V/V$_o$	P (GPa)	V/V$_o$	P (GPa)	V/V$_o$
0	1	12.0	0.564	40.0	0.386
4.0	0.771	14.0	0.537	41.5	0.383
5.3	0.734	15.8	0.519	43.0	0.380
7.8	0.669	17.0	0.503	44.5	0.375
9.0	0.631	19.0	0.481	48.0	0.367
10.6	0.603	20.8	0.465	51.0	0.363
		23.0	0.452	55.0	0.358
		25.0	0.441	59.0	0.352
		27.0	0.430	62.0	0.346
		28.0	0.420	66.0	0.344
		30.4	0.413	69.0	0.338
		31.0	0.410	72.0	0.331
		33.0	0.404	75.0	0.325
		35.0	0.396	85.5	0.315
		37.0	0.391	88.0	0.312
				90.0	0.310
				92.0	0.308

Table 4.2: V/V$_o$ data of Eu for increasing pressure to 92 GPa. The ambient pressure molar volume V$_o$ = 28.98 cm^3/mol [38] is used.

yields the bulk modulus $B_o = 10.9(6)$ GPa and the pressure derivative $B_o^{\prime} = 3.0(2)$, both of which are close to published values [38, 43, 157].

As seen in Figure 4.8, the present V(P) data for both increasing or decreasing pressure agree reasonably well. The pressure at which a given phase transition occurs agrees within 1-2 GPa for all three runs for both increasing and decreasing pressure. The relative volume jump at the bcc-to-hcp transition at 12 GPa is ~3% which is comparable to the value 4% reported in Ref. [38]. No measurable volume discontinuity is observed for the phase transitions at higher pressures.

In Figure 4.9 the molar volume of Eu is plotted versus pressure to 100 GPa (1 Mbar) and compared to data on the neighboring trivalent lanthanides Nd [169], Sm [170],

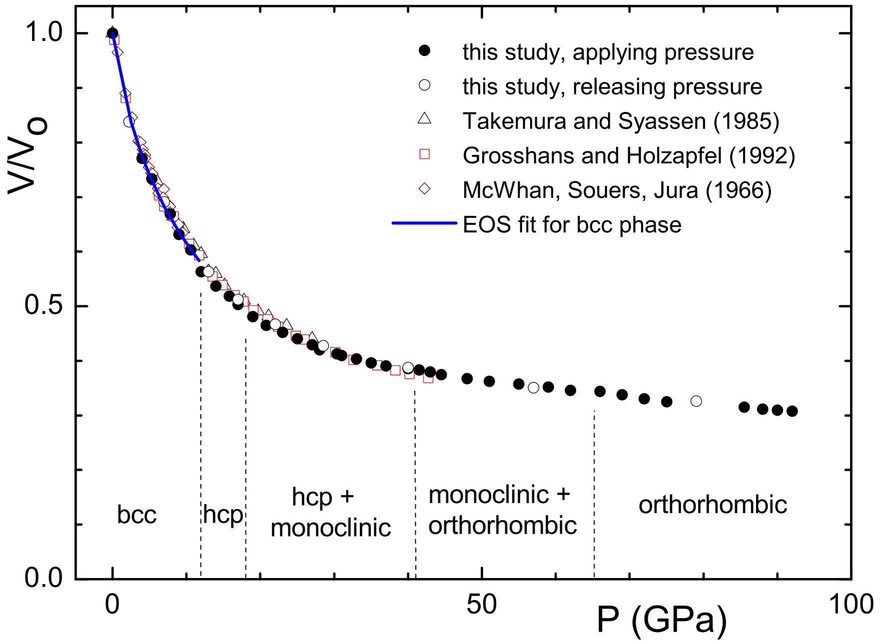

Figure 4.8: Equation of state at ambient temperature for Eu to 92 GPa from present studies compared to earlier work by Takemura and Syassen [38], Grosshans and Holzapfel [157], and McWhan, Souers, and Jura [43]. The V(P) fit in the bcc phase is obtained using the third order Birch-Murnaghan equation [36] (see text).

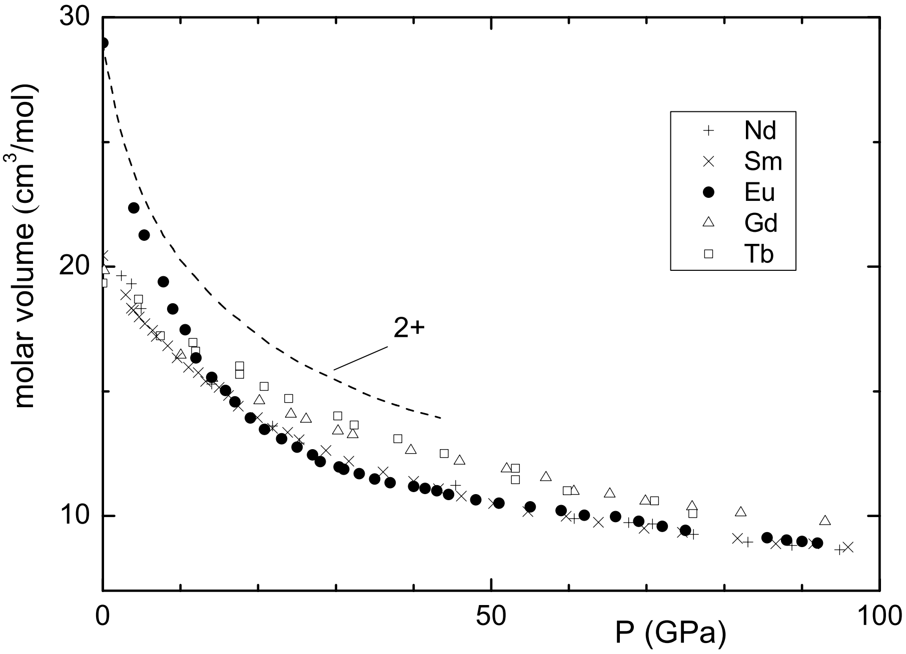

Figure 4.9: Comparison of pressure-dependent molar volume of trivalent Nd [169], Sm [170], Gd [44], and Tb [171] to present results for Eu. Dashed line is calculation for divalent Eu by Johansson and Rosengren [39].

Gd [44], and Tb [171]. The calculated molar volume for Eu in the divalent state to 42 GPa from Johansson and Rosengren is also shown (dashed line). From this figure the molar volume of Eu is seen to initially decrease rapidly under pressure from its large divalent value, falling somewhat below that for trivalent Gd at 10-20 GPa, in agreement with earlier studies by Takemura and Syassen [38]. As these authors point out, this suggests that Eu is no longer divalent above 10-20 GPa, but rather mixed valent or possibly trivalent. A fully trivalent Eu state, however, does not appear likely to pressures as high as 92 GPa since none of the structures observed under pressure in the present experiment (bcc→hcp→mixed phase→primitive orthorhombic (*Pnma*)) has been observed to pressures exceeding 1 Mbar for the neighboring trivalent rare earth metals Nd [169], Sm [170], Gd [44] and Tb [171] or, for that matter, for any of the other trivalent rare-earth metals. At 90 GPa Nd, Gd, and Tb all take on the monoclinic structure $C2/m$. As pointed out by Takemura and Syassen [38], the fact that Eu's molar volume falls below that of trivalent Gd and Tb above 20 GPa does not necessarily imply that Eu is trivalent, but rather may arise from a mixing entropy term in a mixed valent state, as treated in the valence fluctuation model of Wohlleben [172].

In Figure 4.2 it is seen that the calculated enthalpies for the high-pressure phases $C2/c$, *Fdd*2 and *Pnma* lie quite close together between 16 and 45 GPa so that the energetically favorable phase might not be able to form under the conditions of the present experiment. Besides the enthalpy barriers, the stress anisotropies in the present non-hydrostatic pressure experiment may also affect the value of the transition pressure and the phases assumed by Eu. The $C2/c$ phase predicted in Figure 4.9 for the pressure range 46 - 80 GPa thus might not appear in experiment. Both DFT calculations predict that the orthorhombic Pnma phase should transform into the hcp phase above 80 GPa. However, no further phase transition was observed after Pnma in the present experiment to 92 GPa. An extension of these synchrotron x-ray diffraction studies to higher pressures would test this prediction of both theories.

In summary, we have carried out x-ray diffraction experiments in a DAC on polycrystalline Eu metal under pressures to 92 GPa and have observed three pressure-induced phase transitions from bcc to hcp to a mixed phase and then to an orthorhombic *Pnma* phase above 66 GPa. That Eu's large molar volume reduces to a value below that of Gd for 10 - 20 GPa pressure would appear to indicate that Eu is no longer divalent at or above these pressures. Although the equation of state does not permit a reliable estimate of Eu's valence at 92 GPa, the fact that the crystal structures assumed differ from those exhibited by Eu's trivalent neighbors at similar pressures gives evidence that Eu does not reach full trivalency at 92 GPa.

The present structural studies are not able to illuminate the detailed relationship between the pressure-dependent superconductivity, valence, and structure in Eu. It seems likely that Eu is in a mixed-valent state when superconductivity appears at 84 GPa, but the value of the valence at this pressure remains undetermined. However, it does seem likely that the appearance of superconductivity is promoted by the structural transition at 66 GPa to orthorhombic *Pnma.* The fact that no superconducting transition was observed at 66 GPa could result from either a temperature-dependent structural phase boundary or because, from the measured derivative $\mathrm{d}\,T_c(P)/\mathrm{d}P \approx +0.018$ K/GPa [7],

T_c at 66 GPa would lie near 1.5 K which is just below the experimental temperature range.

To provide additional insight to the superconducting state in Eu, XANES, XMCD and SMS experiments were carried out to probe its valence and magnetic state to 87, 60 and 73 GPa, respectively, as discussed in the following section.

4.2 Valence and Magnetic State of Eu Metal under Pressure

Previous high pressure studies to 34 GPa on Eu's valence through XANES by Röhler [48] are interpreted to indicate that Eu enters a mixed-valent state in the bcc phase and the valence increases dramatically at higher pressure saturating at 2.64 above 24 GPa. Low temperature Mössbauer spectroscopy experiments are reported by Farrell and Taylor [127] to agree that Eu's valence increases to 2.4 at 12 GPa whereas the magnetization decreases; however, magnetic ordering in Eu was still present to 14 GPa. A more recent room temperature SMS experiment on Eu to 22 GPa by Wortmann *et al.* estimates Eu's valence to be 2.4 at 10 GPa and 2.55 at 17 GPa.

In order to investigate the valence and magnetic state of Eu metal to much higher pressures, we have carried out XANES, SMS and XMCD experiments at the APS under pressures as high as 87, 73, and 60 GPa, respectively.

4.2.1 XANES Experiment

A high-pressure room temperature XANES experiment on Eu was first performed at beamline 20-BM under general user proposal (GUP)-12789 with the help of N. Souza-Neto, D. Haskel, and Y. Meng from APS. In this run the symmetric cell was used together with two full anvils of the 180 μm culet beveled to 350 μm at 7°. In Röhler's XANES experiment setup, a foil Eu (∼3 μm thick) sample sandwiched with two layers of Al (Al-Eu-Al) was used. The foil sample was loaded vertically in a slit drilled in a beryllium gasket. X-rays went through the 3 μm sample and exited through the gasket. A Be gasket with ∼3 mm in diameter and ∼ 0.82 mm initial thickness was used due to its transparency to x-rays to avoid strong x-ray absorption by the diamond anvils at the low energy of Eu's L_{III} edge 6.97 keV. To avoid the strong absorption by two full diamond anvils (total height $\sim$ 4 mm), a similar setup was first tried with a slit drilled in a Be gasket provided by W. Yang at HPSynC, APS. The Be gasket was preindented to 20 μm. To duplicate Röhler's experiment and also have a uniform sample, a foil sample Al-Eu-Al prepared by K. W. Dennis and R. W. McCallum from the Ames lab [158] with total thickness of 10 μm and Eu thickness of 5 μm was used. The sample was cut into the right size and loaded vertically in a slit (20 μm × 70 μm) with x-ray going through the gasket instead of the diamond anvils. Since Be is extremely toxic and when it breaks it tends to pulverize, the symmetric cell was covered with Kapton tape to reduce the exposure. Pressure was determined using the ruby fluorescence technique.

A foil sample sealed with silicone oil and Kapton tape was first measured at ambient pressure to check the quality of the sample. The foil sample loading was first attempted inside the glovebox located at sector 3 with oxygen level $\sim$ 25 ppm. However, it was extremely challenging to load such a thin foil in a small slit. After a few failed sample loadings, we tried to load it in air. Since the Eu sample is sandwiched by the Al foils, it might be protected well enough from exposure to air. Then the sample was measured at 5 GPa. The absorption signal from the sample was excellent. However, the XANES spectrum showed two peaks with the second peak located 8 eV higher than the first peak, suggesting most of the sample had been oxidized due to the exposure to the air (Figure 4.10).

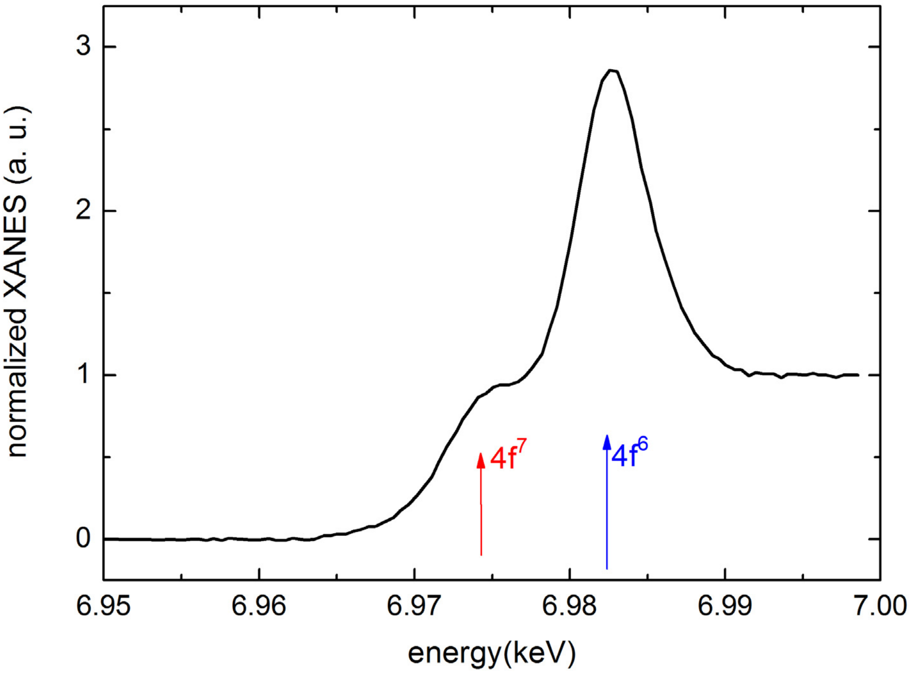

Figure 4.10: Oxidized Eu sample at 5 GPa showing two resonant absorption peaks.

In the second trial, we adopted the fluorescence geometry with a bulk Eu sample loaded in the glovebox. In fluorescence geometry, photons generated near the center of the gasket hole can not escape from the sample since they have to travel through the radius of the hole which is much larger than one absorption length and hence strongly attenuated. Therefore, the absorption spectra can be distorted with self-absorption from the thick sample (thickness $>> \frac{1}{\mu}$, where μ is the absorption coefficient at the Eu's L_{III} edge). Based on the sample profile scan, the x-ray was moved near the edge of the gasket hole so that the fluorescence photons can escape from the sample. Surprisingly, up to 39 GPa we did not see the strong transition toward Eu^{3+} as claimed by Röhler [48]. However, in fluorescence geometry the thickness of the sample where the x-rays pass through might be too large which results in a possible spectral distortion due to self-absorption. The data are, therefore, not very reliable.

In the third trial, a fully perforated anvil, a mini-anvil on one side and one partially perforated anvil on the opposing side (see Figure 3.9) with a 100 μm culet size were used to reduce the strong absorption from the diamond. In this setup, x-rays went through the diamond anvils with a total thickness of 0.7 mm in transmission geometry. Re was used as gasket and a circular hole with 50 μm diameter was drilled. A foil sample was loaded in the gasket hole inside the glovebox. Since x-rays went through the diamond anvils, the cell has to be rotated to avoid seeing the intense sharp Bragg peaks from the single crystal diamond near the absorption peak. We successfully measured the L_{III} edge absorption in transmission geometry up to 22 GPa. Figure 4.11 shows the normalized XANES spectra under pressures 0.2, 5, 8.4 and 21.6 GPa. However, at the

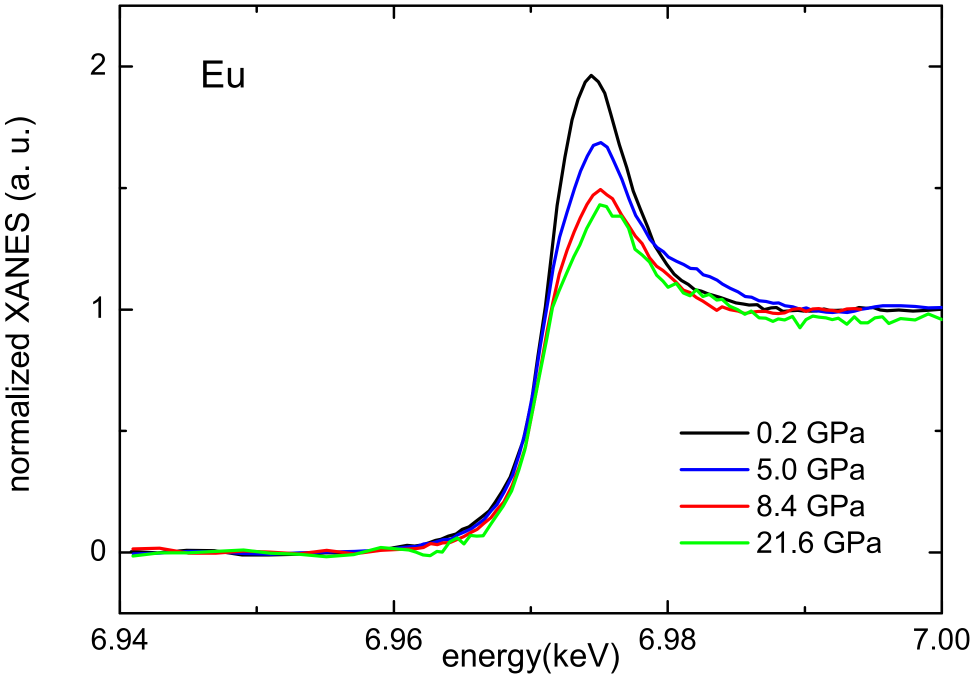

Figure 4.11: Normalized XANES spectra of Eu under pressure in transmission geometry with one fully perforated anvil and a mini-anvil on one side and one partially perforated anvil on the opposing side. The highest pressure 21.6 GPa may have been overestimated (see text).

highest pressure 21.6 GPa, the pressure was determined from a piece of ruby located outside the hole. The hole was started $\sim 15\ \mu m$ off-center at ambient pressure and under pressure it moved to one side. At lower pressure, we noticed the pressure at the center of the culet was higher than that at the center of the sample. Therefore, it is expected that the sample pressure was a few GPa lower than the measured 21.6 GPa. The spectrum for this final measurement was also measured in a much shorter time and thus was very noisy.

As seen in Figure 4.11, the resonant absorption peak intensity decreases with pressure and no obvious valence transition toward Eu^{3+} is observed in the bcc phase. When further pressure was applied, the pressure did not go up, presumably because the gasket hole moved to almost the edge of the culet. Since the beam time ran out, this experiment had to be terminated.

In the three trials of different geometries we established that the transmission geometry with perforated anvils would be the best choice for measuring the XANES at Eu's L_{III} edge to Mbar pressure. However, with the relatively fragile mini-anvil it is still very challenging to achieve a pressure as high as 80 GPa.

To check the results from our previous XANES measurements that no obvious valence transition was observed in the fluorescence and transmission geometries, another experimental run was performed three months later at beamline 4ID-D, APS. In this run a partially perforated anvil and a full anvil were used (see Figure 3.10). Two CuBe cells from easyLab and one symmetric cell were prepared before the experiment. One CuBe cell was mounted with 300 μm culet anvils, and another with 100 μm culet anvils. In the symmetric cell anvils with 100 μm culets were mounted. Re gaskets were preindented to $\sim$ 50 μm and a hole of 120 μm diameter was drilled for the 300 μm anvils and to $20 - 30$ μm and a circular hole of 45 μm was drilled for the 100 μm anvils. The x-ray beam, was focused to 120 × 180 μm^2 with a toroidal mirror, was reduced to 30 × 30 μm^2 with a slit.

The CuBe cell with 300 μm culet anvil was first used due to the large beam size. Since the ruby measurement system using the green laser at 4ID-D was limited to 50 GPa, higher pressures had to be measured at sector 16, HPCAT. In order to be able to move the cell conveniently, we did not attach the membrane but used the CuBe cells with screw drive. The Re gasket was first preindented to 45 micron and a hole of 120 μm was drilled at the center of preindented area. Ruby was used for pressure determination and silicone oil with viscosity of 1000 cSt was used as pressure medium. A freshly prepared Al-Eu-Al foil sample sealed in Kapton tape and silicon oil was measured to check the sample quality. A single layer of foil sample cut to $\sim$100 μm from the same parent foil was loaded into the gasket hole inside the glovebox with the oxygen level of 25 ppm. Since x-rays passed through the diamond anvils with thickness of 2.1 mm, the cell was rotated to get rid of the diamond Bragg peaks within the energy range of 6.93 keV to 7 keV at each pressure. In this cell, XANES spectra at 1, 5.6, 7.2, 9.2, 12.2, 15.3, 17 and 23 GPa were measured. At each pressure, 2-4 scans were collected and averaged. Under pressure, the foil sample became thinner and thinner, and the increasing background made the normalization more difficult than at lower pressures (see in Figure 4.12).

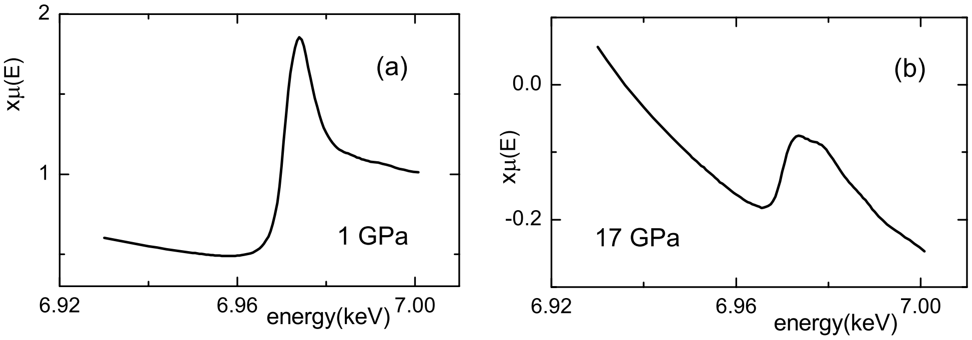

Figure 4.12: XANES spectra from a single Eu foil before normalization at 1 GPa (a) and 17 GPa (b).

Figure 4.13 shows the XANES measurements to 23 GPa. Similar to the bcc phase in Figure 4.11, the resonant peak intensity comes down with pressure and there is no obvious change in the line shape. Above 12 GPa, in hcp phase, the peak becomes broadened and a double-peak feature starts to appear. Under pressure the 2nd peak moves gradually toward higher energy. No edge energy shift by 8 eV was observed.

Three layers of foil sample were loaded in the 50 μm hole in the Re gasket without any pressure medium with anvils of 100 μm culet size mounted on the symmetric cell. Spectra at 6.7, 10.4, 23.5, 31.3 GPa were measured. However, under pressure the sample became almost as thin as the previous single foil sample. Even without any pressure medium, the spectra measured agree well with the previous measurements of a single foil. Then four layers of foil sample were loaded in the CuBe cell without any pressure medium. Spectra at 1.7 GPa, 7.1 GPa, 13.2 GPa, and 35.2 GPa were measured. The measurements agree well with the previous ones. However, at 35.2 GPa, the sample still became too thin to get a good measurement.

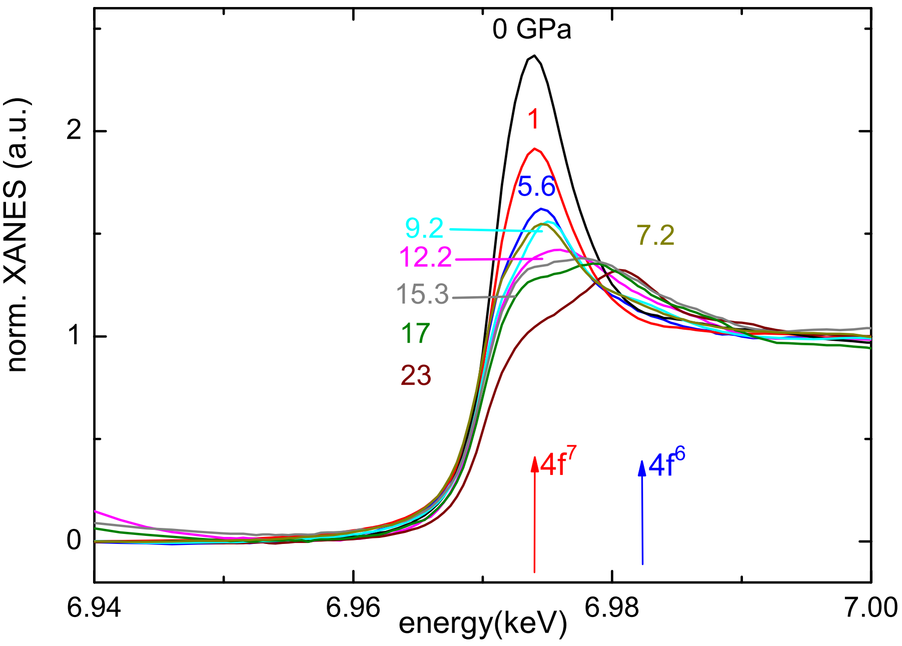

Figure 4.13: Room temperature XANES spectra of Eu under pressure to 23 GPa. The measurements were performed at beamline 4ID-D, APS.

From the above trials we learned that in order to achieve good measurements at pressures above 30 GPa, the sample must be sufficiently thick at the beginning of the pressure cycle. Further trials were made with bulk samples loaded in the cells. Firstly, a sample about 30 μm thick was loaded in the cell with 300 μm anvils. At 1.2 GPa and 8.7 GPa, the spectra did not show any resonant peak due to the self-absorption from a thick sample (see Figure 4.14). When pressure was increased to 18.3 GPa, the sample was thin enough to observe the absorption peak. At 18.3 GPa, the spectrum agrees well with that at 17 GPa for the single foil sample. Knowing that the bulk sample worked at high pressure, we decided to release the pressure and switch to the cell with 100 μm anvils with a thinner sample in order to go above 80 GPa. Upon releasing pressure, 10 and 0.4 GPa were measured.

A new bulk sample was loaded in the CuBe cell with anvils of 100 μm culet. The hole shrank from 50 μm at ambient pressure to $\sim$ 35 μm at 87 GPa. To make sure that the x-ray beam is smaller than the sample size at highest pressure, a smaller slit 20 $\mu m \times 20$ μm was used. XANES spectra were measured at 7.3, 27.4, 35.8, 41.4, 51, 61.2, 69, 79, 87 GPa. The sample thickness decreases under pressure to 51 GPa, and at higher pressure, the sample thickness did not change much. Even at the highest pressure measured 87 GPa, the sample thickness is larger than the sample thickness in the 4 layers of foil at 35.2 GPa. The pressure was then released to 9.7 and 2.0 GPa slowly. However, when the pressure was released to 2.0 GPa, the sample was oxidized and the two peaks corresponding to $Eu^{2+}$and Eu^{3+} were observed. (Figure 4.15)

From the XANES measurements, it is observed that in the bcc phase the resonant

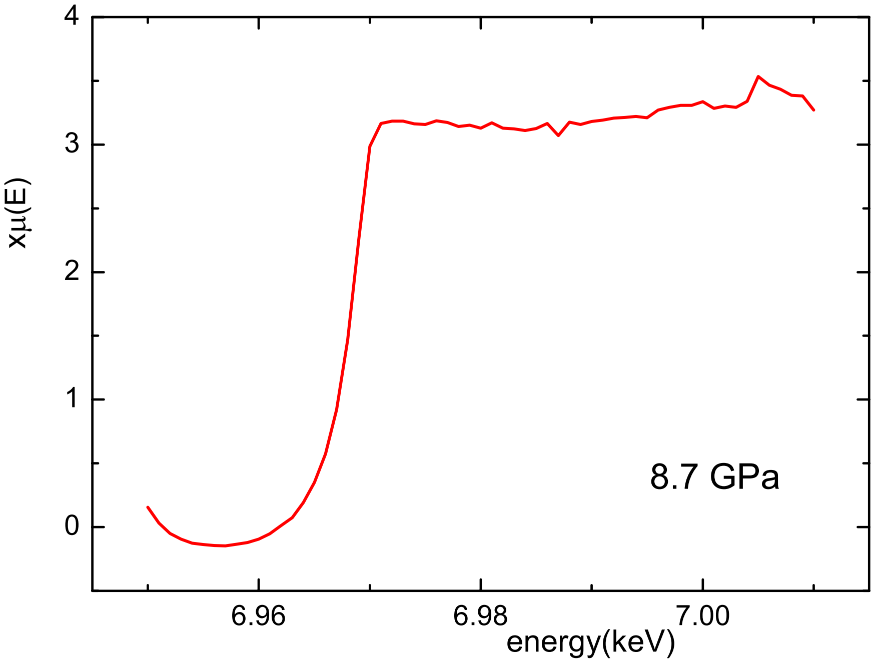

Figure 4.14: XANES spectra of a thick Eu sample at 8.7 GPa.

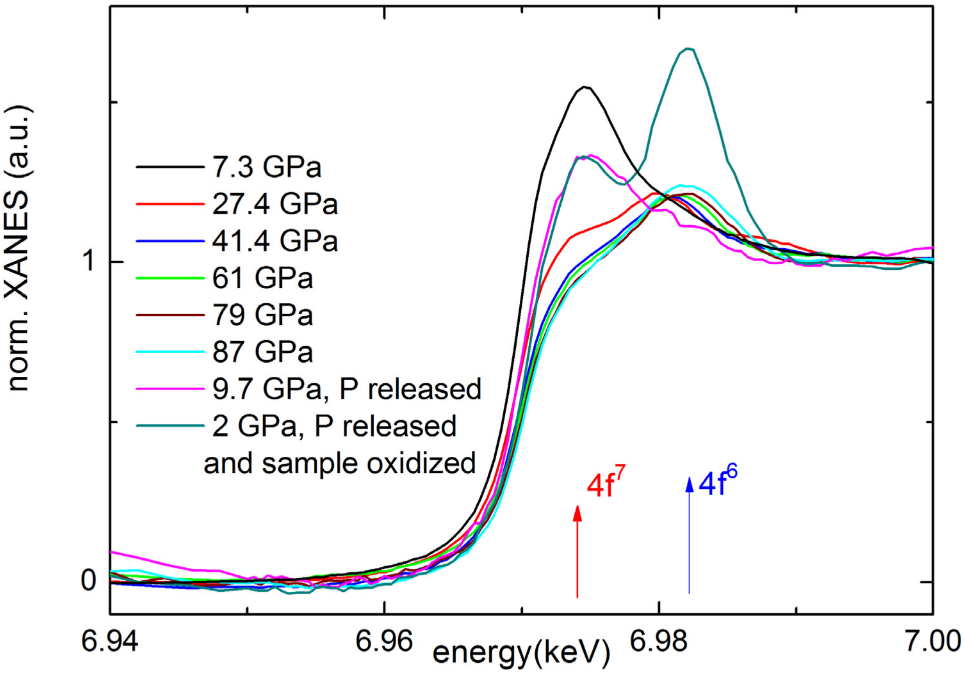

Figure 4.15: Normalized XANES spectra of a bulk Eu under pressure from 7.3 GPa to 87 GPa on increasing pressure and 9.7 GPa and 2 GPa on releasing pressure. In the last pressure measured (2 GPa) the sample was oxidized.

peak intensity decreases under pressure, but the spectral shape does not change and no valence change is observed as claimed by the previous XANES [48] and Mössbauer experiments [49, 127] where the valence was reported to reach 2.5 at 12 GPa. Above 12 GPa, in the hcp phase, a double-peak feature appears (Figure 4.13) and the second peak gradually shifts to higher energy with increasing pressure. At 23 GPa the second peak energy is around 6.980 keV, which is 6 eV higher than the resonant energy for Eu^{2+}. Above 41 GPa the spectra stay almost the same. In the experiment to 87 GPa there is no obvious edge shift toward higher energy.

In Röhler's XANES experiment [48] the spectrum was fitted with an arctan function and a Lorentzian function. He estimated the valence from the ratio of relative intensities of the two peaks corresponding to Eu^{2+} and Eu^{3+}. However, this method of data analysis ignores the fact that the structural transition also leads to spectral changes. Besides, the relative intensity of arctan and Lorentzian functions for Eu^{2+} and Eu^{3+} are arbitrary if Eu is in a mixed-valent phase. To analyze the data and get the valence more accurately, N. Souza-Neto carried out DFT-XANES simulations to 87 GPa. This simulations were done using LDA+U scheme. Although Eu orders antiferromagnetically at ambient pressure, its noncollinear antiferromagnetic state is difficult to simulate. Therefore, a ferromagnetic ground state was used instead. The U parameter used in these simulations places $4f$ electrons at about 1 eV below the Fermi energy level in agreement with the calculations from Turek *et al.* [173] which is more favorable to induce a valence transition than the 3 eV reported by Kunes *et al.* [174]. Figure 4.16 shows the simulated electron occupancy change under pressure from $4f$, $5d$

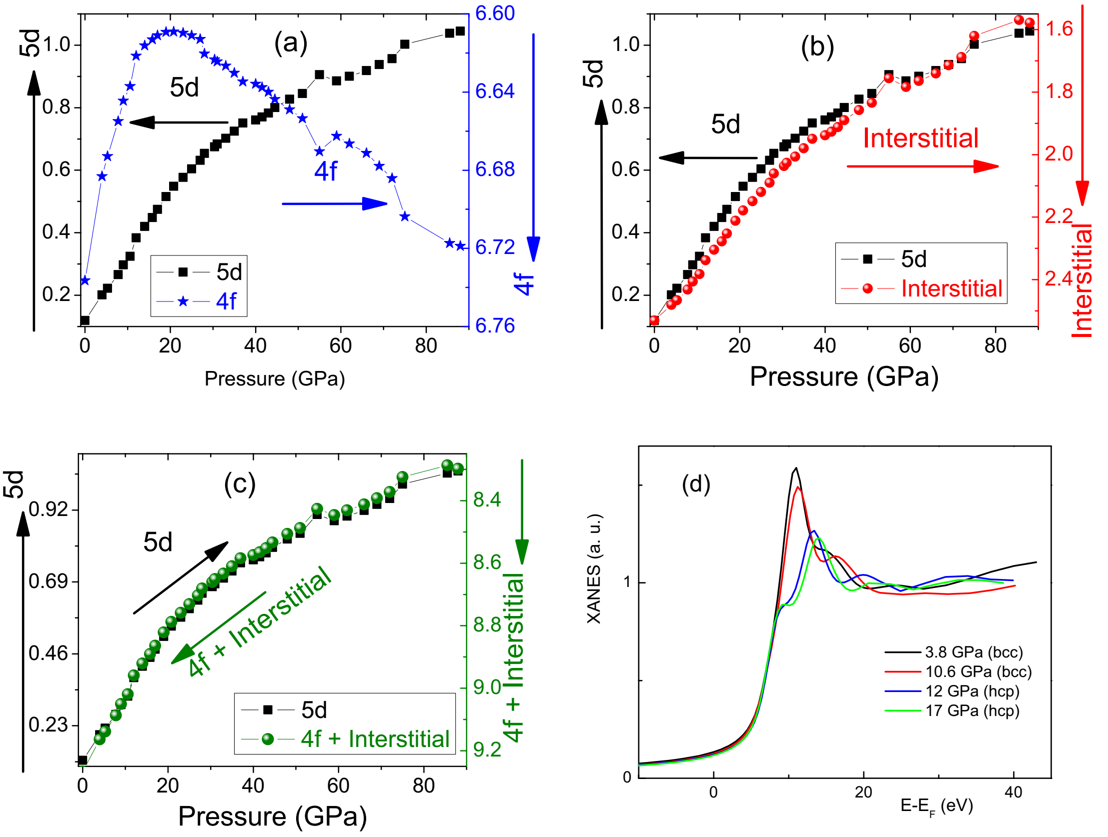

Figure 4.16: Electron occupancy from $5d$, $4f$ and interstitial (a, b, c). (d) shows the simulated XANES spectra in bcc and hcp phase.

and interstitial electrons and the XANES spectra up to 17 GPa.

Based on the simulations, $4f$ electron occupancy decreases by ~ 0.14 from ambient pressure to 20 GPa. Above 20 GPa the occupancy increases again to almost the ambient pressure value. The $5d$ electron occupancy increases monotonically with increasing pressure and at 88 GPa the $5d$ electron occupancy increases by almost 1. Simulations of interstitial electron occupancy show the 1 electron increase in $5d$ comes from the interstitial electrons. This increase in the $5d$ electron occupancy or decrease of empty states in $5d$ could explain the resonant intensity decrease under pressure especially in bcc phase observed in Figure 4.13 4.15. The change of $5d$ electron occupancy under pressure is exactly the same with the sum of $4f$ and interstitial occupancy as shown in Figure 4.16 (c). Based on the band structure calculations and the atomic structure determined from the x-ray diffraction experiments discussed in section 4.1, the corresponding XANES spectra in bcc and hcp phase were calculated as shown in Figure 4.17(d). Once Eu enters the hcp phase, the simulated spectra show a double peak feature which is consistent with the experimental data in bcc and hcp phase. Since there is only a 0.14 $4f$ electron occupancy change up to 20 GPa in the simulations, it is suggested that the spectra changes are structural in origin.

The simulated density of states for $4f$ and $5d$ under pressure are shown in Figure 4.17. The $4f$ density of state (Figure 4.17(a)) are broadened with increasing pressure to 88 GPa, while the $5d$ density of state shows an abrupt change at the bcc-hcp phase transition (Figure 4.17 (b)) and does not change much at higher pressure to 88 GPa except for a broadening induced by pressure (Figure 4.17 (c)). Therefore, the XANES spectra will not change much at higher pressures from 12 GPa to 88 GPa. Since between 18 and 66 GPa Eu is in a mixed phase, from 12 to 35 GPa lattice parameters from the hcp phase were used in the simulation, and above 35 GPa, from the orthorhombic phase *Pnma.* As seen in Figure 4.17 (d), whether hcp or *Pnma* is used in the simulation makes little difference in the $5d$ DOS.

The simulated magnetic moments for $4f$ and $5d$ are shown in Figure 4.18. The $5d$ magnetic moment increases under pressure to 88 GPa. And the increase at the bcc-hcp phase transition near 12 GPa is sudden. Together with the effect of decreasing

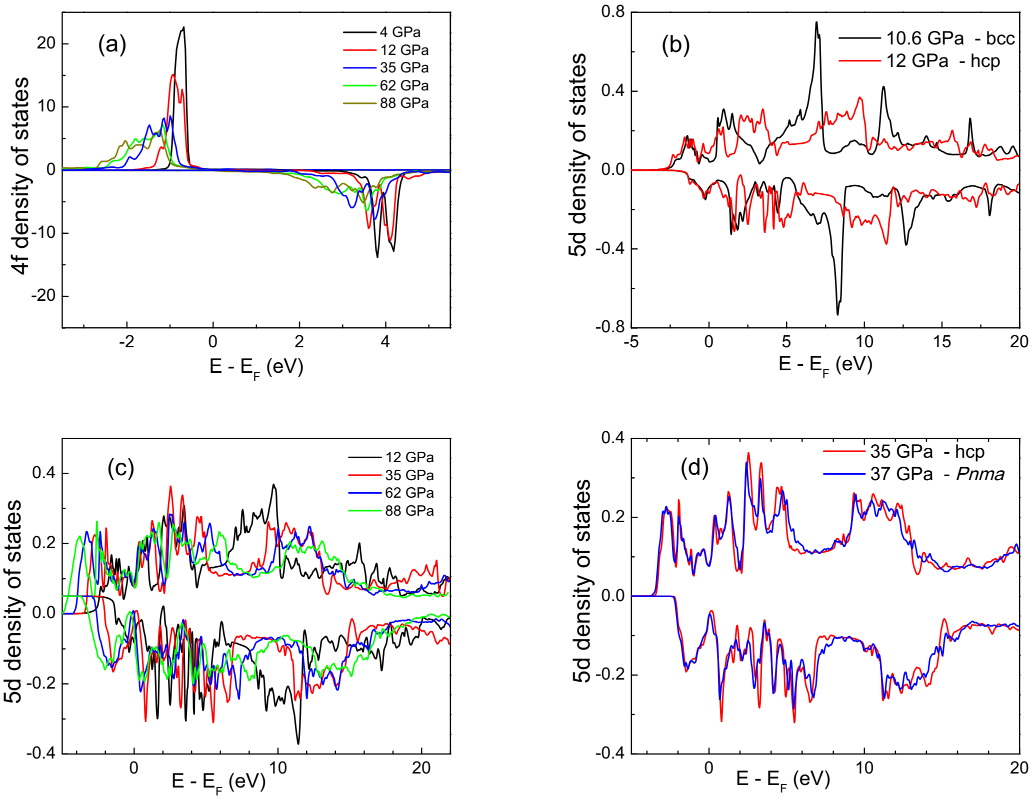

Figure 4.17: Simulated density of state for $4f$ (a) and $5d$ (b, c, d). See text for detailed discussion.

4*f* electron occupancy below 20 GPa the total magnetic moment shows an anomaly around 12 GPa and then decreases at higher pressure.

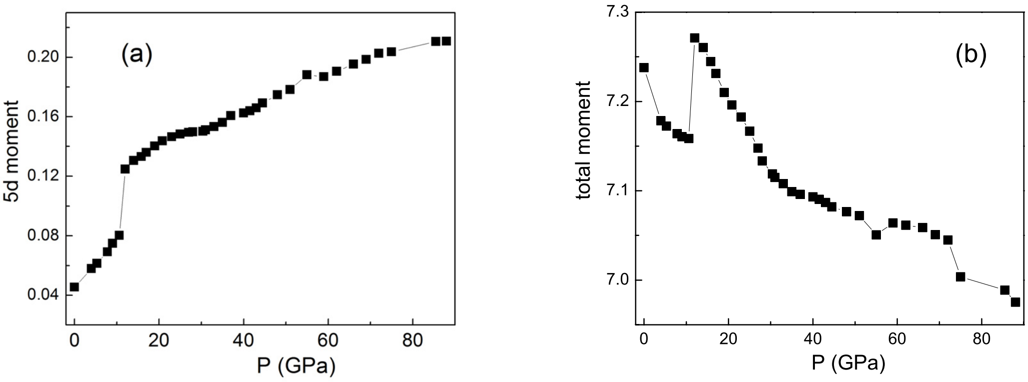

Figure 4.18: Simulated $5d$ (a) and total (b) magnetic moment of Eu in the ferromagnetic ground state.

To confirm the results from the above simulations that the changes in XANES spectra originate from changes in structure instead of valence, high pressure ab-inito XANES simulations were carried out by D. Haskel treating the $4f$ electrons as core electrons and using the atomic structure information from the x-ray diffraction experiment. Figure 4.19 shows the simulated XANES spectra up to 75 GPa. In the bcc phase, the spectral lineshape does not change much except the resonant peak intensity is strongly suppressed under pressure. However, at the bcc-hcp phase transition, the resonant peak becomes broadened and a second peak appears and shifts to higher energy with increasing pressure. The lineshape does not change much beyond the hcp phase to 75 GPa. The electron occupancy changes in s, p, d states from the calculations are shown in Figure 4.20. Similar to the results from DFT-XANES simulations (Figure 4.16), $5d$ electron occupancy increases by 1 from ambient pressure to 70 GPa.

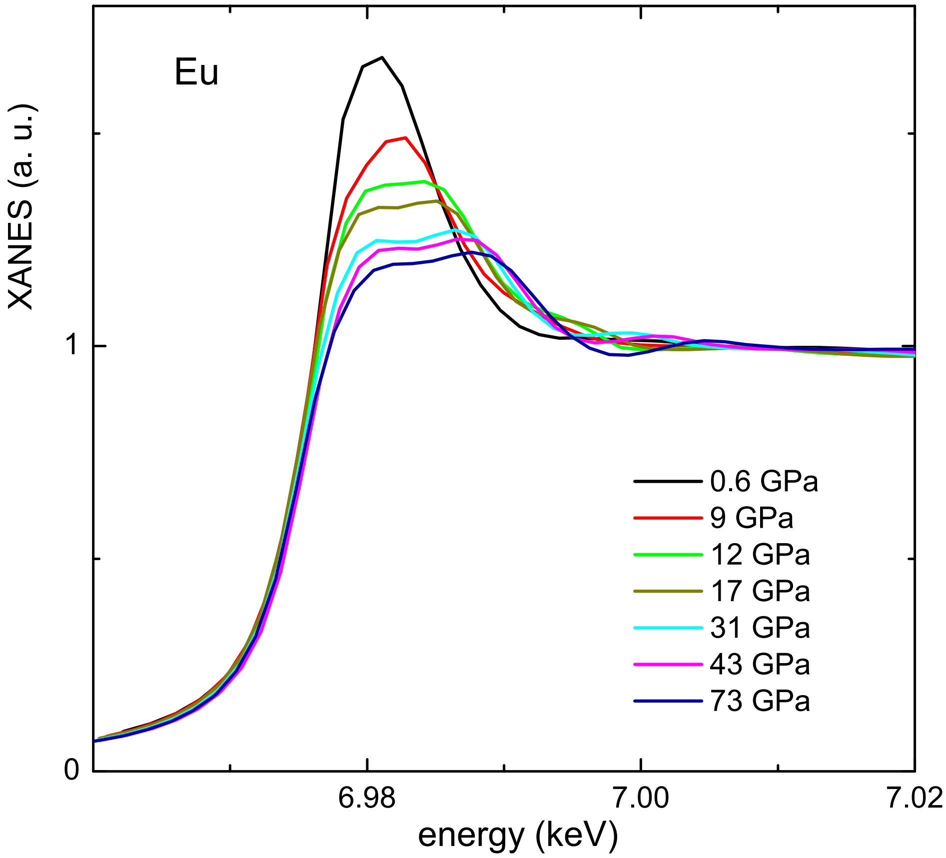

Figure 4.19: Ab-initio simulations of XANES under pressures up to 75 GPa.

This extra charge appears to come from the s and p electrons. This *s*-*p*-*d* hybridization resulting in charge transfer from s and p to d orbitals seems to be the cause for the strong suppression of the XANES resonant intensity in bcc phase (Figure 4.19), where the 5d electron occupancy increases drastically below 12 GPa .

In summary, the room temperature XANES experiment on Eu does not give evidence for a valence transition toward trivalency under pressures up to 87 GPa. The DFT-XANES simulations show that the XANES spectra change is structural in origin

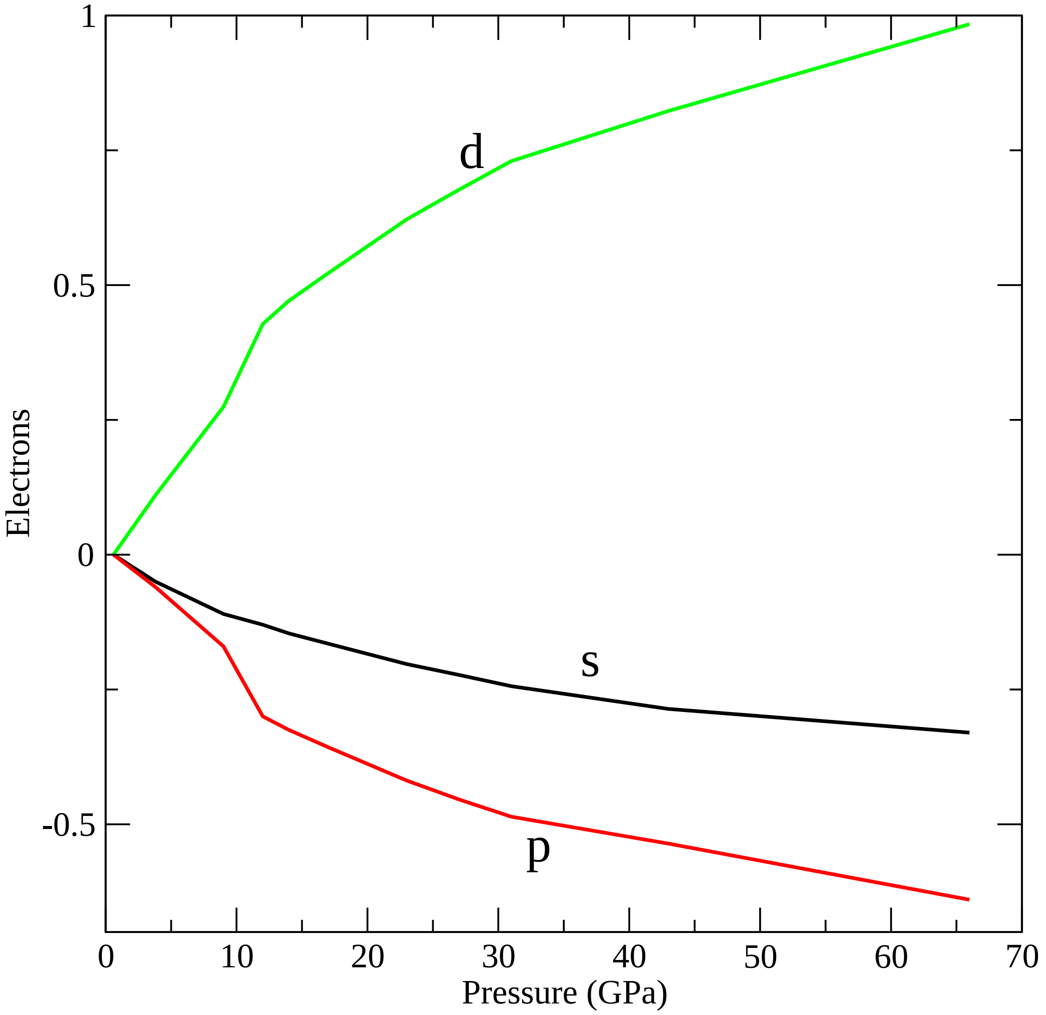

Figure 4.20: Electron occupancy change in *s, p, d* orbitals from ab-initio simulations.

with a small change of $4f$ electron occupancy (0.14) around 20 GPa, contrary to the previous reports [48, 49, 127] that Eu's valence increases under pressure to $\sim$ 2.5 at 12 GPa and saturates at 2.64 above 24 GPa. Further ab-initio simulations treating $4f$ electrons as core electrons confirm that Eu's crystal structure alone could explain the spectra change under pressure.

4.2.2 XMCD Experiment

To further explore possible changes in the valence state of Eu under pressure, we studied the magnetism of Eu under pressures as high as 60 GPa through XMCD experiments carried out at beamline 4ID-D under the proposal GUP-21527 with the help of Dr. N. Souza-Neto, Dr. D. Haskel and G. Fabbris. The canted magnetic moment of Eu was measured at the base temperature $\sim$ 4.6 K with a continuous flow cryostat and 4 T superconducting magnetic field. In order to fit in the superconducting magnet bore, a piston-cylinder miniDAC (Figure 3.18(c)) with a 16 mm outer diameter from D'ANVILS was used. The x-ray beam was focused to $\sim$ 12 μm using a KB mirror at the sample position. Similar to the XANES experiment, to reduce x-ray absorption by the diamond at the L_{III} edge energy 6.97 keV, a partially perforated anvil and a full anvil (Figure 3.10) with a 300 μm culet were used to achieve high pressures up to 60 GPa. The Re gasket was preindented to 60 μm and a circular hole of 120 μm diameter was EDM drilled or laser drilled at GSECARS, sector 13. The Eu sample was loaded in an Ar-filled glovebox with oxygen level $\sim$20 ppm located at sector 3. Pressure was measured from ruby fluorescence at room temperature. Each pressure was measured twice, before and after cooling to low temperature and warming to room temperature. The pressure change in the cell after cooling was less than 3 GPa.

At each pressure, the cell was first rotated to minimize the Bragg peaks from the diamond in the measured energy range of 6.94 keV to 7 keV at room temperature. Then it was cooled to the base temperature of 4.6 K. A 4 T magnetic field was then applied at 4.6 K. After measuring the XMCD spectra, the field was switched to -4 T. At each field direction, at least two scans were collected and averaged. To take into account thickness change under pressure, the XMCD amplitude is normalized by the XANES edge jump at the same pressure. XMCD data taken with opposite applied field directions (+/- 4 T) were substracted and divided by two to yield aritifact-free XMCD signals.

XANES and XMCD spectra were measured at 3.3, 7.1, 10.3, 15, 21.4, 30.7, 40, 49.1 and 59.4 GPa. The low temperature XANES data agree well with the ones measured previously at room temperature (Section 4.2.1). Two examples of the XANES and XMCD signals are shown in Figure 4.21 at 3.3 and 21.4 GPa.

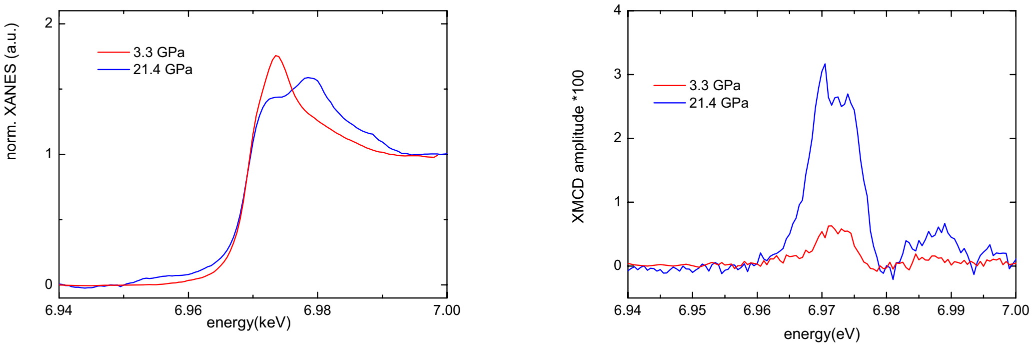

Figure 4.21: Normalized XANES spectra (left) and XMCD amplitude (right) at 3.3 GPa and 21.4 GPa.

The XMCD amplitude versus pressure is plotted in Figure 4.22 up to 60 GPa. The pressure uncertainty in the plot is from the pressure change before and after cooling. The uncertainty in the XMCD signal is from the standard deviation of the XMCD amplitude from different scans. The canted magnetism stays almost constant in the bcc phase below 12 GPa. At higher pressure, the magnetism first increases drastically up to 21.5 GPa and then drops down. This increase in magnetism with pressure to 21.5 GPa indicates that Eu is certainly not in the trivalent state in this pressure range. The change of magnetism under pressure to 60 GPa is similar to the simulated total magnetic moment change under pressure shown in Figure 4.18, suggesting the magnetism change in Eu may come from the pressure-induced structural transition. As discussed in Section 4.1.3, the slope change of the c/a ratio above 18 GPa may signal a magnetic transition (Figure 4.7) which was observed in Fe, MN_y (M = Mn, Fe, Ni) [167,168].

As seen in Figure 4.22, the XMCD amplitude reaches values as high as 2.6% near 21 GPa which is comparable to the XMCD amplitude of ∼3.3% from pure Eu^{2+} ferromagnetism in EuO when the ferromagnetism is saturated at 2 T field and 9 K. The amplitude at 21 GPa is much larger than the XMCD amplitude (∼0.13%) in Van Vleck paramagnetism in Eu_2O_3 measured at 4 T and 9 K [175]. The absence of the quadrupole signature of Eu^{3+} in the XMCD spectra gives strong evidence that Eu is not trivalent at the highest measured pressure 59.4 GPa [175].

The field dependence of the raw XMCD amplitude (before normalized by the edge jump) was measured for the foil sample from -4 T to 4 T, at ambient pressure, a

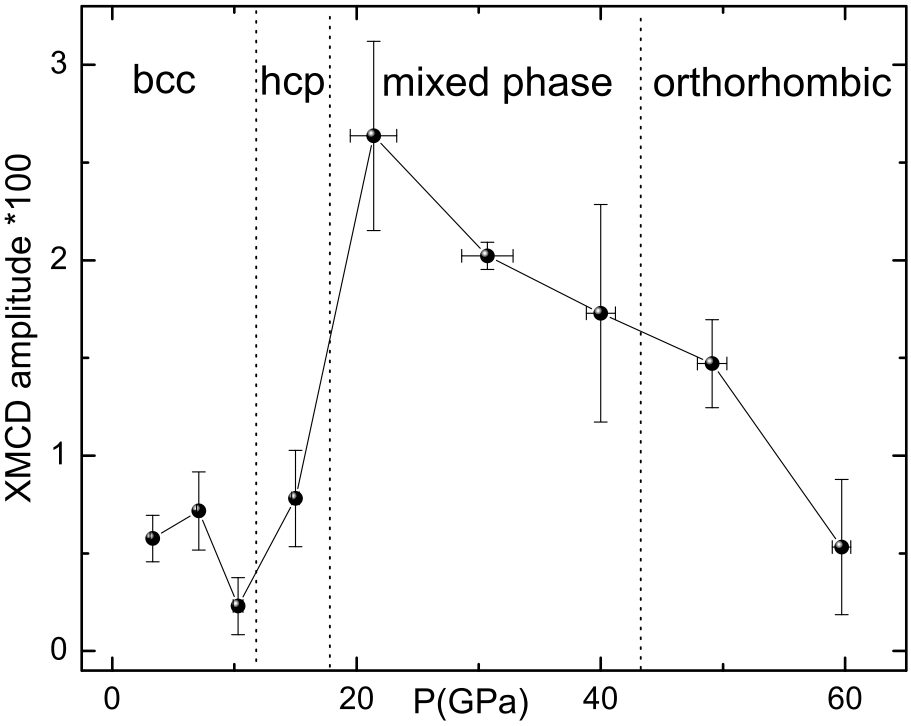

Figure 4.22: XMCD amplitude of Eu under pressure up to 60 GPa.

temperature of 4.6 K, and at the resonant energy of 6.972 keV, which corresponds to the maximum XMCD amplitude (Figure 4.23 (a)). The field dependence of the sample in the DAC was also measured at pressures of 3.3, 21.4, 30.7 and 49.1 GPa (Figure 4.23(b-e)). At ambient pressure, the XMCD-field dependence is linear as expected for field-induced canting of Eu's antiferromagnetic state. At 3.3 GPa the XMCD-field dependence is almost linear. But the data are very noisy since the photon flux is attenuated greatly by the diamond window in the DAC. At 21.4, 30.7 and 49.1 GPa it is clear that the field dependence shows saturation above 2 T, suggesting that the sample shows a ferromagnetic-like behavior.

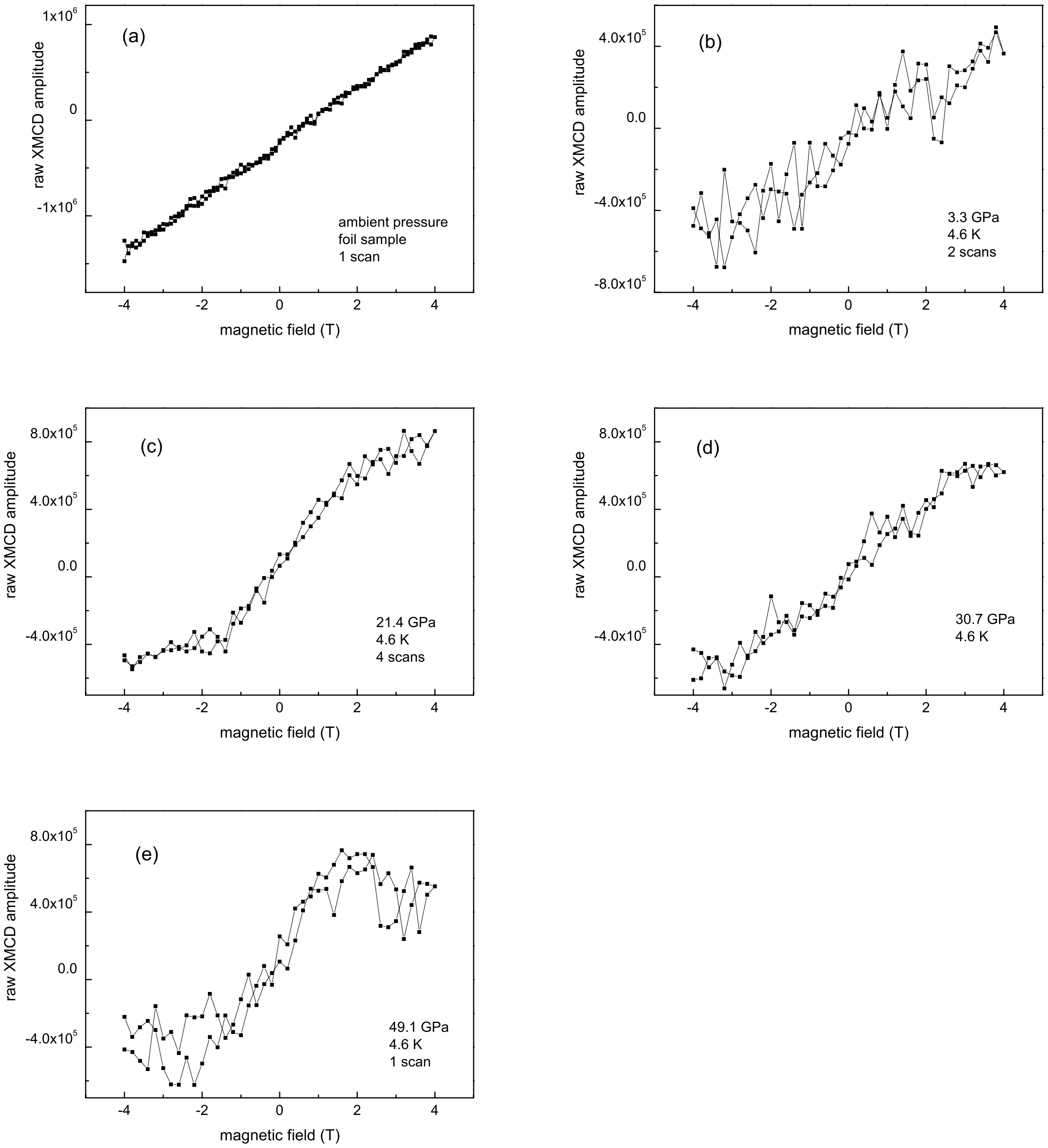

Figure 4.23: Magnetic field dependence of the XMCD amplitude at 4.6 K at ambient pressure (foil sample), 3.3 GPa, 21.4 GPa, 30.7 GPa and 49.1 GPa in DAC.

It would be very interesting to extend these measurements to higher pressures, especially above 80 GPa in the superconducting pressure range, to learn how the XMCD amplitude behaves above 60 GPa. Unfortunately, after the measurement at 59.4 GPa, we ran out of beam time and the experiment had to be stopped.

4.2.3 SMS Experiment

Three runs of SMS experiments on ^{151}Eu were carried out at room temperature at the beamline 3-ID, APS in collaboration with Dr. E. Alp and Dr. J. Zhao. In all three runs, diamond anvils with a 180 μm culet beveled at 7° out to 350 μm were mounted onto the WC plates in the symmetric cell. Ruby spheres with a 5-10 μm diameter and a small amount of Pt powder were loaded together with the sample in the Re gasket hole (~85 μm) for pressure measurement. With Pt as a pressure marker, we were able to measure in-situ powder diffraction on Pt at the resonant energy 21.5 keV. In addition, the diffraction patterns from the Eu sample were also collected simultaneously to double check the pressure by comparing the Eu diffraction peak positions from the previous x-ray diffraction measurements. The in-situ pressure measurement also allowed accurate pressure determination at the same sample position where the SMS was measured. The x-ray beam was focused to ~10 μm in both horizontal and vertical directions through a KB mirror.

To be able to measure in-situ diffraction for pressure determination, the WC backing plate located in the x-ray exiting side must have a big enough aperture to collect at least two diffraction peaks from Pt at the highest pressure. In fact, in the experiments on the x-ray incident side a WC backing plate with a 1 mm diameter hole was used, and on the exiting side (facing the image plate which collected the diffraction patterns) a backing plate with a 1.6 mm diameter hole was used. Both plates had a conical hole with 50° full angle. With a 1.0 mm hole, a 50° full angle, and a 2 mm high diamond anvil, the maximum 2θ angle for x-ray diffraction is only ~14° $\left(\arctan\left(\frac{1mm/2}{2mm}\right)\right)$, which is not high enough to observe 2 diffraction peaks from Pt. If a 1.6 mm hole is used, a maximum 2θ angle of ~22° $\left(\arctan(\frac{1.6mm/2}{2mm})\right)$ can be achieved and the first two (111) and (200) diffraction peaks from Pt can be observed up to at least 1 Mbar of pressure.

For all three experimental runs, the sample was loaded inside the Ar filled glovebox with an oxygen level lower than 0.2 ppm in our lab at Washington University one day before the experiments at APS. The pressure cell has to be loaded with a little pressure in order to seal the sample to avoid being oxidized during transportation to APS, and the initial pressure applied should not be too high, preferable a few GPa. To ensure this, the pressure was measured using ruby fluorescence after the sample loading.

SMS Experiment 1

In the first run of the experiment, G. Fabbris collected the data at beamline 3-ID, APS in August 2010. During this run, pressure was determined from the ruby fluorescence since the diffraction peaks from Pt were not observed at the sample position measured by the SMS. The pressure was increased manually by tightening the 4 screws in the symmetric cell. The Mössbauer spectra were measured at 4, 9, 12, 14, 17 and 25 GPa. In each of the measurements, the Mössbauer spectrum with the reference and the Eu sample was first measured. Then the reference was removed and the diffraction of the

Eu sample was measured without moving the Eu sample position.

At low pressures, Eu_2O_3 with an isomer shift of 1.024 mm/sec served as the reference. However, under pressure the isomer shift of the ^{151}Eu increased from the ambient pressure value -7.33 mm/sec [127] and came close to the reference, which gives less quantum beats in the SMS spectra (Figure 4.24) and makes it difficult to fit the data and get the isomer shift. Therefore, at 25 GPa EuS was used as the reference. The isomer shift of the sample is farther away from the EuS reference -11.496 mm/sec, so more beats were observed on the same time scale. Figure 4.24 is a plot of the SMS (in the left column) and the corresponding spectra in the energy domain (in the right column). The data were fitted in CONUSS software described in section 3.1.4.

When further pressure was applied after 25 GPa, 54, 64 and 90 GPa were also measured from ruby fluorescence. However, based on the Eu diffraction data collected after the SMS measurements, the pressures were lower than 25 GPa, i.e. pressure did not increase, but decreased instead. It is possible that mistakes were made when the ruby fluorescence was measured.

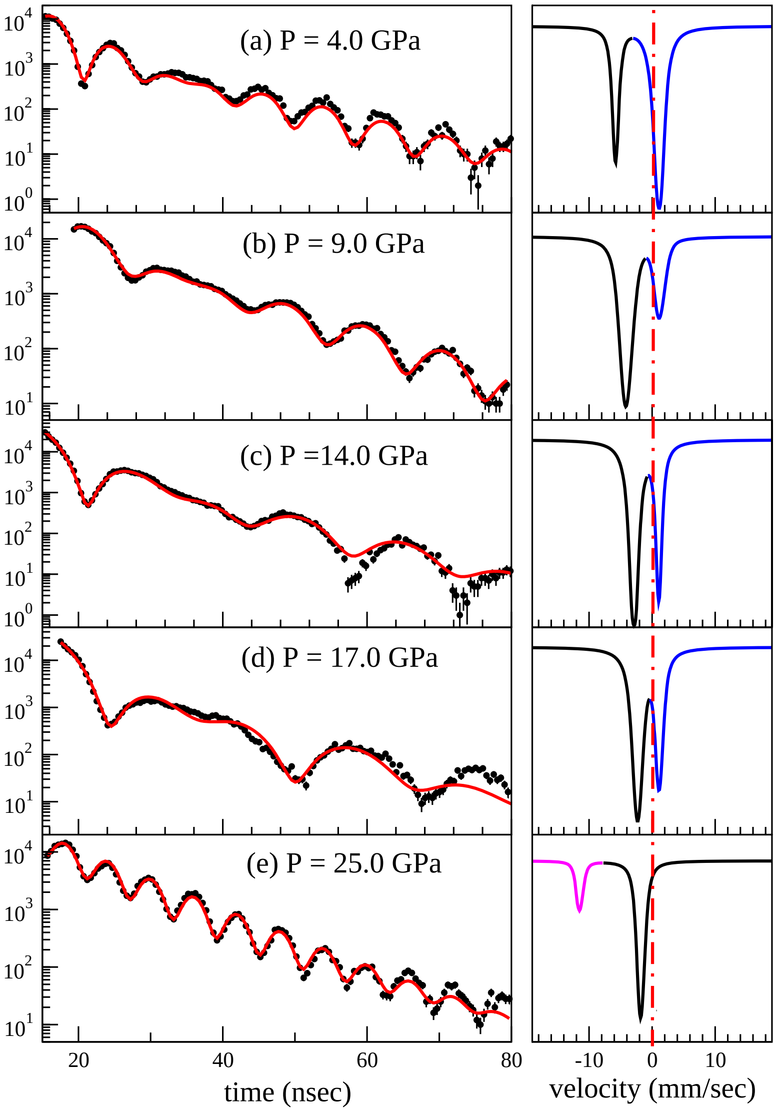

Figure 4.24: Mössbauer spectra of ^{151}Eu under pressure to 25 GPa in time domain (left column) and in the corresponding energy domain (right column) in experimental run 1. In the left column plot, the black solid circle shows the experimental data with error bar and the red line shows the fit to the data. The red dash-dot line in the right column plot indicates the position of the zero isomer shift. In the right column plot the black line shows the resonant absorption from Eu sample, the line in blue color shows the absorption from Eu_2O_3 as the reference, and the purple line is from EuS as the reference.

SMS Experiments 2 and 3

Experimental runs 2 and 3 were carried out in December 2011 with the help of Dr. Y. Meng from HPCAT, Dr. E. Alp and Dr. J. Zhao from 3-ID, APS under GUP-23381. During runs 2 and 3, a gearbox designed for applying pressure to the symmetric cell was used. With two symmetric cells prepared and samples loaded, we were able to measure two runs within 3 days of beam time. During the experiments the pressure was determined from the first two diffraction peaks of Pt based on its equation of state under pressure [126]. Each pressure was measured right after the pressure was applied through the gearbox, as well as after the measurement of the Mössbauer spectrum (~3 hours or more). Since it normally took some time for the pressure to be stabilized through the gearbox, the pressure measured after the Mössbauer measurement was 1-2 GPa higher than the one measured right after pressure was applied. The pressure was determined by comparing the measured diffraction peak positions of Pt with the peak positions from its equation of state [126] under pressure using Xray_helper software. EuS was used as the reference for all the pressures.

During run 2, Mössbauer spectra at 12, 19.3, 23.4, 28.6, 35.3 GPa were measured. Figure 4.23 shows the spectra in both the time and energy domains. Under pressure, the sample became thinner and thinner which resulted in decreasing contrast in the quantum beats in the time domain spectra. When the sample becomes too thin relative to the reference, the measured spectrum shows mainly the exponential decay from the reference EuS, which is a straight line in a logarithmic scale. It is then difficult to fit the spectra and extract the isomer shift of the sample accurately. Therefore, we had to stop the measurement in this cell. Since the Eu sample thickness decreases under pressure, a reference material with a continuously varying thickness in one direction is preferred, so that when the sample thickness decreases under pressure, the reference can be moved to a thinner part to keep a good thickness contrast.

In run 3, Mössbauer spectra at 23.1, 45.2, 52.35, 57.95, 65.5 and 72.6 GPa were measured. Unfortunately, one diamond failed when further pressure was applied through the gearbox after the measurement at 72.6 GPa. The spectra at different pressures are plotted in Figure 4.25. Above 23.1 GPa, starting from 40 nsec, the separation of the beats becomes unequal which makes the fitting more difficult than at lower pressures. Since in this pressure range the structure of Eu is in a mixed phase, an additional ^{151}Eu site for the sample was added in an attempt to fit the data. However, after the refinement the second Eu site always took on the same isomer shift as the first Eu site from the sample, which showed that the second site was not necessary in this case. There may be some unknown weak effect developed under pressure in the Eu sample that we failed to take into account. But for the purpose of extracting the isomer shift, the fits to the experimental spectra are adequate.

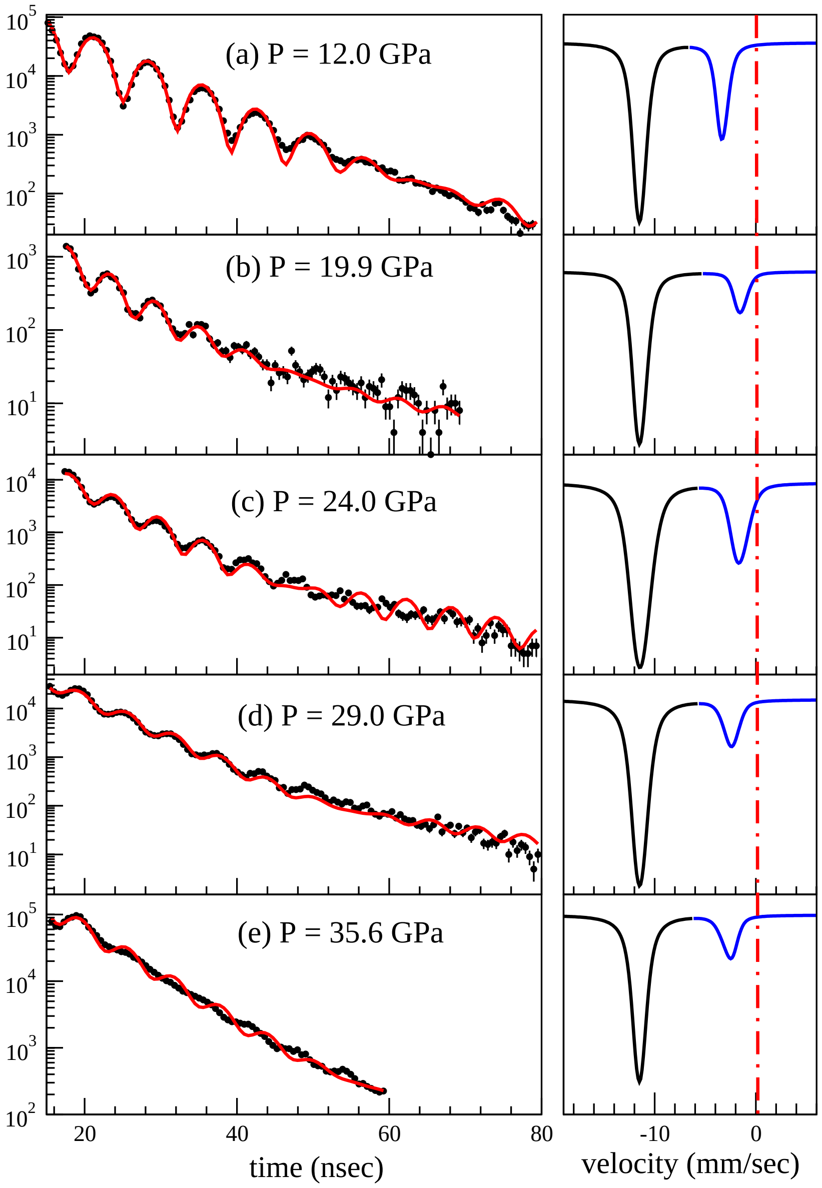

Figure 4.25: SMS experiment run 2 on Eu metal. Mössbauer spectra of ^{151}Eu under pressures up to 35.6 GPa in time domain (left column) and in the corresponding energy domain (right column). In the left column plot, the black solid circle shows the experimental data with error bar and the red line shows the fit to the data. The red dash-dot line in the plot on the right indicates the position of the zero isomer shift. In the right column plot the black line shows the resonant absorption from the Eu sample, the line in blue color shows the absorption from EuS as the reference.

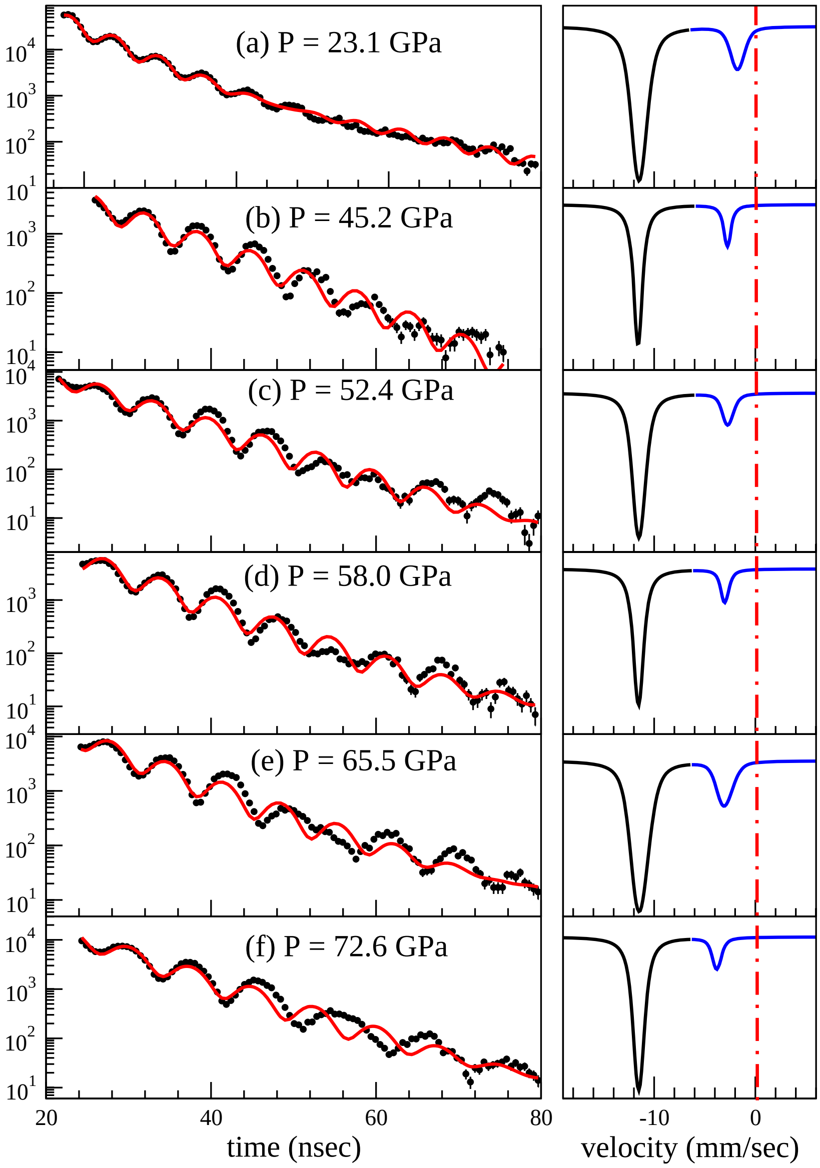

Figure 4.26: SMS experiment run 3 on Eu metal. Mössbauer spectra of ^{151}Eu under pressure to 72.6 GPa in time domain (left column) and in the corresponding energy domain (right column). In the left column plot, the black solid circle shows the experimental data with error bar and the red line shows the fit to the data. The red dash-dot line in the plot on the right indicates the position of the zero isomer shift. In the right column plot the black line shows the resonant absorption from the Eu sample, the line in blue color shows the absorption from EuS as the reference.

The isomer shift of ^{151}Eu under pressure is shown in Figure 4.27. Our experimental data at ambient temperature agree well with the previous studies by Farrell and Taylor at 44 K to 12 GPa [127] and Wortmann *et al.* at ambient temperature to 22 GPa [49]. The application of 20 GPa pressure causes the isomer shift to increase rapidly by almost 6 mm/sec. Between 25 and 30 GPa the isomer shift decreases suddenly and at higher pressures it decreases at a slower rate up to 73 GPa.

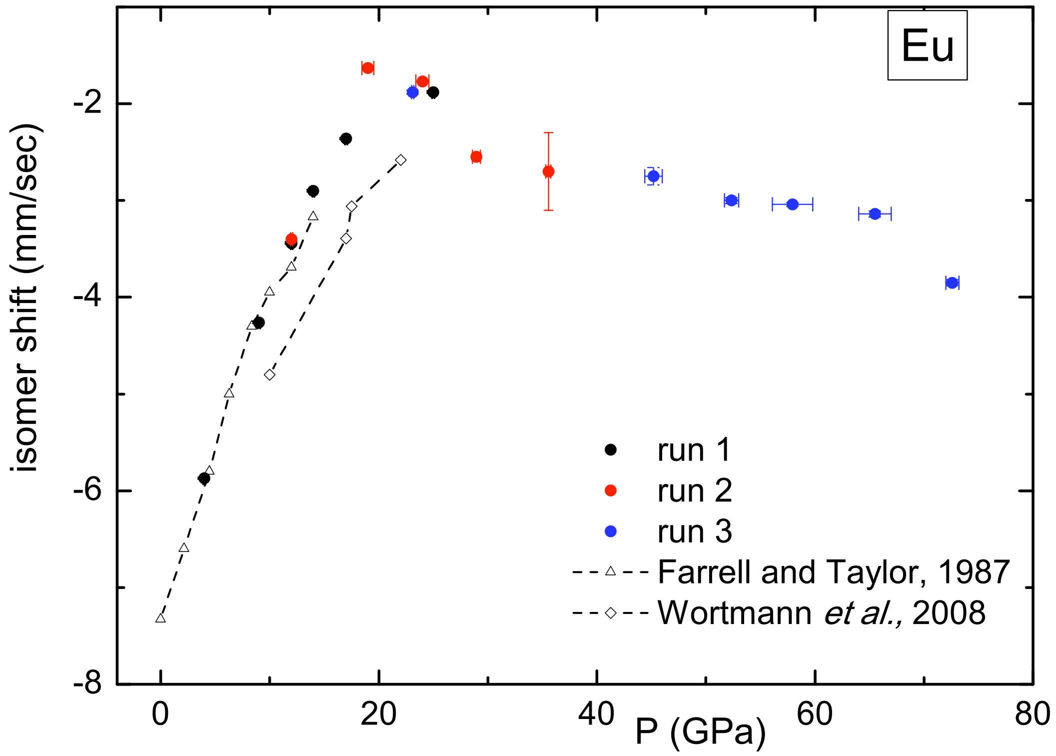

Figure 4.27: Isomer shift of ^{151}Eu under pressure up to 73 GPa in comparison with the previous studies by Farrell and Taylor at 44 K [127] and Wortmann *et al.* at room temperature [49]. The error on the pressure is determined from the deviation of pressure measured before and after Mössbauer measurement. The error on the isomer shift is from the refinement uncertainty obtained from fitting the data in CONUSS.

When Eu is in a mixed-valent state, the isomer shift is expected to show a strong temperature dependence [128,198]. It is noticed in Figure 4.27 that our data taken at room temperature agree well with the data taken at 44 K by Farrell and Taylor, and the isomer shift does not show any temperature dependence which may indicates Eu's valence is not 2.5 at $\sim$ 12 GPa as reported in [48,49,127]. However, the low temperature experiment was done with CMS and our experiment with SMS. The different experiment appratus and variation of the sample may cause some change in isomer shift.

In References [49,127] Eu's valence under pressure was obtained simply from linear extrapolation of the 12.52 mm/sec isomer shift from Eu^{2+} to Eu^{3+} at ambient pressure, thus treating the valence change as the only factor determining the isomer shift under pressure. The extrapolated valence reported in [49,127] increases drastically in the bcc phase, and the values of valence under pressure are in agreement with Röhler's analysis of his XANES measurements [48]. However, the Mössbauer data interpretation ignores the isomer shift caused by pressure-induced changes in the electronic structure. The measured isomer-shift change under pressure may not come from the valence change ($4f^7 \rightarrow 4f^6$) at all. If the change in isomer shift were from the valence change, it would be expected to increase monotonically under pressure. From the x-ray diffraction experiments, Eu enters from bcc to hcp phase at 12 GPa, then a mixed phase above 18 GPa, and finally an orthorhombic phase above 66 GPa after going through a sluggish phase transition between 18 and 66 GPa. The slope change in $\frac{dIS}{dP}$ near 20 GPa may be related to the pressure-induced phase transition. Suggested by the DFT-XANES simulations shown in Figure 4.17, the pressure-induced isomer shift may also be due to variation in the occupation of the *s, p, d* conduction electron states, instead of the valence change. To clarify these issues, theoretical simulations on isomer shift under pressures are in progress.

Another way to resolve this valence controversy would be to carry out low temperature Mössbauer experiments on Eu metal under pressures to 1 Mbar. By measuring the isomer shift at several temperatures on our Eu sample, we will get a clear answer whether the isomer shift shows a large temperature dependence or not. In addition, we will take advantage of SMS's high sensitivity to any type of magnetic ordering and study the high-pressure magnetic ordering of Eu at low temperature. The experiment planned for later this year should provide a definitive answer regarding the valence state of Eu and related presence/absence of magnetic ordering in the normal and superconducting state, and will shed light on why the superconducting temperatures are an order of magnitude lower than for the trivalent d-electron metals.

4.3 He-Gas High-Pressure Studies on Superconducting $LaO_{1-x}F_xFeAs$

The results presented in this section were published in Reference [195] and a good portion of this section is taken from this paper.

The discovery of superconductivity at temperatures as high as 26 K in $LaO_{1-x}F_xFeAs$ [51] has rekindled the interest in high-temperature superconductivity. As for the cuprates, high-pressure experiments can potentially play an important tole in furthering our understanding of the new Fe-based pnictides. High pressure experiments to 30 GPa by Takahashi *et al.* [176] on this compound for $x = 0.11$ using a NaCl pressure medium reveal that the superconducting onset in electrical resistivity reaches temperature as high as 46 K. The initial slope $\mathrm{d}T_c/\mathrm{d}P$ studies by several groups [8, 52, 176, 178, 179] using various fluid pressure media agree that $\mathrm{d}T_c/\mathrm{d}P$ is positive initially, but differs widely in its magnitude. As in the previous studies on the high-T_c cuprates [177] and the binary compound MgB_2 [180], it would be of interest to carry out benchmark determinations of $T_c(P)$ in magnetic susceptibility measurements on $LaO_{1-x}F_xFeAs$ using the most hydrostatic pressure medium known, He gas.

One notable result is that the non-superconducting, undoped pnictides LaOFeAs [176], $CaFe_2As_2$ [181], $SrFe_2As_2$ [182] and $BaFe_2As_2$ [182] reportedly become superconducting under pressure when pressure media such as Fluorinert, methanol-ethanol and silicone oil were used, superconductivity in $CaFe_2As_2$ appearing at a relatively low pressure $\leq$0.4 GPa. However, later dc susceptibility and electrical resistivity measurements by Yu *et al.* [183] on $CaFe_2As_2$ using He-gas pressure media fail to detect any sign of superconductivity to 0.7 GPa and 2 K. These authors suggest that not only in $CaFe_2As_2$, but also in $SrFe_2As_2$ and $BaFe_2As_2$, nonhydrostatic stress components may have been responsible for the reported pressure-induced superconductivity. In addition, very recently Matsubayashi *et al.* [184] carried out parallel ac susceptibility and electrical resistivity measurements on $BaFe_2As_2$ and $SrFe_2As_2$ single crystals to 8 GPa pressure in a relatively hydrostatic cubic anvil pressure apparatus and found no trace of superconductivity in the former compound; in $SrFe_2As_2$, bulk superconductivity, as evidenced by full shielding in ac susceptibility, is only found in a rather narrow (2 GPa) pressure region centered about 6 GPa, where non-bulk (filamentary) superconductivity is revealed in the resistivity that falls to zero over a much wider pressure region. Extensive mechanical deformation studies on $SrFe_2As_2$ single crystals indicate that internal strains originating from c-axis-oriented planar defects plays a central role in the appearance of superconductivity at ambient pressure [185]. The potentially important role that shear stresses play in the superconductivity of Fe-based pnictides is emphasized in the recent review of Chu and Lorenz [6]. Indeed, shear-stress effects on $T_c(P)$ are well known from studies on diverse superconducting materials such as organic metals [186], high-T_c oxides [177], MgB_2 [180] and Re metal [187].

To our knowledge, the measurements of Yu *et al.* [183] on $CaFe_2As_2$ are the only He-gas high-pressure studies of superconductivity carried out to date on an Fe-based pnictides. It would be of obvious interest to extend such studies to the $LaO_{1-x}F_xFeAs$ system to ascertain whether $T_c(P)$ differs from the findings of earlier studies, where less hydrostatic pressure media were employed. Using He as the pressure medium brings a further benefit: it allows one to change the hydrostatic pressure at relatively low temperatures and temperature dependent. An example of such phenomena in the cuprates is the well-known oxygen ordering effect, which has been shown in some systems to be the dominant factor determining the dependence of T_c on pressure [177].

To throw some light on these issues, we have determined $T_c(P)$ using He-gas pressure medium to 0.78 GPa for the original Fe-based superconducting pnictide, $\mathrm{LaO_{1\text{-}x}F_xFeAs}$, where $x = 0.07$ and 0.14. For these doping levels we find the initial pressure derivative $\mathrm{d}T_c(P)/\mathrm{d}P$ to be positive, but markedly less than the published values using other pressure media; in addition, the dependence of T_c on pressure is not reversible but depends on the detailed pressure/temperature history of the sample. Possible origins for this behavior are discussed in the following.

4.3.1 Experiment

Polycrystalline $\mathrm{LaO_{1\text{-}x}F_xFeAs}$ samples are prepared by solid-state reaction as described in previous publications [51, 52]. For $x = 0.14$ both the previous resistivity measurements [176] and the present ac susceptibility studies are carried out on pieces taken from the same mother sample. The fluorine content in the present samples, $x = 0.07$ and $x = 0.14$, is determined from the lattice constant using Vegard's law: these samples have densities 6.704 and 6.739 g $\mathrm{cm^{-3}}$ [51] and masses 1.54 and 8.69 mg (or 5.65 mg), respectively.

The hydrostatic pressures as high as 0.8 GPa was generated using the He-gas compressor system. The two-stage closed cycle refrigerator was used to cool the pressure cell to temperatures as low as 506 K; measurements were carried out on warming up slowly through the transition at the rate ~0.3 K min^{-1}. All susceptibility measurements were repeated at least once to verify that the reproducibility of the transition temperature was within 20 mK. Unless otherwise stated, the sample was cooled down to measure T_c 30-60 min after a given change in pressure/temperature.

4.3.2 Experimental Results

4.3.2.1 $\mathbf{LaO_{0.93}F_{0.07}FeAs}$ sample

For the $x = 0.07$ sample at ambient pressure, the 80-20 transition width in ac susceptibility is ~1 K, where $T_c \simeq 21$ K from the midpoint. These values of T_c are several degree kelvin less than those estimated from the resistivity onset at comparable fluorine concentrations [176].

Previous high-pressure resistivity measurements with Fluorinert pressure medium on $\mathrm{LaO_{1\text{-}x}F_{\mathit{x}}FeAs}$ for $x = 0.05$, 0.08 and 0.11 yielded the following positive values of the initial derivative $\mathrm{d}T_c(P)/\mathrm{d}P \simeq 2$, 2 and 8 K/GPa respectively, where T_c was determined from the resistivity onset. From these results, one would anticipate that $\mathrm{d}T_c(P)/\mathrm{d}P \simeq 2$ K/GPa for $x = 0.07$. On the other hand, if T_c is determined from the temperature at which the resistivity ρ drops to 0, one finds for $x = 0.08$ the initial pressure dependence $\mathrm{d}T_c(P)/\mathrm{d}P \simeq 0.54$ K/GPa, a value approximately 4× smaller than that from the resistivity onset (for $x = 0.05$ and 0.11, it was not possible to reliably estimate the temperature at which $\rho \to 0$. In resistivity measurements, therefore, the value of $\mathrm{d}T_c(P)/\mathrm{d}P$ obtained evidently depends on the criterion used to determine T_c.

We now compare the values of $\mathrm{d}T_c(P)/\mathrm{d}P$ obtained from the present ac susceptibility measurements using hydrostatic He-gas pressure on $\mathrm{LaO}_{1\text{-x}}\mathrm{F}_x\mathrm{FeAs}$ with those obtained in the above resistivity studies. Figure 4.28 shows our results for the F concentration $x = 0.07$. The large magnitude of the superconducting transition is consistent with bulk superconductivity; in fact, the shielding effect is approximately twice that expected for perfect diamagnetism. No correction is made here for diamagnetization effects. Under increasing He-gas pressure to 0.78 GPa, the superconducting transition is seen to shift monotonically to higher temperatures. Here T_c is defined by the transition midpoint (see Figure 4.28); however, since the shape of $\chi'(T)$ of the transition does not change with pressure, the shift in T_c with pressure is the same irrespective of whether T_c is defined from the transition midpoint or onset.

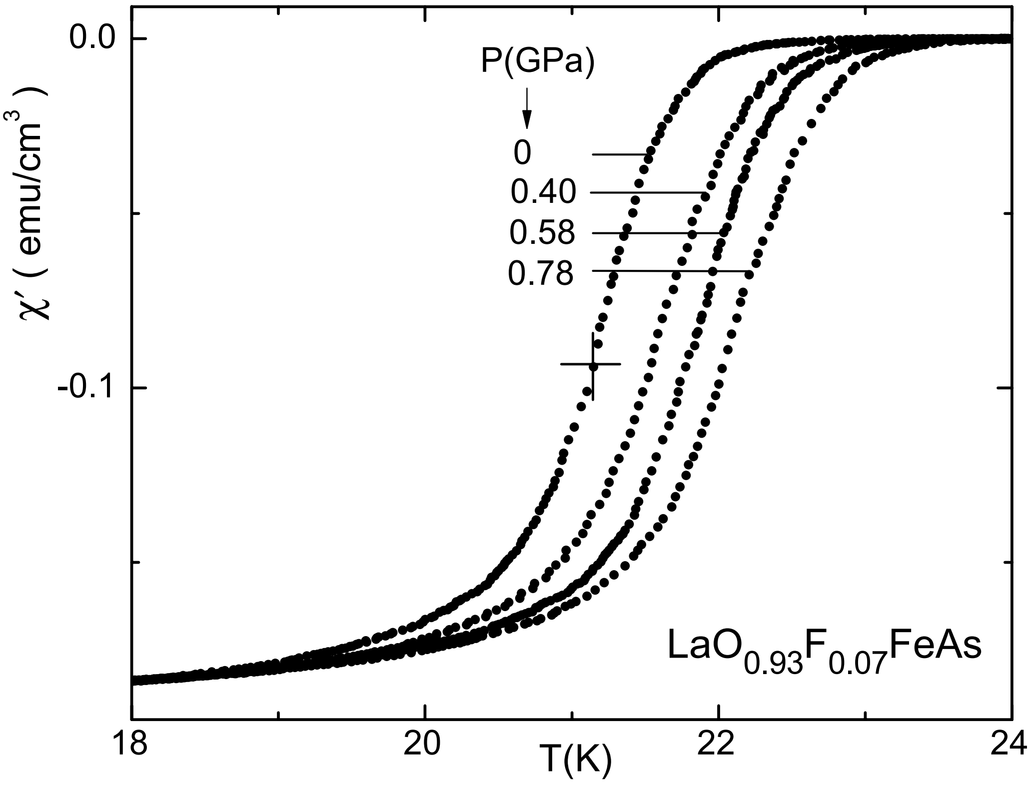

Figure 4.28: Real part of the ac susceptibility versus temperature of LaO$_{0.93}$F$_{0.07}$FeAs sample (mass 1.54 mg) at four selected He-gas pressures. Order of measurement given by pressure values from top to bottom. Large cross (+) marks midpoint of superconducting transition for initial measurement at ambient pressure (0 GPa).

In Figure 4.29 the dependence of T_c on pressure is shown for all measurements on the $x = 0.07$ sample, the numbers giving the order of measurement. After the ambient measurement (point 1), 0.78 GPa pressure is applied at room temperature (RT) to yield point 2. T_c is seen to increase under pressure at the rate +1.20 K/GPa, clearly less than the value +2 K/GPa inferred from the resistivity onset but great than the value using the $\rho \rightarrow 0$ criterion at nearly the same F concentration ($x = 0.08$); in the resistivity studies, the pressure was always changed at RT. The pressure was then successively reduced at low temperatures (62, 52 and 45 K for points 2$\rightarrow$ 3, 3 $\rightarrow$ 4 and 4 $\rightarrow$ 5, respectively) before cooling down further to measure T_c. Up to and including point 4, the $T_c(P)$ dependence is reversible; however, at ambient pressure (point 5) T_c lies $\sim$220 mK lower than the initial value at ambient pressure (point 1). Interestingly, after warming the sample back to RT and holding for 1.5 h, T_c is seen to revert (point 6) to its initial value. This behavior bears some resemblance to that observed previously from oxygen-ordering effects in the cuprates, where $T_c(P)$ may differ strongly depending on whether the pressure is changed at RT or low temperatures [177]; there is, however, one notable difference - when pressure is reduced at low temperature in a cuprate with oxygen ordering, all values of T_c would differ, and not just those below a certain pressure threshold.

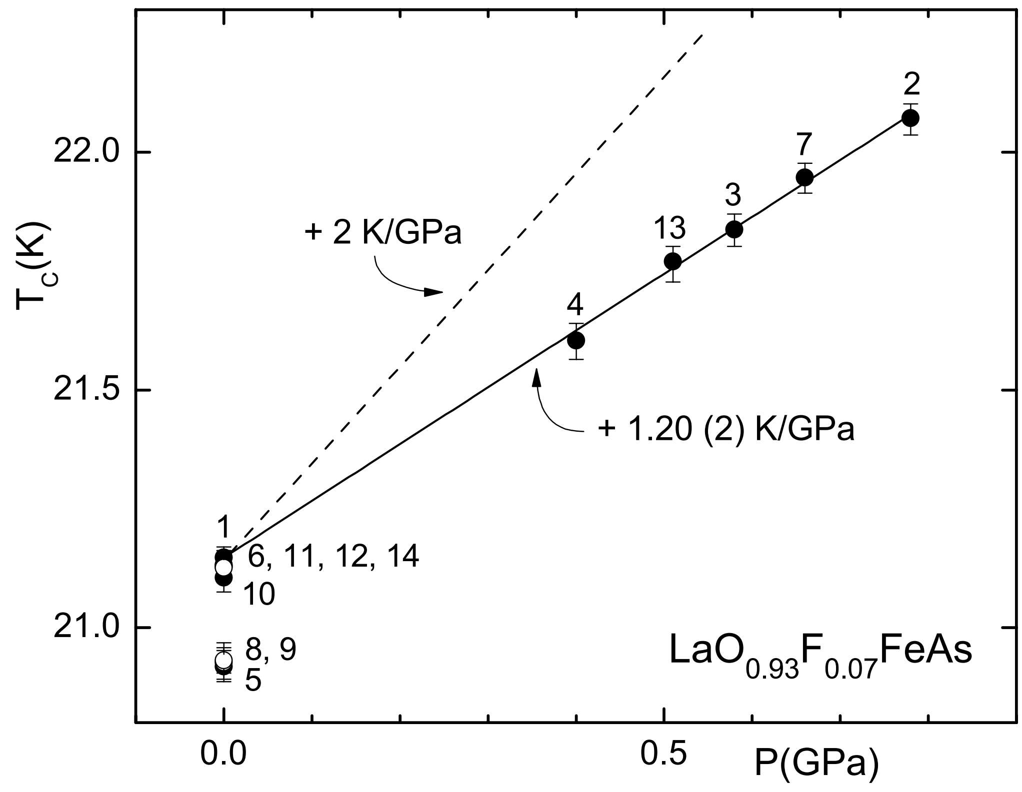

Figure 4.29: T_c versus pressure of LaO$_{0.93}$F$_{0.07}$FeAs sample for all data taken. Numbers give order of measurement (see text for details). Data for primed and unprimed numbers (open and closed circles) taken on different samples with masses 5.65 and 8.69 mg, respectively. Solid straight line is a guide to the eye and dashed line gives slope from resistivity onset data in [176].

To examine whether, as in the cuprates, there exists a particular (sub-RT) temperature above which such $T_c$relaxation occurs, we applied 0.66 GPa pressure at RT (point 7) and then released pressure at 60 K (point 8), reproducing exactly the previous results. Holding the sample at 100 K for 90 min resulted in no change in T_c(point 9). However, after holding the sample at 200 K for 100 min, T_c returned to its initial value (point 10). Warming back to RT for 1 h (point 11) and then for one week (point 12) resulted in no further change in T_c. A pressure of 0.51 GPa was then applied at 60 K (point 13) and released at 50 K (point 14); these T_c values faithfully track the +1.2 K/GPa straight line in Figure 4.29.

4.3.2.2 $\mathbf{LaO_{0.86}F_{0.14}FeAs}$ sample

For the $x = 0.14$ sample at ambient pressure, the 80-20 transition width in ac susceptibility is $\sim$ 2K, where $T_c \simeq$ 13.7 K from the transition onset and $T_c \simeq$ 12.5 K from the midpoint (see Figure 4.30). This onset value is several degrees less than from the resistivity onset ($\sim$19 K); however, the temperature of susceptibility midpoint is comparable to the resistivity zero point ($\sim$12 K) [176].

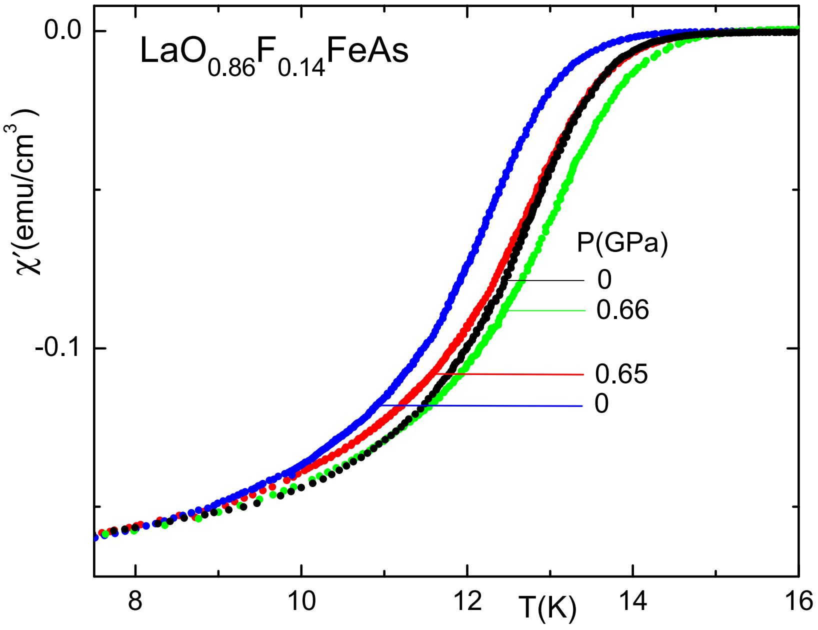

Figure 4.30: Real part of the ac susceptibility versus temperature at four selected He-gas pressures for $LaO_{0.86}F_{0.14}FeAs$ sample with mass 8.69 mg. Order of measurement given by pressure values from top to bottom (corresponds to points 1, 2, 5 and 6 in figure 4.31).

Previous high-pressure resistivity measurements on $\mathrm{LaO_{0.86}F_{0.14}FeAs}$, where pressure was always changed at RT, revealed that T_c from the resistivity onset increases rapidly with pressure in Fluorinert pressure medium at the rate +12 K/GPa. At a pressure of 0.66 GPa, therefore, T_c would be expected to increase by approximately 8 K. In Figure 4.31, however, the application of 0.66 GPa He-gas pressure at RT is seen to slightly broaden the transition in ac susceptibility and shift it only slightly (~0.2 K) to higher temperatures (point 2 in Figure 4.31), a shift 40 × less than the 8 K expected! This difference in $\mathrm{d}T_c/\mathrm{d}P$ decreases to 15× if the resistivity zero point is used (4.4 K/GPa).

The sample was then allowed to remain at RT for various cumulative lengths of time (20 h for point 3, 68 h for point 4 and 112 h for point 5) for a total of 112 h, during which time the pressure at RT decreased only slightly to 0.65 GPa; surprisingly, T_c is seen in Figure 4.31 to decrease by ~0.3 K (point 5)! Releasing the pressure then at 55 K to 0 GPa results in T_c shifting further downwards to a temperature (point 6) ~0.5 K less than its initial value at ambient pressure (point 1), the transition recovering its original sharpness. After the release of pressure at 55 K (point 6), holding the sample at 270 K for 1 h did not result in a further change in T_c (point 7). The superconducting transition appears to be stuck at this lower value. Such a feature was not observed in oxygen ordering phenomena in the cuprates [177].

A second sample from the same synthesis batch was then studied to check these highly anomalous results, yielding the data points (open circles) labeled with primed numbers in Figure 4.31. The value of T_c at ambient pressure was identical to that of the previous sample. Applying 0.78 GPa He-gas pressure at RT shifted T_c upward by only 0.23 K (point 2'), yielding a slope $\mathrm{d}T_c/\mathrm{d}P \simeq +0.30(1)$ K/GPa in excellent agreement with the results for the first sample (closed circles), but far less ($40\times$) than that (dashed line) observed in resistivity studies by Takahashi *et al.* [176] using Fluorinert pressure medium. The pressure was then reduced successively at low temperatures to $P = 0$ (2'$\rightarrow 3'$ at 60 K, 3'$\rightarrow 4'$ at 55 K, $4' \rightarrow 5'$ at 40 K and $5' \rightarrow 6'$ at 35 K). At ambient pressure, T_c now lies 0.62 K lower than the initial value (point 1'). Holding the sample for 1 h at 100 K caused no further change in T_c (point 7'). T_c was observed to shift upwards by 0. 33 K after holding at 200 K for 1.3 h (point 8'), but no further shift in T_c occurred after holding at 250 K for 1 h (point 9') or at RT for 30 h (point 10'). A pressure of 0. 33 GPa was then applied at 60 K (point 11') and released again at 50 K (point 12'), yielding a value of T_c approximately 0.8 K lower than the initial value (point 1'). The ambient pressure value of T_c did not change further, even after holding at RT for 170 h (point 13')!

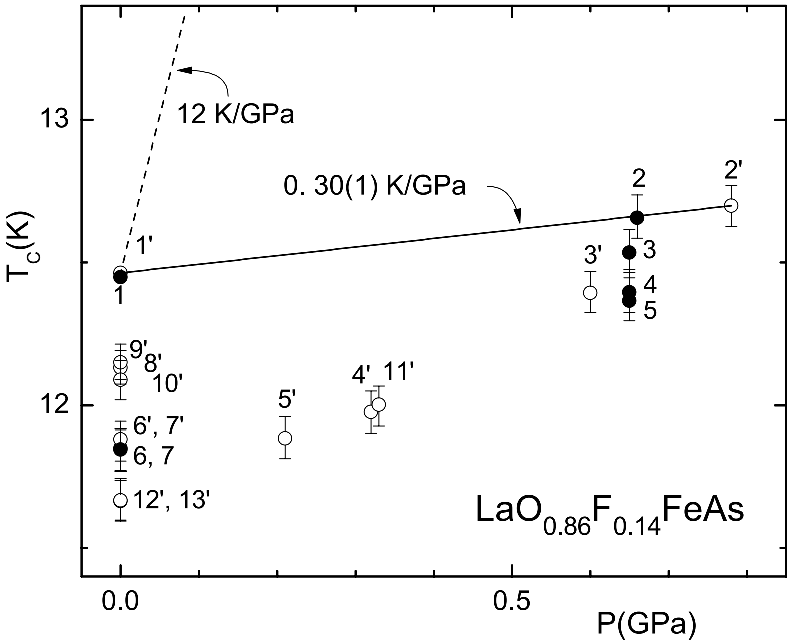

Figure 4.31: T_c versus pressure of $LaO_{0.86}F_{0.14}FeAs$ sample for all data taken. Numbers give order of measurement (see text for details). Data for primed and unprimed numbers (open and closed circles) taken on different samples with masses 5.65 and 8.69 mg, respectively. Solid straight line is to guide the eye and dashed line gives slope from resistivity onset data in [176].

4.3.3 Discussion

In all previous high-pressure studies on superconducting pnictides, pressure was changed at RT. We first compare the results of those studies with the present He-gas results for pressure change at RT. To our knowledge, the only measurements of $T_c(P)$ under pressure on $LaO_{1-x}F_xFeAs$ for fluorine concentrations near those ($x = 0.07$, $x = 0.14$) used in the present study are the resistivity measurements to 1.5 GPa with Fluorinert pressure medium by Takahashi *et al.* [176] for $x = 0.05$, 0.08, 0.11 and 0.14. As discussed above, if the pressure is changed at RT, the values obtained for $\mathrm{d}T_c/\mathrm{d}P$ from resistivity studies depend sensitively on the criterion used to determine T_c; the resistivity onset or $\rho \rightarrow 0$ point gives $\mathrm{d}T_c/\mathrm{d}P \simeq 2$ or 0.54 K/GPa, respectively, in contrast to the present ac susceptibility studies using He-gas pressure where the intermediate value $\mathrm{d}T_c/\mathrm{d}P \simeq 12$ K/GPa (onset) or 4.4 K/GPa ($\rho \rightarrow 0$ point), the respective values being 40× or 15× higher than the 0.30 K/GPa found in the present He-gas experiments. The fact that the anomalous temperature/pressure effects are most dramatic for the $x = 0.14$ sample, which lies near the substitution limit of F for O, suggests that the application of pressure may cause an irreversible phase separation. This would explain why the value of T_c does not recover in our experiments after a pressure cycle, as seen in Figure 4.31.

We note that at the lower concentration $x = 0.11$, Takahashi *et al.* [176] report $\mathrm{d}T_c/\mathrm{d}P \simeq 8$ K/GPa. On the other hand, at the same F concentration the much lower value $\mathrm{d}T_c/\mathrm{d}P \simeq 1.2$ K/GPa is obtained in a dc susceptibility measurement by Lu *et al.* [178] to 1 GPa pressure using an unspecified fluid pressure medium and in resistivity (onset) studies by Zocco *et al.* [179] using n-pentane: iso-amyl alcohol pressure medium to 0.94 GPa. It appears, therefore, that in the 1111 Fe-pnictides the pressure dependence of T_c depends sensitively not only on the dopant concentration but also on which physical property is measured, how the value of T_c is determined and the type of pressure transmitting medium used. This would appear to support the view of Yu *et al.* that the shear-stress effects play an important role in determining $T_c(P)$ in the oxypnictides, large shear stress generating significant changes in T_c. The marked temperature/pressure history effects seen in Figure 4.29 and 4.31 may be indicative of important shear-stress effects between grains in polycrystalline samples, even when purely hydrostatic He-gas pressure is applied. Parallel measurements on high-quality single crystals would test this hypothesis. It is also possible that the short-range diffusion of oxygen or fluorine anions within the crystal structure may occur in response to a change in pressure at RT, much as the oxygen ordering effects observed in the cuprate oxides [177].

In order to check whether the temperature/pressure history effect seen here might result from the penetration of the He pressure medium into the crystal lattice, we heated a 3.3 mg portion of the $x = 0.14$ sample used in the present He-gas experiments to 100°C while connected to a sensitive mass spectrometer. We were unable to detect the slightest trace of He escaping from the sample. Subsequent vaporization of this sample in an ultra-sensitive mass spectrometer set the He impurity level at $\sim$1ppm, an amount far too small to effect the dramatic changes observed in T_c.

An alternative scenario is conceivable. The undoped compound LaOFeAs exhibits a spin-density-wave (SDW) and structural phase transition (tetragonal→orthorhombic) below 150 K [51,188]. Substituting O with F or applying pressure is believed to suppress this transition and allow a superconducting ground state to appear. Competition between an SDW instability and superconductivity is also observed in $CeO_{1-x}F_xFeAs$ [53]. Perhaps shear-stress effects result in superconducting and non-superconducting SDW regions in the sample, which lead to the complex temperature/pressure history effects found in the present studies.

Whatever the explanation for the anomalous behavior of $T_c(P)$, it is likely that in the oxypnictides, as in the cuprates, a full understanding of the manner in which T_c changes under pressure may be difficult to obtain since it almost certainly depends on several factors simultaneously, including the strength of shear-stress effects as well as changes in the carrier concentration and the separation and area of the superconducting planes. Further experimentation that focuses on pressure-induced changes in superconductivity and crystal structure on global and local scales is clearly needed here.

4.4 Doped (P- and Co-) and Undoped $EuFe_2As_2$

$EuFe_2As_2$ exhibits spin-density-wave order below $T_s \approx 185$ K involving the Fe sublattice; under pressure T_s shifts rapidly to lower temperatures, disappearing completely above ~2.5 GPa [72]. The interactions between the strong local magnetic moments on each Eu site (Eu is divalent with a $4f^7$ orbital configuration) lead to type A antiferromagnetic order below 19 K, although the positive Curie-Weiss temperature points to predominantly ferromagnetic interactions [73]. Under pressure the magnetic ordering temperature reportedly remains constant to 2.6 GPa [74], increasing slowly at higher pressures before reaching a maximum near 55 K at ~9 GPa [72]. Only in a narrow region of pressure around 3 GPa has bulk superconductivity near 30 K been reported for $EuFe_2As_2$ [77]. The partial substitution of Co for Fe or of P for As in $EuFe_2As_2$ leads to a ferromagnetic ground state [77, 79, 81]; surprisingly, samples of polycrystalline $EuFe_2As_{1.4}P_{0.6}$ [79] and single-crystalline $EuFe_{1.78}Co_{0.22}As_2$ [81] have been reported to exhibit at ambient pressure ferromagnetism in coexistence with a superconducting transition near 26 K and 21 K, respectively, although only a very small fraction of full diamagnetic shielding was observed. In very recent work on well characterized single crystals of $EuFe_2As_{2\text{-}y}P_y$, Jeevan *et al.* [77] report that bulk superconductivity only exists in the narrow doping range $0.32 \leq y \leq 0.44$, and thus not for $y = 0.6$.

To study the intrinsic dependence of the magnetic properties and superconducting state on pressure for a given Fe-based material, it is essential to study only high quality single crystals under pure hydrostatic pressure. He-gas experiments have been carried out to measure the temperature-dependent ac susceptibility of single crystalline samples

$EuFe_2As_2$, $EuFe_2As_{1.4}P_{0.6}$, and $EuFe_{1.715}Co_{0.285}As_2$. Ac susceptibility experiments in a DAC system have also been tried in attempt to trace the magnetic ordering temperature to higher pressures in parent compound $EuFe_2As_2$.

4.4.1 He-Gas Experiment

A good portion of this section is taken from the paper by Banks, *et al.* [189]. In this project, H. B. Banks and L. Sun performed about 50% of the measurements and I performed 50% of the measurements.

High quality single crystals with nominal composition $EuFe_2As_2$, $EuFe_2As_{1.4}P_{0.6}$ and $EuFe_{1.715}Co_{0.285}As_2$measured in the He-gas system were brought here by Dr. L. Sun's group from Physics Institute, Chinese Academy of Sciences.. The x-ray diffraction done on $EuFe_2As_2$, $EuFe_2As_{1.4}P_{0.6}$ single crystals by Dr. L. Sun's group reveals the lattice parameters c = 1.207(7) and 1.188(7) nm, respectively. Comparison of these value of c with those obtained in the extensive studies by Jeevan *et al.* [77] on $EuFe_2As_{2\text{-}y}P_y$ crystals, where the doping level y for each crystal was determined by EDX, reveals that the actual level of P-doping for our crystal may be somewhat lower than the nominal value $y = 0.6$, but likely in the range $0.45 \leq y \leq 0.6$. As expected for this doping level, no sign of a SDW transition was observed in $EuFe_2As_{1.4}P_{0.6}$ either in the ac susceptibility or electrical resistivity over the temperature range 4-300 K [191].

The three samples were measured in He-gas system under pressures as high as 0.8 GPa. Measurements were carried out by slowly warming up through the transition at the rate ~100 mK/min and all susceptibility measurements were repeated at least once to verify that the reproducibility of the ferromagnetic or antiferromagnetic transition temperature $T_{C,\,N}$ was within 20 mK. The temperature-dependent background signal from the empty coil system was measured and subtracted from the sample data. Unfortunately, due to the pressure- and temperature-dependent background signal, it was not possible to reliably extract the pressure dependence of the Curie constant or Curie-Weiss temperature from the paramagnetic ac susceptibility in the temperature region well above $T_{C,\,N}$.

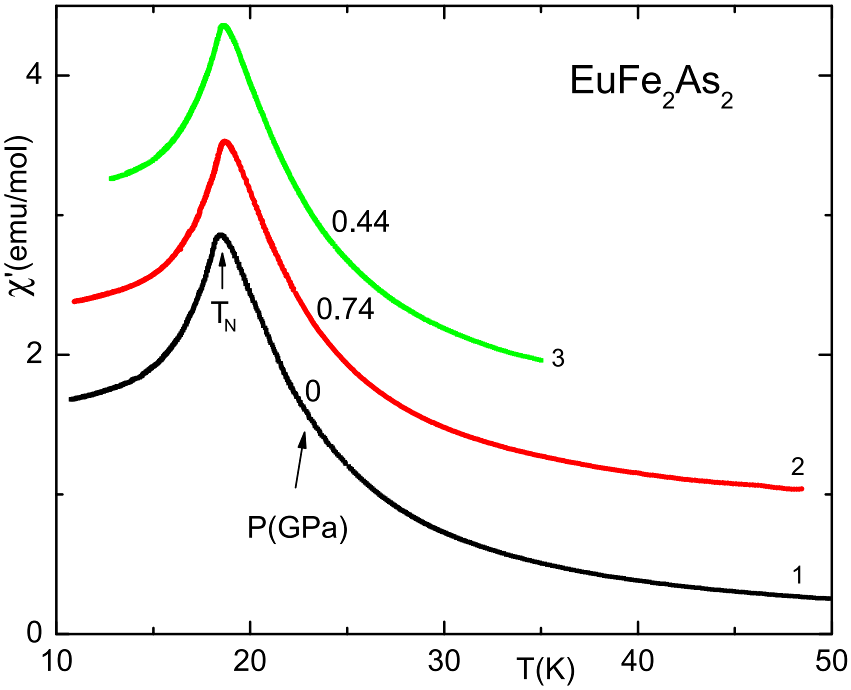

Figure 4.32: Real part of the ac susceptibility versus temperature at different pressures for $EuFe_2As_2$. Ordinate scale applies to data at ambient pressure (0 GPa). Data at high pressures are shifted vertically for clarity. Short vertical arrows give location of Néel (T_N) or Curie (T_C) temperatures. Numbers give order of measurement.

In Figure 4.32 the temperature-dependent magnetic susceptibility of $\mathrm{EuFe_2As_2}$ is plotted on an expanded scale for three different hydrostatic pressures. The Néel temperature T_N increases with pressure at the rate +0.35(3) K/GPa (see Figure 4.35). The temperature-dependent ac susceptibilities of $\mathrm{EuFe_2As_{1.4}P_{0.6}}$ and $\mathrm{EuFe_{1.715}Co_{0.285}As_2}$ are shown in Figure 4.33 and Figure 4.34; the anomaly near 15 K for both is not understood, but likely signals a minor spin rearrangement. In both cases the Curie temperature increases at the relatively rapid rates +2.4(1) and +2.0(1) K/GPa, respectively (see Figure 4.35). It has been suggested [190] that the increase in the Curie temperature with P-doping in $\mathrm{EuFe_2As_{2\text{-}y}P_y}$ for $\mathrm{y} \geq 0.44$ arises from the rapid reduction in the c lattice parameter, and thus the separation of the Eu-layers, with increasing y. As the Eu-planes come closer together, the interplanar exchange coupling increases which leads to the observed enhancement of the Curie temperature T_C . This scenario is in qualitative agreement with the present results where the application of pressure to 8 GPa is known to rapidly decrease c in $\mathrm{EuFe_2As_{1.4}P_{0.6}}$, with little or no change in a [191]. Whereas a 1% decrease in c through P-doping in $\mathrm{EuFe_2As_{2\text{-}y}P_y}$ leads to an increase in T_c by ∼18% [190], the present experiments together with Reference [191] show that a 1% decrease in c by applying pressure enhances T_C by ∼9%. The increase in T_C with P-doping thus appears to not be solely a chemical pressure effect.

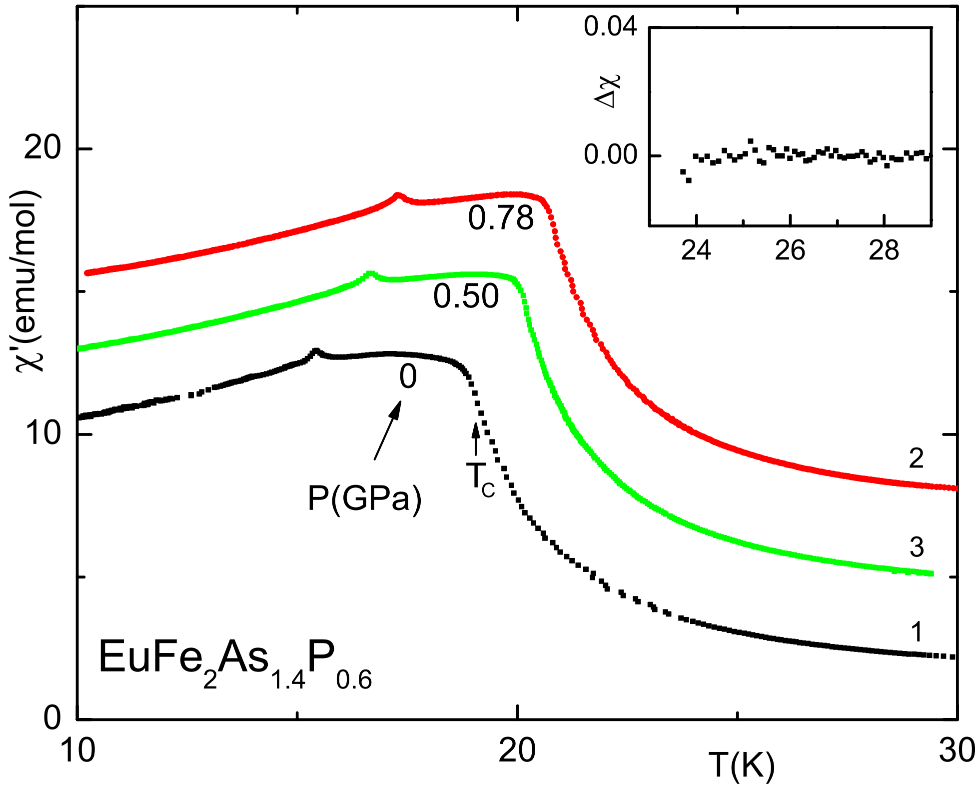

Figure 4.33: Real part of the ac susceptibility versus temperature at different pressures for $EuFe_2As_{1.4}P_{0.6}$ (inset gives "nonmagnetic" susceptibility versus temperature near 26 K in the same units as main figure. A magnetic (Curie-Weiss) fit has been subtracted from the data.). Ordinate scale applies to data at ambient pressure (0 GPa). Data at high pressures are shifted vertically for clarity. Short vertical arrows give location of Néel (T_N) or Curie (T_c) temperatures. Numbers give order of measurement.

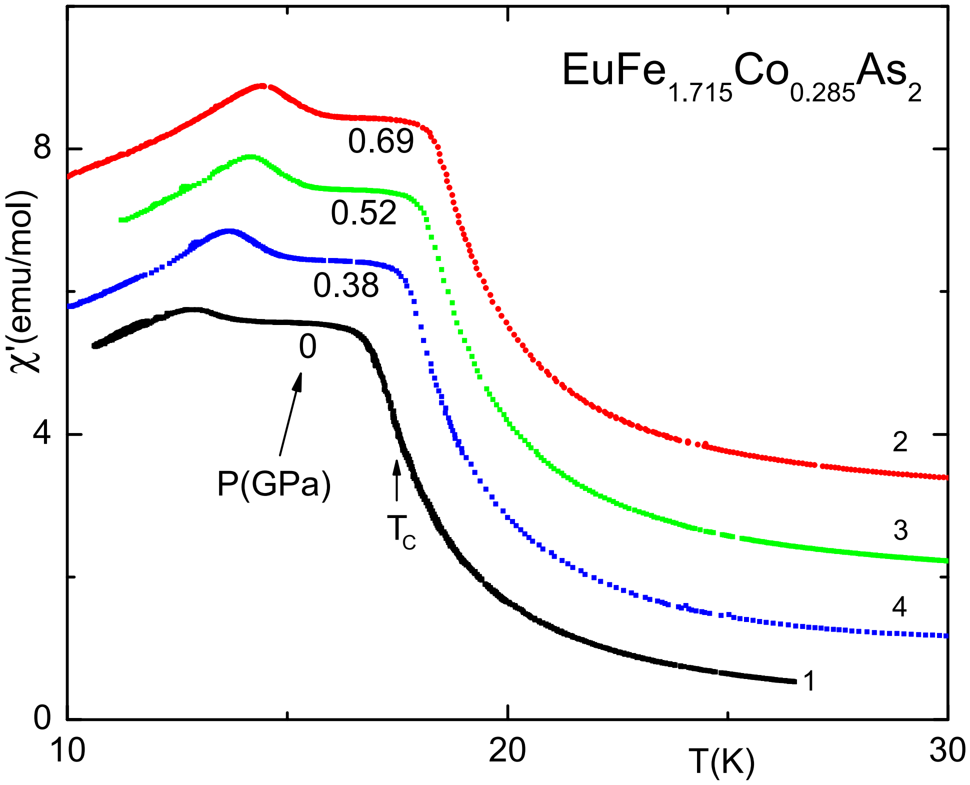

Figure 4.34: Real part of the ac susceptibility versus temperature at different pressures for $EuFe_{1.715}Co_{0.285}As_2$. Ordinate scale applies to data at ambient pressure (0 GPa). Data at high pressures are shifted vertically for clarity. Short vertical arrows give location of Néel (T_N) or Curie (T_C) temperatures. Numbers give order of measurement.

We speculate that the relatively small pressure derivative $\mathrm{d}\,T_C/\mathrm{d}P = +0.35$ K/GPa found for $EuFe_2As_2$ may be the result of mixed ferro- and antiferromagnetic exchange interactions within and between the Eu layers and/or arise from exchange coupling between the SDW-ordered Fe-sublattice and the antiferromagnetically ordered Eu layers. More complete details of the pressure-dependent spin structures of these systems would be needed before one could attempt a more quantitative interpretation of the present data. In contrast to a previous report of a superconducting transition near

26 K for $EuFe_2As_{1.4}P_{0.6}$ at ambient pressure [79], we observe no diamagnetic transition near 26 K (see inset in Figure 4.33) within our instrumental resolution of better than 0.01 emu/mole which corresponds to ~0.2% of full diamagnetic shielding. In $EuFe_{1.715}Co_{0.285}As_2$ we also find no evidence for the superconducting transition near 21 K reported by Jiang *et al.* [81] for this same compound at the somewhat different doping level $EuFe_{1.715}Co_{0.285}As_2$. In fact, to an accuracy of 0.2% of full diamagnetic shielding, we do not observe any indication of a superconducting transition for any of the three samples over the temperature and pressure ranges 10-60 K and 0-0.8 GPa, respectively. As pointed out earlier, this absence of superconductivity in $EuFe_2As_{1.4}P_{0.6}$ is consistent with the findings of Jeevan *et al.* [77]. In Figure 4.35 the magnetic ordering temperature is plotted versus hydrostatic pressure for the three crystals studied. One further (final) data point is shown for each crystal after the pressure was fully released to ambient. To check for possible temperature/pressure history effects such as we had observed for the superconducting transition temperature in polycrystalline $LaO_{1\text{-}x}F_xFeAs$ [195], a further experiment was carried out here for both doped $EuFe_2As_2$ crystals. For the Co-doped crystal, 0.3 GPa pressure was applied at room temperature but released at ~30 K, while for the P-doped crystal 0.85 GPa was applied at room temperature and released at ~78 K. For $EuFe_2As_2$ the pressure release (pts. 3→4 in Figure 4.35) was carried out at 150 K instead of room temperature. For all three samples the measured values of $T_{C,\ N}$ at ambient pressure were identical, within experimental accuracy, to the initial value at the beginning of the experiment. The absence of temperature/pressure history effects here is indicated by the fact that after the pressure release at low temperature the value of the magnetic ordering temperature reverts to its initial value

at the beginning of the experiment. In summary, in ac susceptibility measurements the magnetic ordering temperatures of three undoped and P- and Co-doped $EuFe_2As_2$ compounds are found to increase under hydrostatic (He-gas) pressure to 0.8 GPa, likely due to the rapid decrease in interplanar separation which promotes an enhanced ferromagnetic exchange interaction between Eu layers. At either ambient or high pressure no evidence is found for superconductivity in any compound studied for temperatures above 10 K.

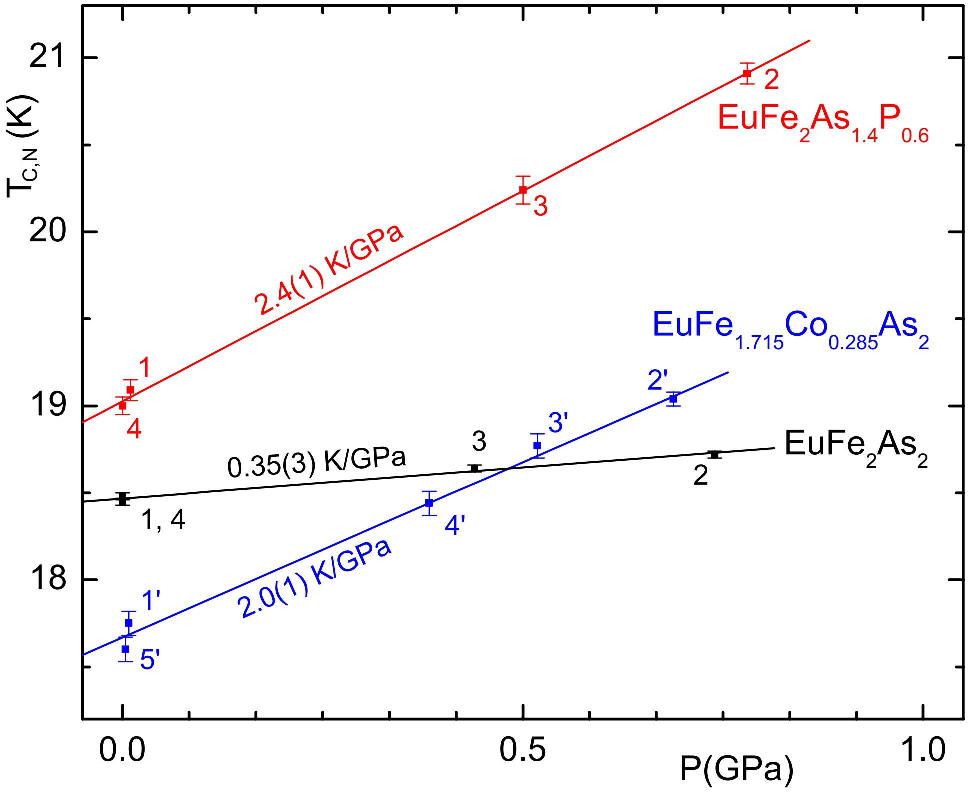

Figure 4.35: Pressure dependence of the magnetic ordering temperature $T_{C,\,N}$ for the three samples studied. Value of pressure derivative $\mathrm{d}T_{C,\,N}/\mathrm{d}P$ is given for each. Numbers give order of measurement; primed numbers are used to distinguish data from the Co-doped crystal.

4.4.2 DAC Experiment in $EuFe_2As_2$ Single Crystal Sample

$EuFe_2As_2$ orders antiferromagnetically at ambient pressure and becomes superconducting in a narrow region of pressure 2.5-2.7 GPa [72]. Above 8 GPa up to 12 GPa the antiferromagnetism of Eu^{2+} moments changes to ferromagnetism, which seems to coincide with the occurrence of valence change of Eu from the XMCD experiment at Eu's L_{III} edge up to 20 GPa by Matsubayashi, *et al.* [72]. To trace the ferromagnetic ordering above 12 GPa and search for possible superconductivity induced by the valence change, ac susceptibility experiments under hydrostatic pressures using He as pressure medium was carried out to 48.5 GPa down to 4 K in DAC system.

The single crystalline sample is provided by Dr. K. Matsubayashi, University of Tokyo, Japan. In the experiments, diamond anvils with 500 μm culet and Au-plated Re gaskets were used. A circular hole of a 250 μm diameter was EDM drilled at the center of the gasket. A big sample ($\sim$ 200 μm in diameter, $\sim$ 70 μm thick) was first loaded inside the gasket hole while a piece of MgB_2 was loaded in the compensation coil to check whether a antiferromagnetic signal could be detected with the coils. A kink representing the antiferromagnetic ordering could be clearly resolved around 19.4 K as seen in Figure 4.36. Then in next step, two runs of high pressure experiments with He as pressure medium were performed on a sample with a size of $\sim$ 100 μm in diameter and $30 - 40$ μm thick .

In the first run, measurements were done at ambient pressure, 1.9 GPa, 5 GPa, 7 GPa and 10.4 GPa. At 10.4 GPa during warming up to room temperature one diamond broke at about 220 K. During the second run, the temperature was kept below 180 K all the time. Measurements of susceptibility at pressures of 8 GPa, 10.4 GPa, 16.8 GPa, 22.2 GPa, 35.4 GPa, 42 GPa and 48.5 GPa were carried out. However, in both runs at all pressures, none of the antiferromagnetic, ferromagnetic and superconducting transition was observed in the temperature range of 4 K and 70 K. The absence of antiferromagnetic/ferromagnetic transition are possibly due to the small sample size in the hydrostatic measurements. It is important to point out that $EuFe_2As_2$ does not become superconducting to 48.5 GPa between 4 K and 70 K.

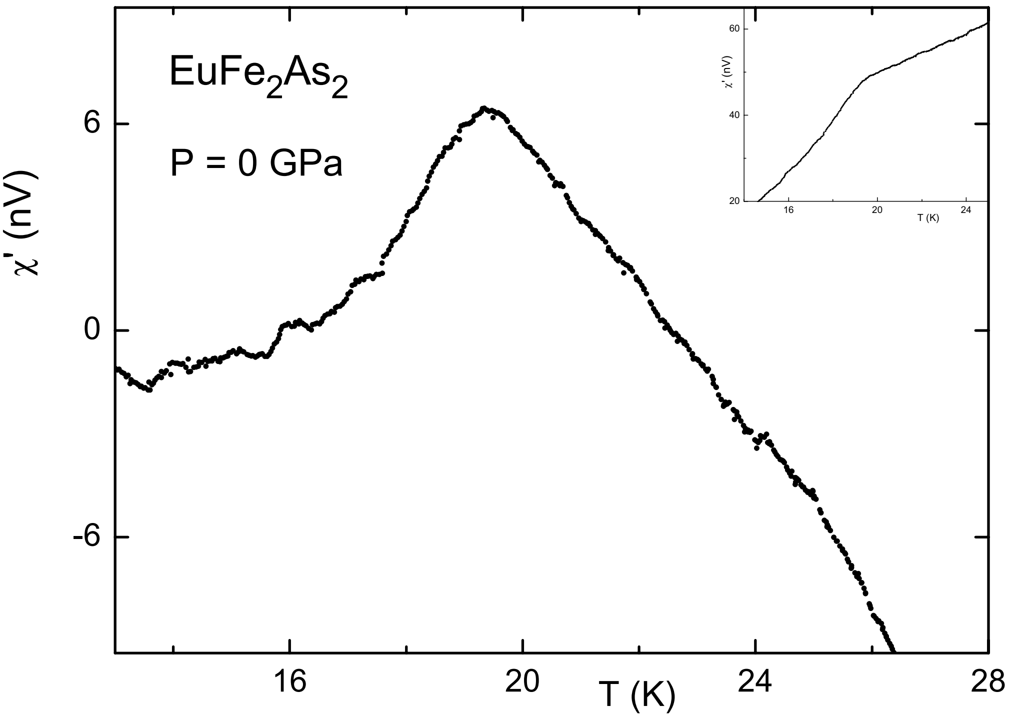

Figure 4.36: Real part of the ac susceptibility measurement showing the antiferromagnetic ordering around 19 K on a $EuFe_2As_2$ single crystal sample of ~ 200 μm diameter in the DAC coil. The data shown here is after background subtraction. The inset shows the raw data before subtraction.

4.5 Magnetism and Insulator-Metal Transition in EuO

At ambient pressure EuO is an insulator and orders ferromagnetically at 69 K with a saturation moment of close to 7 Bohr magneton [196]. Based on an s-f model, Eyert and Nolting report T_c reaching a maximum when EuO enters a mixed-valent state [42]. With increasing pressure, its Curie temperature changes drastically, increasing to about 200 K and decreasing monotonically at higher-pressure to 31 GPa. The pressure corresponding to the maximum T_c varies from 13 GPa [197] in the ac susceptibility experiments to 23 GPa from Mössbauer [198] and resistivity [199] experiments.

EuO has a NaCl-type structure (fcc) at ambient condition. A high-pressure structural study by Jayaraman [200] shows that with increasing pressure an isostructural transition occurs near 30 GPa with a 4% volume change before a transformation to a CsCl-type (bcc) structure near 40 GPa with a 6.5% volume change. The first structural transition near 30 GPa was suggested as a valence transition from Eu^{2+} to Eu^{3+}. In the second NaCl phase, the redish brown sample was observed to exhibit a silvery luster indicating an insulator-metal transition [200]. An optical reflection experiment by Zimmer *et al.* [201] suggests an insulator-metal transition in EuO at 14 GPa. However, two-point resistivity measurement up to 25 GPa by DiMarzio *et al.* [199] reports that an insulator-semiconductor occurs transition around 14 GPa and that the sample remains semiconducting up to 25 GPa.

From the above review of the previous studies it can be concluded that the question of Eu is in a divalent or trivalent state in EuO under pressure and whether it is a semiconductor or a metal is rather controversial. To extend the previous magnetic and electrical resistivity studies to higher pressures and search for possible superconductivity, ac susceptibility and electrical resistivity measurements have been performed up to 35.6 GPa and 36 GPa, respectively, in the diamond anvil cell with 500 micron culet and Re gasket.

In the ac susceptibility experiments, a few pieces of EuO single crystal sample with a total size less than 100 μm was loaded into the Re gasket hole (250 μm diameter) inside an Ar filled glovebox due to the air-sensitivity of the sample. The Re gasket was Au-plated to improve the sealing. The diamond anvil cell was then cool down to 1.5 K to load superfluid liquid He into the cell as a pressure medium. During all the high pressure measurements, the temperature was kept below 170 K to reduce the chance of He diffusing into and breaking the diamonds. The pressures were measured using ruby fluorescence. At ambient pressure and under pressure to 8.6 GPa, a kink corresponding to the ferromagnetic transition in the raw data was clearly observed. However, the kink broadened and became weaker under pressure. When further pressure was applied, no ferromagnetic transition could be resolved in the data measured between 4 K and 170 K up to 35.6 GPa, due to the limited sensitivity of the DAC coil system. No superconducting transition was observed in the measured pressure and temperature range. Unfortunately, one diamond failed after further pressure (45.6 GPa) was applied.

To search for a possible insulator-metal transition in EuO, two experimental runs of electrical resistivity were carried out to 36.2 GPa at room temperature. Both runs confirmed the a transition around 15 GPa reported previously by DiMarzio *et al.* [199]. However, whether this transition is an insulator-semiconductor or an insulator-metal transition cannot be concluded from the experiments due to the contact problems between two of the Pt electrodes and the gasket. Further experiments with strictly four-point measurement need to be carried out in the future to higher pressures.

Chapter 5

Summary

- Synchrotron x-ray diffraction experiments were carried out on Eu metal at ambient temperature to pressures as high as 92 GPa. Following the known bcc-to-hcp transition at 12 GPa, a mixed phase region is observed from 18 to 66 GPa until finally a single orthorhombic ($Pnma$) phase persists from 66 to 92 GPa. These results are compared to predictions from density functional theory calculations. Under pressure the relatively large molar volume V_{mol} of divalent Eu rapidly decreases, equaling or falling below $V_{\mathrm{mol}}(P)$ for neighboring trivalent lanthanides above 15 GPa. The present results suggest that above 15 GPa Eu is neither divalent nor fully trivalent to pressures as high as 92 GPa.

- XANES, XMCD and SMS experiments on Eu metal were performed to study the valence and magnetic state of Eu metal under pressure. Room temperature XANES measurements show no clear valence transition to 87 GPa, contrary to the previous report that the valence increases rapidly and reaches 2.6 at 24 GPa. The theoretical simulations suggest spectra changes originate from structural changes instead of from valence transition. In XMCD experiments, the XMCD amplitude first increases drastically under pressure to 20 GPa and then comes down at higher pressures to 60 GPa. The increase of magnetism to 20 GPa supports our conclusion from the XANES experiment that Eu remains divalent in this pressure range. Room temperature SMS experiments up to 73 GPa shows the isomer shift increases under pressure to around 20 GPa and then decreases at higher pressure. The isomer shift change under pressure suggests that Eu does not become trivalent up to 73 GPa.

- Ac susceptibility measurements have been carried out on $LaO_{1-x}F_xFeAs$ superconductors for $x = 0.07$ and 0.14 under He-gas pressures to $\sim$ 0.8 GPa. Not only do the measured values of $\mathrm{d}T_c/\mathrm{d}P$ differ substantially from those obtained in previous studies using other pressure media, but also the $T_c(P)$ depend on detailed pressure/temperature history of the sample. A sizable sensitivity of $T_c(P)$ to shear stresses provides a possible explanation.

- Ac susceptibility of single crystalline samples $EuFe_2As_2$, $EuFe_2As_{1.4}P_{0.6}$, and $EuFe_{1.715}Co_{0.285}As_2$ have been measured over the hydrostatic (He-gas) pressure regime up to 0.8 GPa. For all three samples the magnetic ordering temperature (17-19 K) from the Eu sublattice increases linearly with pressure. No evidence for a superconducting transition was observed in the susceptibility for any sample over the measured temperature/pressure range.

- Ac susceptibility and DC-electrical resistivity experiments to 36.5 GPa and 36.2 GPa were carried out in a EuO sample. No magnetic transition could be resolved above 8.6 GPa and no superconductivity was observed between 4 K and 170 K. A sudden drop of the electrical resistivity was observed near 15 GPa, but whether the sample becomes metallic or semiconducting above 15 GPa could not be determined due to contact problems under pressure.
- A photolithography procedure has been developed for fabrication of miniature coils and electrical resistivity leads on diamond anvils.

Appendix A

Search for Superconductivity in K and Na

Sodium

Among alkali metals, only Li and Cs have been found to be superconducting. Li superconducts at 4 mK at ambient pressure and T_c increases as high as 14 K under hydrostatic pressure. Recently a metal-semiconductor transition was observed in resistivity experiment near 80 GPa [22]. Na was experimentally observed to become transparent around 200 GPa [23]. To learn whether Na becomes superconducting before entering the transparent state, three sets of ac susceptibility experiments were carried out on Na up to 165 GPa.

Previous experiments in searching for superconductivity in Na by S. Deemyad were performed under hydrostatic conditions with He as a pressure medium at pressures of 6.2, 17.4, 23.4, 25.7, 33.0, 38.0, 45.0, 52.5, 56.5, and 58.0 GPa down to 4 K. No superconductivity was found.

During this thesis research, nonhydrostatic ac susceptibility measurements of Na down to 1.35 K at pressures of 64, 80, 106 and 117 GPa in beveled 180 μm anvils with Be:Cu gasket were carried out together with N. Hillier. Another run to higher pressure was performed with beveled 100 μm anvils at pressures of 62, 90, 105, 125, 146 and 161 GPa until one diamond broke after 180 GPa (extrapolated from membrane pressure) was applied.

Potassium

Potassium undergoes a phase transition from bcc to hcp at 12 GPa and transforms to K-III phase around 20 GPa. Potassium was predicted to superconduct $\sim$ 2 K in fcc phase, with T_c increasing to 11 K at 30 GPa [203].

In the previous efforts to search for superconductivity in K, S. Deemyad carried out hydrostatic ac susceptibility measurements up to 44 GPa and down to 4 K and M. Debessai performed nonhydrostatic measurements up to 94 GPa. No superconductivity was found in these experiments.

In attempt to search for pressure-induced superconductivity in K to a lower temperature and under hydrostatic conditions, ac susceptibility experiments were performed together with Dr. V. G. Tissen and N. Hillier. 500 μm anvils were used to achieve high pressure. Potassium sample with 99.98% (metal basis) purity from Alfa Aesar was loaded inside the Ar gas filled glovebox. Nonmagnetic and nonsuperconducting gasket material Ni(Mo 25%) brought by Dr. Tissen was used in the experiments. A few attempts were made to use He as pressure medium. However, the NiMo gasket hole closed up during warming after initial pressure was applied. Nonhydrostatic measurements at 0.4, 5.4, 10.9, 14, 17.5, and 23 GPa and down to 1.35 K showed no sign of superconductivity in K.

Very recently, K was predicted to be ferromagnetic above 20 GPa [204] and semiconducting around 25 GPa in K-III phase [205]. Further work is necessary to search for the possible semiconducting and/or ferromagnetic behaviors under moderate pressures through ac susceptibility, electrical resistivity and synchrotron experiments.

Appendix B

Superconductivity in Nb

A single crystalline sample Nb from Prof. John J. Neumeier in Montana State University was measured in He-gas pressure system as part of collaborative research. The superconducting temperature measured from the ac susceptibility shows $\mathrm{d}T_c/\mathrm{d}P$ = -32(6) mK/GPa (see in Figure B.1), which is slightly higher than the previous reported value of $\mathrm{d}T_c/\mathrm{d}P$ = -20(3) mK/GPa [206].

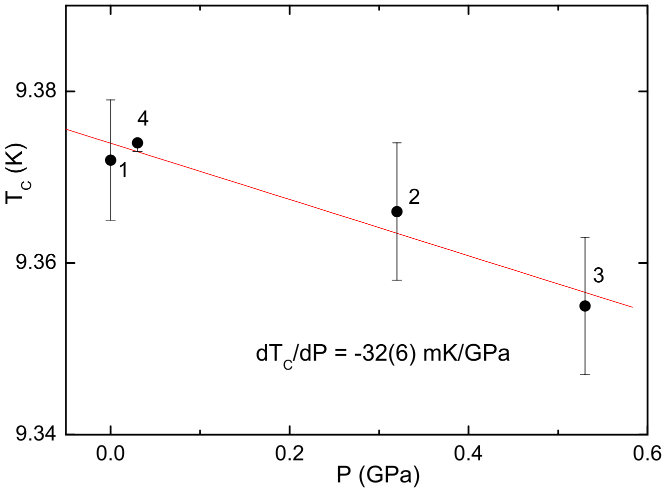

Figure B.1: Superconducting transition temperature of Nb under hydrostatic pressure to 0.53 GPa.

Bibliography

[1] H. K. Onnes, Akad. von Wetenschappen 14, 113 (1911).

[2] G. J. Sizoo and H. K. Onnes, Commun. Phys. Lab. Univ. Leiden, No. 180 b (1925).

[3] J. G. Bednorz and K. A. Müller, Z. Physik B 64, 189 (1986).

[4] C. W. Chu, P. H. Hor, R. L. Meng, L. Gao, Z. J. Huang, and Y. Q. Wang, Phys. Rev. Lett. 58, 405 (1987).

[5] L. Goa, Y. Y. Yue, F. Chen, Q. Xiong, R. L. Meng, D. Ramirez, C. W. Chu, J. H. Eggert, and H. K. Mao, Phys. Rev. B 50, 4260(R) (1994).

[6] C. W. Chu and B. Lorenz, Physica C 469, 385 (2009).

[7] M. Debessai, T. Matsuoka, J. J. Hamlin, J. S. Schilling, and K. Shimizu, Phys. Rev. Lett. 102, 197002 (2009).

[8] Y. Kamihara, H. Hiramatsu, M. Hirano, R. Kawamura, H. Yanagi, T. Kamiya and H. Hosono, J. Am. Chem. Soc. 128, 10012 (2008).

[9] K. Shimizu, T. Kimura, S. Furomoto, K. Takeda, K. Kontani, Y. Onuki, and K, Amaya, Nature 412, 316 (2001).

[10] J. Bardeen, L. N. Cooper, and J. R. Schrieffer, Phys. Rev. 108, 1175 (1957).

[11] J. S. Schilling, Handbook of High Temperature Superconductivity: Theory and Experiement, J. R. Schrieffer, Editor, J. S. Brooks, Associate Editor, chapter 11, Springer, Verlag, Hamburg, 2006.

[12] R. Grover, A. K. McMahan, and M. Ross, Europhys. Conf. Abstr. 1A, 18 (1975).

[13] J. S. Schilling and J. Hamlin, J. Phys.: Conf. Ser. 121, 052006 (2008).

[14] G. S. Anderson, S. Legvold, and F. H. Spedding, Phys. Rev. 109, 243 (1958).

[15] J. Wittig, Phys. Rev. Lett. 24, 812 (1970).

[16] J. Wittig, C. Probst and W. Wiedemann, Low Temperature Physics 13, 490 (1972).

[17] M. Debessai, T. Matsuoka, J. J. Hamlin, W. Bi, Y. Meng, K. Shimizu and J. S. Schilling, J. Phys.: Conf. Ser. 215, 012034 (2010).

[18] J. S. Schilling, Mat. Res. Soc. Symp. Proc. 22, 79 (1984).

[19] J. T. Waber and D. T. Cromer, J. Chem. Phys. 42, 4116 (1965).

[20] D. A. Yong, Phase Diagrams of the Elements, University of California Press, Berkeley, CA, 1991.

[21] O. Degtyareva, High Press. Res. 30, 343 (2010).

[22] T. Matsuoka and K. Shimizu, Nature 458, 186 (2009).

[23] Y. Ma, M. Eremets, A. R. Oganov, Y. Xie, I. Trojan, S. Medvedev, A. O. Lyakhov, M. Valle and V. Prakapenka, Nature 458, 182 (2009).

[24] C. Kittel, Introduction to Solid State Physics, 6th ed., 403, John Wiley and Sons Inc., New York, 1986.

[25] E. Yu. Tonkov, and E. G. Ponyatovsky, Phase Transformations of Elements under High Pressure, CRC Press, Boca Raton, FL, 2005.

[26] W. B. Holzapfel, J. Alloy Compd. 223, 170 (1995);

[27] A. Jayaraman, Phys. Rev. 135, A1056 (1964).

[28] M. I. McMahon and R. J. Nelmes, Chem. Soc. Rev. 35, 943 (2006).

[29] U. Schwartz, Z. Kristallogr. 219, 376 (2004).

[30] W. B. Holzapfel, Rep. Prog. Phys. 59, 29 (1996).

[31] J. C. Jamieson, Ann. Rev. Mater. Sci. 11, 233 (1981).

[32] E. Boldyreva and P. Dera (eds.), High-Pressure Crystallography: From Fundamental phenomena to Technological Applications, NATO Science for Peace and Security Series -B: Physics and Biophysics, Springer, 2009, 261-280.

[33] P. Vinet, J. R. Smith, Phys. Rev. B 35, 1945 (1987).

[34] F. D. Murnaghan, Am. J. Math. 49, 235 (1937).

[35] J-P. Poirier, A. Tarantola, Phys. Earth Planet Int. 109, 1 (1998).

[36] F. Birch, J. Geophys. Res. 83, 1257 (1978).

[37] W. B. Holzapfel, High Press. Res. 16, 81 (1998).

[38] K. Takemura and K. Syassen, J. Phys. F 15, 543 (1985).

[39] B. Johansson and A. Rosengren, Phys. Rev. B 11, 2836 (1975).

[40] A. Rosengren, and B. Johansson, Phys. Rev. B 13, 4 (1976).

[41] B. I. Min, H. J. F. Jansen, T. Oguchi and A. J. Freeman, J. Magn. Magn. Mater. 59, 277 (1986).

[42] V. Eyert and W. Nolting, Solid State Commn. 60, 905 (1986).

[43] D. B. McWhan, P. C. Souers, and G. Jura, Phys. Rev. 143, 385 (1966).

[44] D. Errandonea, R. Boehler, B. Schwager, and M. Mezouar, Phys. Rev. B 75, 014103 (2007).

[45] J. L. Smith and R. G. Haire, Science 200, 535 (1978).

[46] F. P. Bundy and K. J. Dunn, Phys. Rev. B 24, 4136 (1981).

[47] M. Debessai, J. J. Hamlin, and J. S. Schilling, Phys. Rev. B 78, 064519 (2008).

[48] J. Röhler, Physica (Amsterdam) 144B, 27 (1986).

[49] G. Wortmann, U. Ponkratz, B. Bielemeier and K. Rupprecht, High Press. Res. 28, 545 (2008).

[50] J. -C. Griveau, J. Rebizant, and G. H. Lander, Phys. Rev. Lett. 94, 097002 (2005).

[51] Kamihara Y., Watanabe T., Hirano M. and Hosono H., J. Am. Chem. Soc. 130, 3296 (2008).

[52] H. Takahashi, K. Igawa, K. Arii, Y. Kamihara, M. Hirano and H. Mosono, Nature 453, 376 (2008).

[53] F. G. Chen, D. Wu, W. Z. Hu, J. Dong, P. Zheng, J. L. Luo and N. L. Wang, Phys. Rev. B 100, 247002 (2008).

[54] Z. A. Ren, J. Yang, W. Lu, W. Yi, G. C. Chen, X. L. Dong, L. L. Sun, and X. Z. Zhao, Mater. Res. Innov. 12, 105 (2008).

[55] Z. A. Ren, J. Yang, W. Lu, W. Yi, X. L. Shen, Z. C. Li, G. C. Che, X. L. Dong, L. L. Sun, F. Zhou, and Z. X. Zhao, Europhys. Lett. 82, 57002 (2008).

[56] Z. A. Ren, W. Lu, J. Yang, W. Yi, X. L. Shen, Z. C. Li, G. C. Che, X. L. Dong, L. L. Sun, F. Zhou, and Z. X. Zhao, Chinese Phys. Lett. 25, 2215 (2008).

[57] K. Kadowaki, A. Goya, T. Mochiji, and S. V. Chong, J. Phy.: Conf. Ser. 150, 4 (2009).

[58] P. Chang, L. Fang, X. Zhu, G. Mu, H. Luo, Z. Wang, and H. Wen, Sci. China, G 51, 719 (2008).

[59] J. W. G. Bos, G. B. S. Penny, J. A. Rodgers, D. A. Sokolov, A. D. Huxley, and J. P. Attfield, Chem. Commun. 3634 (2008).

[60] G. Wang, L. J. Li, S. Chi, Z. Zhu, Z. Ren, Y. K. Li, Y. T. Wang, Y. T. Wang, X. Lin, Y. K. Luo, S. Jiang, X. F. Xu, G. H. Cao, and Z. A. Xu, Europhys. Lett. 83, 67006 (2008).

[61] M. D. Lumsden and A. D. Christianson, J. Phys.: Condens. Matter 22, 203203 (2010).

[62] K. Kuroki, arXiv:1008. 2286v1 [cond-mat.supr-con] (2010); K. Kuroki, H. Usui, S. Onari, R. Arita, and H. Aoki, Phys. Rev. B 79, 224511 (2009).

[63] Y. Mizuguchi, Y. Hara, K. Deguchi, S. Tsuda, T. Yamaguchi, K. Takeda, H. Kotegawa, H. Tou, and Y. Takano, Supercond. Sci. Technol. 23, 054013 (2010).

[64] C. de la Cruz, Q. Huang, J. W. Lynn, J. Li, W. Ratcliff II, J. L. Zarestky, H. A. Mook, G. F. Chen, J. L. Luo, N. L. Wang, and P. C. Dai, Nature 453, 899 (2008).

[65] T. Nomura, S. W. Kim, Y. Kamihara, M. Hirano, P. V. Sushko, K. Kato, M. Takata, A. L. Shluger, and H. Hosono, Supercond. Sci. Technol. 21, 125028 (2008).

[66] M Rotter, M. Tegel, D. Johrendt, I. Schellenberg, W. Hermes, and R. Pottgen, Phys. Rev. B 78, 020503 (2008).

[67] Q. Huang, Y. Qiu, W. Bao, M. A. Green, J. W. Lynn, Y. C. Gasparovic, T. Wu, G. Wu, and X. H. Chen, Phys. Rev. Lett. 101, 257003 (2008).

[68] J. -Q. Yan, A. Kreyssig, S. Nandi, N. Ni, S. L. Bud'ko, A. Kracher, R. J. McQueeney, R. W. McCallum, T. A. Lograsso, A. I. Goldman, and P. C. Canfield, Phys. Rev. B 78, 024516 (2008).

[69] A. Jesche, N. Caroca-Canales, H. Rosner, H. Borrmann, A. Ormeci, D. Kasinathan, H. H. Klauss, H. Luetkens, R. Khasanov, A. Amato, A. Hoser, K. Kaneko, C. Krellner, and C. Geibel, Phys. Rev. B 78, 180504 (2008).

[70] N. Ni, S. Nandi, A. Kreyssig, A. I. Goldman, E. D. Mun, S. L. Bud'ko, and P. C. Canfield, Phys. Rev. B 78, 014523 (2008).

[71] M. Tegel, M. Rotter, V. Weiss, F. Schappacher, R. Pottgen, and D. Johrendt, J. Phys.: Condens. Matter 20, 452201 (2008).

[72] K. Matsubayashi, K. Munakata, N. Katayama, M. Isobe, K. Ohgushi, Y. Ueda, N. Kawamura, M. Mizumaki, N. Ishimatsu, M. Hedo, I. Umehara, and Y. Uwatoko, arXiv:1007.2889, (2010).

[73] Z. Ren, Z. W. Zhu, S. Jiang, X. F. Xu, Q. Tao, C. Wang, C. M. Feng, G. H. Cao, and Z. A. Xu, Phys. Rev. B 78, 052501 (2008).

[74] C. F. Miclea, M. Nicklas, H. S. Jeevan, D. Kasinathan, Z. Hossain, H. Rosner, P. Gegenwart, C. Geibel, and F. Steglich, Phys. Rev. B 79, 2125009 (2009).

[75] J. Paglione and R. L. Greene, Nature Phys. 6, 645 (2010).

[76] Y. Mizuguchi, Y. Hara, K, Deguchi, S. Tsuda, T. Yamaguchi, K. Takeda, H. Kotegawa, H. Tou, and Y. Takano, Supercond. Sci. Technol. 23, 054012 (2010).

[77] H. S. Jeevan, D. Kasinathan, H. Rosner, and P. Gegenwart, in arXiv (cond-mat): 1011.4481.

[78] W. Uhoya, G. Tsoi, Y. K. Vohra, M. A. McGuire, A. S. Sefat, B. C. Sales, D. Mandrus, and S. T. Weir, J. Phys.: Condens. Matter 22, 292202 (2010).

[79] Z. Ren, Q. Tao, S. Jiang, C. Feng, C. Wang, J. Dai, G. Cao, and Z. Xu, Phys. Rev. Lett 102, 137002 (2009).

[80] A. Ahmed, M. Itou, S. Xu, Z. A. Xu, G. H. Cao, Y. Sakurai, J. Penner-Hahn, and A. Deb, Phys. Rev. Lett. 105, 207003 (2010).

[81] S. Jiang, H. Xing, G. Xuan, Z. Ren, C. Wang, Z. Xu, and G. Cao, Phys. Rev. B 80, 184514 (2009).

[82] X. B. Chen, Z. A. Z. A. Ren, D. H. Ding, and L. H. Liu, Sci. China 53, 1212 (2010).

[83] A. P. Hammersley, S. O. Svensson, M. Hanfland, A. N. Fitch, and D. Hausermann, High Press. Res. 12, 235 (1996).

[84] J. Howard and B. A. Hunter, A Computer Program for Rietveld Analysis of X-ray and Neutron Powder Diffraction Patterns, Lucas Height Research Laboratories, 1998.

[85] A. C. Larson and R. V. Von Dreele, GSAS Technical Manual (Los Alamos National Laboratory, Los Alamos, 1985-2000).

[86] International Tables for Crystallography, Springer.

[87] Brian H. Toby, Powder Diffraction Crystallography Resources, http://www.aps.anl.gov/ Xray_Science_Division/Powder_Diffraction_Crystallography/.

[88] B. D. Cullity, Elements of X-ray Diffraction, Chapter 1, 2nd edition, Addison-Welsley, 1978.

[89] J. Als-Nielsen and D. McMorrow, Elements of Modern X-ray Physics, Chapter 1, John Wiley & Sons, Ltd., 2001.

[90] F. Hippert, E. Geissler, J. L. Hodeau, E. Lelièver-Berna, Jean-René Regnard, Neutron and X-ray Spectroscopy, Springer, 2006.

[91] X-ray Database, X-ray Interactions with Matter, http://henke.lbl.gov/optical_constants/.

[92] A. Dadashev, M. P. Pasternak and G. Kh. Rozenberg, Rev. Sci. Instrum. 72, 2633 (2001).

[93] D. Haskel, Y. C. Tseng, N. M. Souza-Neto, J. C. Lang, S. Sinogeikin, Ya. Mudryk, K. A. Gschneidner, Jr and V. K. Pecharsky, High Press. Res. 28, 185 (2008).

[94] D. C. Koningsberger and R. Prins, X-ray Absorption-Principles, Applications, Techniques of EXAFS, SEXAFS and XANES, chap. 2, ed. John Willey (1988).

[95] M. A. Marcus, A. Manceau,Tutorial: Overabsorption, Thickness and Hole Effects in EXAFS, xafs.org.

[96] M. Newville, Lecture in Consortium for Advanced Radiation Sources, 2004.

[97] L. Gerward, Nucl. Instr. Meth. Phys. Res. 181, 11 (1981).

[98] M. E. Rose and M. M. Shapiro, Phys. Rev. 74, 1853 (1948).

[99] E. A. Stern and K. Kim, Phys. Rev. B 23, 3781 (1981).

[100] http://physics.nist.gov/PhysRefData/XrayMassCoef/tab3.html, NIST X-Ray Attenuation Databases.

[101] B. D. Cullity, Elements of X-ray Diffration, Apendix 8, 2nd edition, 1978.

[102] P. Kirkpatrick and A. V. Baez, J. Opt. Soc. Am. 38, 766 (1948).

[103] D. Haskel, Y. C. Tseng, and J. C. Lang, Rev. Sci. Instrum. 78, 083904 (2007).

[104] U. Fano, Phys. Rev. 178, 131 (1969).

[105] J. C. Lang and G. Srajer, Rev. Sci. Instrum. 66, 1540 (1995).

[106] T. Jo and S. Imada, J. Phys. Soc. Japan 62, 3721 (1993).

[107] J. C. Parlebas, K. Asakura, A. Fujiwara, I. Harada, A. Kotani, Physics Reports 431, 1-38 (2006).

[108] N. M Souza-Neto, D. Haskel, Y. C. Tseng, and G. Lapertot, Phys. Rev. Lett. 102, 057206 (2009).

[109] Y. H. Matsuda, Z. W. Ouyang, H. Nojiri, T. Inami, K. Ohwada, M. Suzuki, N. Kawamura, A. Mitsuda, and H. Wada, Phys. Rev. Lett. 103, 046402 (2009).

[110] B. J. Ruck, H. J. Trodahl, J. H. Richter, J. C. Cezar, F. Wilhelm, A. Rogalev, V. N. Antonov, B. Do Le, and C. Meyer, Phys. Rev. B 83, 174404 (2011).

[111] R. L. Mössbauer, Z. Phys. 151, 124 (1958).

[112] F. E. Fujita, Hyperfine Interat. 111, 191 (1998).

[113] T. C. Bibb, Principles of Mössbauer Spectroscopy, Chapman and Hall, London (1976), page 16-17.

[114] W. Sturhahn, J. Phys: Condens. Matter 16, S497 (2004).

[115] Y. L. Chen, D. P. Yang, Mössbauer Effect in Lattice Dynamics: Experimental Techniques and Applications, , Wiley (2007), Chapter 7.

[116] W. Sturhahn, E. E. Alp, T. S. Toellner, P. Hession, M. Hu and J. Sutter, Hyperfine Interact. 113, 47 (1998).

[117] W. Sturhahn and E. Gerdau, Phys. Rev. B 49, 9285 (1994).

[118] W. Sturhahn, Hyperfine Interact. 125, 149 (2000).

[119] E. E. Alp, W. Sturhahn and T. Toellner, Nucl. Intrum. Methods B, 97, 526 (1995).

[120] C. M. Lederer, J. M. Hollander, and I. Perlman, Table of Isotopes, 6th edition, New York:Wiley (1967).

[121] O. Leupold, J. Pollmann, E. Gerdau, H. D. Rüter, G. Falgel, M. Tegze, G. Bortel, R. Rüffer, A. I. Chumakov and A. Q. R. Baron, Europhys. Lett. 35, 671 (1996).

[122] O. Leupold, A. I. Chumakov, E. E. Alp, W. Sturhahn and A. Q. R. Baron, Hyperfine Interat. 123/124, 611 (1999).

[123] N. N. Greenwood and T. C. Gibb, Mössbauer Spectroscopy, Chapman and Hall, London (1971).

[124] N. N. Greenwood and T. C. Gibb, Mössbauer Spectroscopy, Chapman and Hall, London (1971), page 543-554.

[125] A. Q. R. Baron, Hyperfine Interact. 125, 29 (2000).

[126] N. C. Holmes, J.A. Moriaty, R. G. Gathers and W. J. Nellis, J. Appl. Phys. 66, 2962 (1989).

[127] J. N. Farrell and R. D. Taylor, Phys. Rev. Lett. 58, 2478 (1987).

[128] E. R. Bauminger, D. Froindlich, I. Nowik, S. Ofer, I. Felner, and I. Mayer, Phys. Rev. Lett. 30, 1053 (1973).

[129] S. Deemyad and J. S. Schilling, Phys. Rev. Lett. 91, 167001-1 (2003).

[130] W. A. Bassett, High Press. Res. 29, 163 (2009).

[131] J. S. Schilling, Magnetism at high pressure, Mat. Res. Soc. Symp. Proc. 22, 79 (1984).

[132] J. K. Hulum and B. B. Goodman, Phys. Rev. 106, 659 (1957).

[133] R. Boehler and H. De Hantsetters, High Press. Res. 24, 391 (2004).

[134] R. J. Hemley, H. K. Mao, G.Shen, J. Badro, P. Gillet, M. Hanfland and D. Husermann, Science 276, 1242 (1997).

[135] K. Brister, Rev. Sci. Instrum. 68, 1629 (1996).

[136] H. K. Mao, J. Shu, Y. Fei, J. Hu and R. J. Hemley, Phys. Earth Planet. Int. 96, 135 (1996).

[137] J. F. Lin, J. Shu, H. K. Mao and R. J. Hemley, Rev. Sci. Instrum. 74, 4732 (2003).

[138] N. Funamori and T. Sato, Rev. Sci. Instrum. 79, 053903 (2008).

[139] K. Syassen, High Press. Res. 28, 75 (2008).

[140] S. Buchsbaum, R. L. Mills and D. Schiferl, J. Phys. Chem. 88, 2522 (1984).

[141] G. J. Piermarini, S. Block, J. D. Barnett, and R. A. Forman, J. Appl. Phys. 46, 2774 (1975).

[142] H. K. Mao, P. M. Bell, J. W. Shaner, and D. J. Steinberg, J. Appl. Phys. 49, 3276 (1978).

[143] H. K. Mao, J. Xu, and P. M. Bell, J. Geophys. Res. 91, 4673 (1986).

[144] W. B. Holzapfel, High Press. Res. 25, 87 (2005).

[145] A. D. Chijioke, W. J. Nellis, A. Soldatov and R. A. Forman, J. Appl. Phys. 98, 114905 (2005).

[146] Y. Akahama and H. Kawamura, J. Appl. Phys. 100, 43516 (2006).

[147] M. Hanfland, K. Syassen, J. Appl. Phys. 57, 2752 (1984).

[148] M. I. Eremets, J. of Raman Spec. 34, 515 (2003).

[149] M. T. Debessai, Ph.D. Thesis, Washington University in St. Louis (2007).

[150] J. J. Hamlin, Ph.D. Thesis, Washington University in St. Louis (2007).

[151] D. X. Chen, J. A. Brug and R. B. Goldfarb, IEEE Transactions on Magnetics 27, 3601 (1991).

[152] D. D. Jackson, C.Aracne-Ruddle, V. Malba, and S. T. Weir, Rev. Sci. Instrum. 74, 2467 (2003).

[153] T. Tomita, Ph.D. Thesis, Washington University in St. Louis (2005).

[154] K. Syassen, G. Wortmann, J. Feldhaus, K. H. Frank, and G. Kaindl, Phys. Rev. B 26, 4745 (1982).

[155] A. Fuse, G. Nakamoto, M. Kurisu, N. Ishimatsu, H. Tanida, J. Alloys and Comp. 376, 34-37 (2003).

[156] G. N. Chestnut and Y. K. Vohra, Phys. Rev. Lett. 82, 1712 (1999).

[157] W. A. Grosshans and E. B. Holzapfel, Phys. Rev. B 45, 5171 (1992).

[158] Materials Preparation Center, Ames Laboratary, U.S. DOE, Ames, Iowa (http://www.mpc.ameslab.gov).

[159] A. Dewaele, P. Loubeyre, and M. Mezouar, Phys. Rev. B 70, 094112 (2004).

[160] A. R. Oganov and C.W. Glass, J. Chem. Phys. 124, 244704 (2006).

[161] G. Kresse and J. Furthmüller, Phys. Rev. B 54, 11169 (1996); G. Kresse and D. Joubert, Phys. Rev. B 59, 1758 (1999).

[162] N. G. Nereson, C. E. Olsen, and G. P. Arnold, Phys. Rev. 135, A176 (1964); R. L. Cohen, S. Hüfner, and K. W. West, Phys. Rev. A 184, 263 (1969).

[163] J. P. Perdew, K. Burke, and M. Ernzerhof, Phys. Rev. Lett. 77, 3865 (1996).

[164] R. G. Hennig, A. Wadehra, K. P. Driver, W. D. Parker, C. J. Umrigar, and J. W. Wilkins, Phys. Rev. B 82, 014101 (2010).

[165] W. Bi, Y. Meng, R. S. Kumar, A. L. Cornelius, W. W. Tipton, R. G. Hennig, Y. Zhang, C. Chen, and J. S. Schilling, Phys. Rev. B 83, 104106 (2011).

[166] L. W. Nixon and D. A. Papaconstantopoulos, Physica C 470, 709 (2010).

[167] S. Ono, T. Kikegawa, N. Hirao, and K. Mibe, Amer. Miner. 95, 880 (2010).

[168] A. Leineweber, H. Jacobs, W. Kockelmann, S. Hull, D. Hinz-Hübner, J. Alloys and Compd. 384, 1 (2004).

[169] G. N. Chestnut and Y. K. Vohra, Phys. Rev. B 61, R3768 (2000).

[170] Y. C. Zhao, F. Porsch and W. B. Holzapfel, Phys. Rev. B 50, 6603 (1994).

[171] N. C. Cunningham, W. Qiu, K. M. Hope, H.-P. Liermann, and Y. K. Vohra, Phys. Rev. B 76, 212101 (2007).

[172] D. Wohlleben, in Valence Fluctuations in Solids, L. M. Falicov, W. Hanke, and M. B. Maple, editors (New York, North-Holland, 1981) p. 1.

[173] I. Turek, J. Kudrnovský, M. Divis, P. Franek, G. Bilhlmayer, and S. Blügel, Phys. Rev. B 68, 224451 (2003).

[174] J. Kunes, R. Laskowski, Phys. Rev. B 70, 174415 (2004).

[175] N. Souza-Neto, private communication.

[176] H. Takahashi, H. Okada, K. Igawa, K. Arri, Y. Kamihara, S. Matsuishi, M. Hirano, H. Hosono, K. Matsubayashi and Y. Uwatoko, J. Phys. Soc. Japan 77, C78 (2008).

[177] J. S. Schilling, Handbook of High-Temperature Superconductivity: Theory and Experiment ed J. R. Schriffer, associated ed. J. S. Brooks (New York:Springer) Chaper 11, p 427, 2007.

[178] W. Lu, J. Yang, X. I. Dong, Z. A. Ren, G. C. Che, and Z. X. Zhao, New J. Phys. 10, 063026 (2008).

[179] D. A. Zocco, J. J. Hamlin, B. R. Beckett, R. E. Baumbach R. E., M. B. Maple, M. A. McGuire, A. S. Sefat, B. C. Sales, R. Jin, D. Mandrus, J. R. Jeffries, S. T. Weir and Y. K. Vohra, Physica C 486, 2229 (2008).

[180] S. Deemyad, T. Tomita, J. J. Hamlin, B. R. Beckett, J. S. Schilling, D. G. Hinks, J. D. Jorgensen, S. Lee and S. Tajima, Physica C 385, 105 (2003).

[181] M. S. Torikachvili, S. L. Bud'ko, N. Ni, P. C. Canfield and G. M. Luke, Phys. Rev. B 79, 020511 (2009).

[182] H. Fukazawa, N. Takeshita, T. Yamazaki, K, Kondo, K. Kirayama, Y. Kohori, K. Miyazawa, H. Kito, H. Eisaki and A. Iyo, J. Phys. Soc. Japan 77, 105004 (2008).

[183] W. Yu, A. A. Aczel, T. J. Williams, S. L. Bud'ko, N. Ni, P. C. Canfield and G. M. Luke, Phys. Rev. B 79, 010511 (2009).

[184] K. Matsubayashi, N. Katayama, K. Ohgushi, A. Yamada, K. Munakata, T. Matsumoto and Y. Uwatoko, J. Phys. Soc. Japan 78, 073706 (2009).

[185] S. R. Saha, N. P. Butch, K. Krishenbaum, J. Paglione and P. Y. Zavalij, Phys. Rev. Lett. 103, 037005 (2009).

[186] J. E. Schirber, D. L. Overmyer, K. D. Carlson, J. M. Williams, A. M. Kini, H. H. Wang, H. A. Charlier, B. J. Love, D. M. Watkins and G. A. Yaconi, Phys. Rev. B 44, 4666 (1991).

[187] C. W. Chu, T. F. Smith and W. E Gardner, Phys. Rev. B 1, 214 (1970).

[188] C. de la Cruz, Q. Huang, J. W. Lynn, J. Li, W. II. Ratcliff, J. L. Zarestky, H. A. Mook, G. F. Chen, J. L. Luo, N. L. Wang and P. Dai, Nature 453, 869 (2008).

[189] H. B. Banks, W. Bi, L. Sun, G. F. Chen, X. H. Chen, J. S. Schilling, to appear in Physica C (2011).

[190] T. Terashima, M. Kimata, H. Satsukawa, A. Harada, K. Hazama, S. Uji, H. S. Suzuki, T. Matsuomoto, and K. Murata, J. Phys. Soc. Japan 78, 083701 (2009).

[191] J. Guo, L. Sun, C. Zhang, G. Chen, J. He, X. Dong, W. Yi, Y. Li, X. Li, J. Liu, Z. Jiang, X. Wei, Y. Huang, Q. Wu, X. Dai, and Z. Zhao, preprint in arXiv (cond-mat): 1008.2086.

[192] J. J. Ying, T. Wu, Q. J. Zheng, Y. He, G. Wu, Q. J. Li, Y. J. Yan, and L. Xie, Phys. Rev. B 81, 052503 2010.

[193] S. Jiang, Y. Luo, Z. Ren, Z. Zhu, C. Wang, X. Xu, Q. Tao, G. Cao, and Z. Xu, New J. Phys. 11, 025007 (2009).

[194] Y. Xiao, Y. Su, M. Meven, R. Mittal, C. M. N. Kumar, T. Chatterji, S. Price, J. Persson, N. Kumar, S. K. Dhar, A. Thamizhavel, and Th. Brueckel, Phys. Rev. B 80, 174424 (2009); J. Herrero-Martin, V. Scagnoli, C. Mazzoli, Y. Su, R.Mittal, Y. Xiao, T. Brueckel, N. Kumar, S. K. dhar, A. Thamizhavel, and L. Paolasini, Phys. Rev. B 80, 134411 (2009).

[195] W. Bi, H. B. Banks, J. S. Schilling, H. Takahashi, H. Okada, Y. Kamihara, M. Hirano, and H. Hosono, New J. Phys. 12, 023005 (2010).

[196] D. B. McWhan, P. C. Souers and G. Jura, Phys. Rev. 143, 385 (1966). B. T. Matthias, R. M. Bozorth, and J. H. Van Vleck, Phys. Rev. Lett. 7, 160 (1961).

[197] V. G. Tissen and E. G. Ponyatovskii, JETP Lett. 46, 361 (1988).

[198] M. M. Abd-Elmeguid and R. D. Taylor, Phys. Rev. B 42, 1048 (1990).

[199] D. DiMarzio, M. Croft, N. Sakai and M. W. Shafer, Phys. Rev. B 35, 8891 (1987).

[200] A. Jayaraman, Phys. Rev. Lett. 29, 1674 (1972).

[201] H. G. Zimmer, K. Takemura, and K. Syassen, Phys. Rev. B 29, 2350 (1984).

[202] S. Deemyad, Ph.D. Thesis, 2004.

[203] A. Sanna, C. Franchini, A. Floris, G. Profeta, N. N. Lathiotakis, M. Lüders, M. A. L. Marques, E. K. U. Gross, A. Continenza, and S. Massidda, Phys. Rev. B 73, 144512 (2006).

[204] C. J. Pickard, R. J. Needs, arXiv:1103.6141v1 (2011).

[205] M. Marqués, G. J. Achland, L. F. Lundegaard, G. Stinton, R. J. Nelmes, and M. I. McMahon, Phys. Rev. Lett. 103, 115501 (2009).

[206] T. F. Smith, Phys. Lett. A 33, 465 (1970).